DAMAGE DETECTION OF LAMINATED COMPOSITE STRUCTURES USING INVERSE FINITE ELEMENT METHOD

by
FARAZ GANJDOUST

Submitted to the Faculty of Engineering and Natural Sciences
in partial fulfilment of
the requirements for the degree of Master of Science

Sabancı University
July 2022

DAMAGE DETECTION OF LAMINATED COMPOSITE STRUCTURES USING INVERSE FINITE ELEMENT METHOD

Approved by:

Date of Approval: 18.07.2022

ABSTRACT

DAMAGE DETECTION OF LAMINATED COMPOSITE STRUCTURES USING INVERSE FINITE ELEMENT METHOD

FARAZ GANJDOUST

MECHATRONICS ENGINEERING M.Sc. THESIS, JULY 2022

Thesis Supervisor: Assist. Prof. Adnan Kefal

Keywords: Damage detection, laminated composite shells, inverse finite element method, refined zigzag theory, structural health monitoring

In recent years, structural health monitoring (SHM) has been revolutionized with the advent of an inverse method based on the minimization of a weighted least squares functional, known as inverse finite element method (iFEM). This approach is suitable for detection of damage, thanks to its ability in accurate full-field reconstruction of the displacement field over the problem domain. This study focuses on the application of iFEM for shape sensing and damage detection in various case studies, using numerically generated in-situ strain data via high fidelity forward finite element modeling (FEM). The study is conducted utilizing quadrilateral inverse-plane, and quadrilateral inverse-shell elements (iQS4). By utilizing the field variable achieved via the iFEM, equivalent von Mises strains are computed, after that, through definition of a damage index, the health of the structure is evaluated in terms of the presence of damage as well as its extent. Additionally, a new strategy is introduced for detection of the through-the-thickness damage in laminated composite materials by incorporating refined zigzag theory (RZT) in the iFEM algorithm. As a result of these analyses, the inverse algorithm shows its efficiency in detecting flawed regions over the problem domain and through the thickness of layered materials, both in terms of the location of the damage as well as its morphology.

ÖZET

LAMİNE KOMPOZİT YAPILARDA TERS SONLU ELEMANLAR YÖNTEMİ İLE HASAR TESPİTİ

FARAZ GANJDOUST

MEKATRONİK MÜHENDİSLİĞİ YÜKSEK LİSANS TEZİ, TEMMUZ 2022

Tez Danışmanı: Dr. Öğr. Üyesi Adnan Kefal

Anahtar Kelimeler: Hasar tespiti, lamine kompozit kabuklar, ters sonlu elemanlar yöntemi, hassaslaştırılmış zikzak teorisi, yapısal sağlık izleme

Son yıllarda, ağırlıklı en küçük kareler fonksiyonelinin minimizasyonuna dayalı bir yöntem olan ters sonlu elemanlar metodu (iFEM), yapısal sağlık izleme alanında bir devrim yaratmıştır. Bu yaklaşım, problem alanı üzerindeki yer değiştirme alanının isabetli bir biçimde tam saha yeniden yapılandırmasına imkân tanımasından dolayı hasar tespiti için uygundur. Bu çalışma, iFEM'in direkt sonlu elemanlar yöntemi ile yüksek doğrulukla elde edilmiş yerleşik gerinim verilerini kullanarak şekil algılama ve hasar tespiti üzerine odaklanmaktadır. Burada dört kenarlı ters düzlem elemanları ve dört kenarlı ters kabuk elemanları (iQS4) kullanılmıştır. iFEM kullanılarak elde edilen alan değişkenleri ile eşdeğer von Mises gerinimleri hesaplanmış ve sonrasında hasar endeksi tanımlanarak yapıdaki hasarın varlığı ve boyutuna ilişkin değerlendirmeler yapılmıştır. Ek olarak, hassaslaştırılmış zikzak teorisini (RZT) iFEM algoritması içerisinde kullanarak lamine kompozitlerde kalınlık boyunca hasar tespiti için yeni bir strateji tanıtılmıştır. Bu analizler sonucunda ters analiz algoritması, problem alanında ve katmanlı malzemelerin kalınlıkları yönünde hasarlı bölgelerin tespitini, hasarın konum ve şekli açısından, isabetli bir şekilde yapabildiğini göstermektedir.

ACKNOWLEDGEMENTS

I would like to extend my gratitude to my thesis supervisor, Asst. Prof. Dr. Adnan Kefal, for his consistent support and guidance throughout my master's program. Also, the financial supports provided by the Scientific and Technological Research Council of Turkey (TUBITAK) under the grant numbers, 217M207 and 5200082, are greatly acknowledged. I also want to thank all the members of the Computational Mechanics & Engineering Optimization (CMEO) research group and Sabanci University Integrated Manufacturing Technologies Research and Application Center (SU-IMC) friends and staff for creating a professional and at the same time, friendly work environment. In addition, the moral support I received from those closest to me, Sina Khalilvandi Behrouzyar, Dr. Isa Emami Tabrizi, Dr. Marjan Hezarkhani, and Sina Shahri Majarshin cannot be underestimated. Also, if it wasn't for the immeasurable help and moral support of the one and only Sahar Dadashi Farkhandi, it would have been extremely difficult to go through these times. In the end, I want to thank my family for their unlimited support and love, and for providing the means for me to reach where I am now.

"Living, there is no happiness in that. Living: carrying one's painful self through the world.
But being, being is happiness. Being: becoming a fountain, a fountain on which the universe falls like warm rain."
Milan Kundera

To my father, my mother, and my brother Ramiz, for making me realize that I "am", and for making my being more meaningful.

TABLE OF CONTENTS

LIST OF TABLES

LIST OF FIGURES

LIST OF ABBREVIATIONS

AI Artificial Intelligence 2

FBG Fiber Bragg Grating 1, 3, 6, 22, 37, 40, 53

FEM Finite Element Method iv, xii, xiii, 31, 33, 34, 35, 38, 40, 41, 42, 43, 49, 50, 51, 54, 55, 59, 63

FSDT First-order Shear Deformation Theory 4

iFEM Inverse Finite Element Method . iv, v, xi, xii, xiii, 1, 2, 3, 4, 5, 6, 7, 10, 11, 16, 22, 24, 26, 27, 30, 32, 33, 34, 35, 36, 38, 40, 41, 42, 43, 44, 45, 46, 47, 48, 49, 50, 51, 52, 53, 54, 55, 56, 57, 59, 60, 62, 63, 64

MM Modal Method 1, 3

MTT Modal Transformation Theory 1

RZT Refined Zigzag Theory . . iv, v, xiii, 4, 5, 7, 19, 22, 26, 27, 52, 55, 56, 57, 59, 60, 62, 63, 64

SHM Structural Health Monitoring . . . . . iv, 1, 2, 3, 40, 64

1. INTRODUCTION

The dependency of modern affairs and economy on marine and aerospace vehicles has entailed their respective industries to devote extra attention to design of such structures. Hence, the manufacturers are always in a constant struggle to make a compromise between the cost-efficiency of the manufactured parts, and their safety. Furthermore, considering that any type of in-service accidents for such vehicles are prone to having catastrophic outcomes, finely detailed monitoring procedures must be devised with the purpose of studying the in-process state of various parts. This not only saves lives and economic interests of companies through prevention of vicious accidents, but also acts as a sign of warning for the operators to make necessary modifications in the machinery, or halt the operation of certain parts so as to prohibit the further progression of faults and defects in the mechanical system. SHM provides the industrial units with valuable information of this sort. Among various SHM methods, the iFEM shows great capabilities in terms of its robustness in full-field reconstruction and damage sensing results it provides, as well as the fact that it can also enable real-time monitoring of the structures by making use of strain sensors mounted on and/or embedded within the structure.

By putting the aforementioned advantages of SHM in perspective, various techniques have been proposed to conduct such operations. In their review study, Gherlone, Cerracchio & Mattone (2018) underscored the importance of accurate full-field reconstruction of the displacement field in conducting a successful SHM operation and classified the shape-sensing approaches. The first approach, originally targeting the beam problems, was proposed by Ko, Richards & Tran (2007), and is based on the reconstruction of the displacement field of the structure through the integration of the strain data measured via strain gauges or fiber bragg grating (FBG) sensors (Kang, Kim & Han, 2007; Kim, Kang & Han, 2011; Ko, Richards & Fleischer, 2009). In another technique, continuous functions are fit over discrete in-situ strain data, and through establishing the strain-displacement relations, the displacement field is recovered. This approach is the generic form of the modal method (MM), which is also known as modal transformation theory (MTT) (Bogert, Haugse & Gehrki,

2003; Pisoni, Santolini, Hauf & Dubowsky, 1995; Rapp, Kang, Han, Mueller & Baier, 2009). In this context, other shape-sensing methods were also developed within the framework of artificial intelligence (AI) (Bruno, Toomarian & Salama, 1994). However, iFEM possesses features that make it more general in comparison to the aforementioned approaches. Attributes such as the applicability of the method with no requirement for material models and/or loading conditions, the ability of full-field reconstruction of detailed and complex geometries, real-time delivery of the monitoring results, and cost-efficiency and precision, even with strain data acquired sparsely over the problem domain. These are the key properties of the iFEM which makes it more appealing than the other shape-sensing techniques, and at the same time distinguish iFEM and show its generality in contrast to other methods, such as shape-sensing via AI, in which the network is trained only for a certain class of problems. The inverse method, iFEM, was first introduced by Tessler & Spangler (2005), and ever since, major contributions have been made to further develop this approach numerically, and when coupled with experimental test data. Among theoretical efforts in the field, the studies of Tessler & Spangler (2004) through establishing a three-node triangular inverse-shell element, iMIN3, Kefal, Oterkus, Tessler & Spangler (2016) through developing a four-node quadrilateral inverse-shell element, iQS4, and Kefal (2019) by introducing an eight-node curved inverse-shell element stand out, as most of the numerical implementations of iFEM are made through the utilization of these inverse elements. In this context, Abdollahzadeh, Kefal & Yildiz (2020) presented a comparative study in which they evaluated the efficiency of different types of inverse elements, namely iMIN3, iQS4, and iCS8, in terms of their performance with regard to reconstructing the field variables. They concluded that iCS8 is superior to the other two inverse element types, specifically for models with more detailed and complex geometries. Furthermore, Kefal & Oterkus (2020) established the mathematical framework for the isogeometric iFEM. To this end, various numerical manipulations have been coupled with this inverse approach so as to enhance its performance in the reconstruction of the field variable, the displacement field. The primary, yet crucial problem which is covered in the work of Roy, Tessler, Surace & Gherlone (2020) is the determination of a suitable sensor deployment scheme to take the most advantage of the iFEM. Other works involve the definition of smoothing methods, such as in Kefal, Tabrizi, Yildiz & Tessler (2021), or pre-extrapolation of the strain data as exhibited in Oboe, Colombo, Sbarufatti & Giglio (2021a).

In conjunction with such theoretical advances, in recent years, numerous studies have incorporated iFEM for the purpose of SHM. Gherlone, Cerracchio, Mattone, Di Sciuva & Tessler (2014) developed iFEM models for the shape-sensing of beams,

by defining its kinematic relations based on the relations associated with the Timoshenko beam, and showed that for a single element, using the in-situ strain measurements, their model can reconstruct the shape of the beam. Then by increasing the number of the inverse elements, they conducted a convergence study. It was also shown that even with interference present, their model is capable of capturing deformations. Cerracchio, Gherlone & Tessler (2015) applied iFEM to problems involving static, dynamic, and thermal loads; through their numerical investigation, the versatility of the iFEM algorithm for various types of loading was illustrated. Kefal & Oterkus (2015) assessed the applicability of the four-node quadrilateral inverse-shell element in several case studies, where they also targeted the effects of the number of the strain sensors on the solution of iFEM in addition to the effects of the sensor placement and discretization of the problem domain. By the same token, iFEM has also been applied as a monitoring technique to various real-world engineering problems, including the health monitoring of a chemical tanker (Kefal & Oterkus, 2016a), or the shape-sensing and stress reconstruction of a Panamax containership (Kefal & Oterkus, 2016b), and real-time monitoring of bulk carriers (Kefal, Mayang, Oterkus & Yildiz, 2018). Miller, Manalo & Tessler (2016) used iFEM for the reconstruction of the displacements and internal loads of a half-span test wing. Additionally, Papa, Russo, Lamboglia, Del Core & Iannuzzo (2017) undertook the controlling process of an unmanned aircraft system (UAS) with the iFEM. Withal, Kefal & Yildiz (2017) analyzed different sensor deployment schemes on a wing-shaped sandwich structure. Furthermore, iFEM has also been used in order to monitor the deformations of gantry structures via utilizing the strain data from embedded FBG sensors (Liu, Zhang, Song, Zhou, Zhou & Zhou, 2018). De Mooij, Martinez & Benedictus (2019) solved benchmark problems using forward analysis, and then utilizing the data acquired from the forward analysis, conducted the inverse analysis. In their work, the numerical data collected for their inverse algorithm were provided via displacement sensors, strain sensors, or a combination of them. Li, Kefal, Oterkus & Oterkus (2020) performed SHM using the iQS4 element, where they acquired the necessary input data for the inverse analysis numerically and studied cases involving static and dynamic loading while using the same sensor placement schemes for both types of loading. It was shown that iFEM provides more accurate results in the case of static loading than in the case of dynamic loading. Esposito & Gherlone (2020) implemented iFEM along with Ko's displacement method and MM, to a rather complicated aerospace structure, and through a comparative study, determined that in terms of precision, iFEM provides the best results; however, it requires more sensor data than the other two approaches. Also, Oboe, Colombo, Sbarufatti & Giglio (2021b) introduced a 'simple iFEM model', where they modeled a complex structure with simplifications, specifically by simplifying the parts which do not contribute

much to the stiffness of the structure and modeling them in detail, further complicates the simulations as they introduce numerical errors in the calculations. In the so-called simple model, the boundary conditions were applied through the definition of a set of weighting coefficients that are calibrated in a way to model the real behavior of the structure when subjected to these constraints. Moreover, through coupling experimental analysis with numerical simulations, Kefal, Tabrizi, Tansan, Kisa & Yildiz (2021) solved the shape-sensing problem for composite and sandwich structures in a case study including time-dependent loading. Abdollahzadeh, Tabrizi, Kefal & Yildiz (2021) conducted a comparative study focusing on the efficiency of iFEM-RZT and iFEM-FSDT (first-order shear deformation theory) when applied to case studies incorporating moderately thick laminates, and concluded that the former is more effective. Moreover, in order to find the best sensor placement scheme, they used pre-extrapolated strain measurements with different polynomial degrees.

Another crucial advantage of the iFEM is that it is also an effective tool for damage detection. Numerous studies have focused on damage detection and crack propagation recently. Specifically, as outlined in Tabrizi, Khan, Massarwa, Zanjani, Ali, Demir & Yildiz (2019), composite materials that are widely used in aviation and maritime industries, are susceptible to various modes of failure, and damage mechanisms in composite materials can be more intricate compared to metals. Among the efforts undertaken for damage detection using iFEM, Colombo, Sbarufatti & Giglio (2019) made a comparison between the results of the analysis when using inverse-plane elements and when using inverse-shell elements. Also, they analyzed the effects of the size and shape of the defect in the results of the damage sensitivity of iFEM as well as the overall results. Furthermore, in Abdollahzadeh et al. (2020), the performance of the various inverse-shell elements developed in Kefal (2019); Kefal et al. (2016); Tessler & Spangler (2004) were assessed. It was seen that in terms of damage detection, iCS8 proves to be better than flat elements (iMIN3 and iQS4). Other studies, which have consolidated the superior capability of iFEM concerning damage monitoring, include Li, Kefal, Cerik & Oterkus (2020) where they employed iFEM for identification of dent damage. Their effort included several case studies, where the input data for iFEM was generated numerically. Moreover, they presented results for damage index (a novel damage index was defined), as well as von Mises strain contours, considering that the damage index alone might be deceiving. Damage detection potential of iFEM has also been studied in the work presented by Roy, Gherlone, Surace & Tessler (2021). By the same token, iFEM has proven to be a viable method for studying damage in laminated composites. Several applications of iFEM have been conducted to verify the inverse numerical results against the experimental test data, as presented in Colombo, Oboe, Sbarufatti, Cadini, Russo

& Giglio (2021) and Kefal, Tabrizi & Yildiz (2021). However, the mere application of iFEM to crack monitoring problems in laminated shells is impractical given that a realistic insight into the damage for this type of material is achieved by studying the through-the-thickness profile of the defect. This phenomenon calls for a more advanced set of kinematic relations that incorporate the RZT (Tessler, Di Sciuva & Gherlone, 2010). This new formulation, known as iFEM-RZT herein, employed by Cerracchio, Gherlone, Di Sciuva & Tessler (2015), facilitated the implementation of iFEM to thick shells, nevertheless, the study was not comprehensive adequately as the through-the-thickness profile of the stress/strain fields lacked accuracy. In this context, Kefal, Tessler & Oterkus (2017) addressed the issue by adding complementary terms to the weighted-least-squares functional, which in turn led to a precise through-the-thickness deformation reconstruction for laminated shells.

The groundwork for this study is primarily established in the work of Kefal & Tessler (2021). In the present work, the capability of the iFEM for shape-sensing is assessed, also it is evaluated in terms of damage detection and approximating the shape of the flaw. For this purpose, several numerical examples, which become more complicated in the order that are presented, have been solved. The first three case studies are solved by utilization of the iFEM solely, whereas the last two case studies have utilized iFEM-RZT. The example problems are namely an isotropic plate subjected to tensile loading, a composite part with bending load, similarly a T-beam subjected to a bending load case, a cross-ply composite plate with torsional load, and a curved composite panel subjected to axial loading, where in all cases, the problem domain includes single or multiple pre-defined defected areas. For these analyses, inverse-plane elements and inverse-shell elements have been used. The in-situ strain measurements are collected numerically through running high fidelity forward analysis. Different sensor deployment models, dense and sparse, have been implemented. In order to quantify damage, a damage index is defined. By the same token, the damage sensitivity plots based on the maximum calculated damage indices have been plotted. This study shows that both the inverse-plane element and the inverse-shell element are effectively capable of predicting the location as well as the shape of the flawed areas in the structure, independent of the material models used (isotropic or orthotropic) and loading information. Furthermore, the iFEM-RZT coupling exhibits promising results with regards to its potential as an efficient tool to identify damage mechanisms such as delamination in composite materials even when a sparse sensor placement scheme is devised, and through-the-thickness strain data are collected from a remote location to the defected zone.

1.1 Contribution Beyond the State of the Art

The main focus of the present effort is on exploitation of the abilities of the iFEM in order to develop a viable tool for damage detection. Particularly, damage mechanisms such as delamination in laminated composite materials are among the most common and critical damage types in this category of materials. Therefore, this study suggests a novel formulation that enables a layer-wise study and damage detection procedure. In this regard, through utilization of the section strains, membrane and bending strains, for calculating their respective equivalent von Mises strains, membrane and twisting damage indices are defined. These two indices help identify a region with high probability of structural damage. Then, through obtaining the von Mises strain for each layer in the laminated structure, the ply with the highest damage index, i.e., the lamina that contains (delamination) damage, is determined.

One of the significant advantages of this novel delamination damage strategy is that it is robust in terms of adapting to experimental problems. The experimental strain data obtained using strain sensors (rosettes and FBG) are processed simultaneously in this algorithm, and the output is an accurate prediction of the shape and location (in-plane and through-the-thickness) of the damage in the composite material.

2. INVERSE FINITE ELEMENT METHOD FORMULATION

The theoretical and mathematical framework associated with iFEM is provided in this section. The material presented in this section include the governing mathematical relations for the inverse-plane element, inverse-shell element, and the formulation for the inverse-shell element coupled with RZT, referred to as iRZT4 (Abdollahzadeh et al., 2021). In order to perform the calculations for the aforementioned inverse element types, three coordinate systems are utilized: a global coordinate system denoted by (X, Y, Z), a local coordinate system denoted by (x, y, z), and for the sake of computationally effective numerical operations, an isoparametric coordinate system is also defined as (s, t).

2.1 Quadrilateral Inverse-Plane Element

The inverse-plane element consists of four nodes and each node has two membrane degrees of freedom, namely translation degrees of freedom along X-axis and Y-axis, per node. The formulation for iFEM is developed utilizing the weighted least squares functional defined in terms of the error between the measured (experimental) strains and numerically calculated strains, i.e., the strains that are obtained using the inverse approach. Figure 2.1 shows the global coordinate system and the positive degrees of freedom associated with an individual node for the inverse-plane element. On the other hand, Figure 2.2 shows the local and isoparametric coordinate systems for this inverse element type. Additionally, a set of relations must be established between the local and isoparametric coordinates for mapping. In this regard, the position of every point in the local coordinate system can be written in terms of s and t.

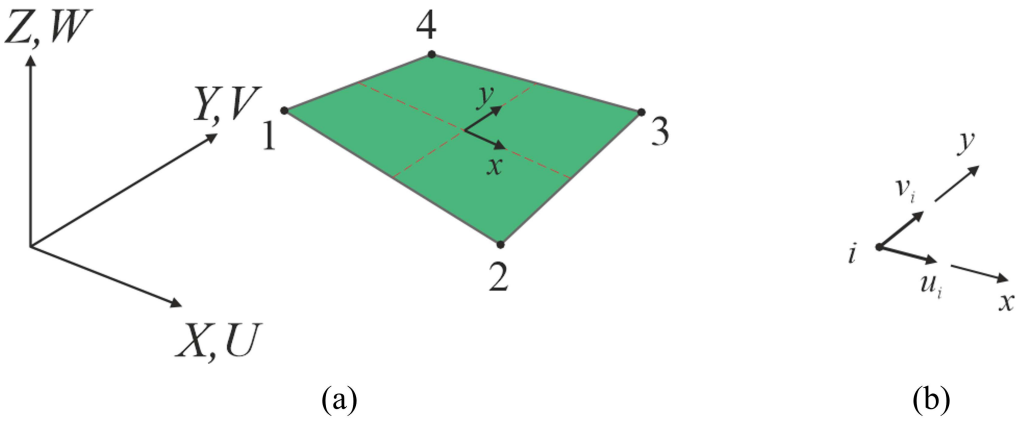

Figure 2.1 (a) Global coordinate system for the inverse-plane element; (b) Positive degrees of freedom for the i-th node of the inverse-plane element.

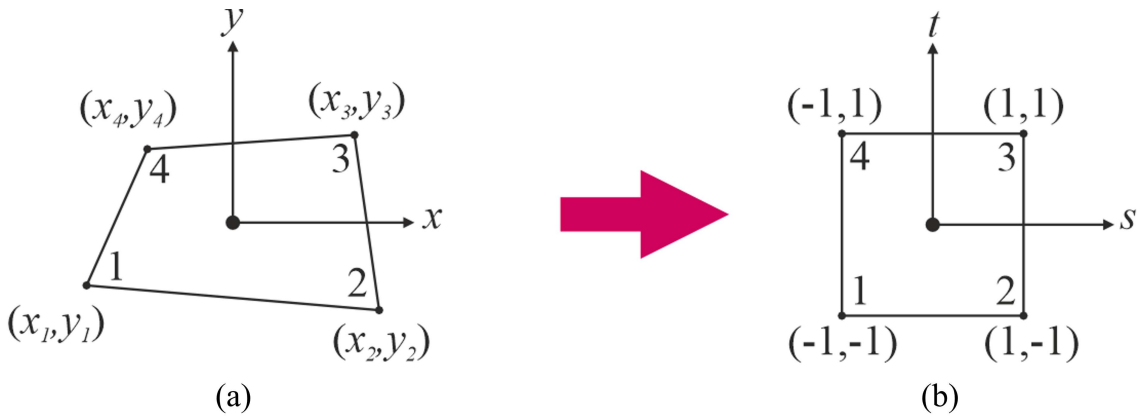

Figure 2.2 (a) Local coordinate system for the inverse-plane element; (b) Isoparametric coordinate system.

$$x \equiv x(s,t) = \sum_{i=1}^{4} N_i x_i \tag{2.1a}$$

$$y \equiv y(s,t) = \sum_{i=1}^{4} N_i y_i \tag{2.1b}$$

where x_i and y_i are the horizontal and vertical components of the local nodal coordinates of the inverse-plate element, respectively. Furthermore, N_i represent the shape functions, which are calculated for each of the nodes in the element in the isoparametric coordinate system for the inverse-plane element. The shape functions for the inverse-plane element are provided in Appendix A. To this end, the horizontal component of membrane displacement, u, as well as the vertical component, v, can be defined in the following manner:

$$u = \sum_{i=1}^{4} N_i u_i \tag{2.2a}$$

$$v = \sum_{i=1}^{4} N_i v_i \tag{2.2b}$$

with u_i representing the positive horizontal translations of nodal degrees of freedom, and v_i being the positive vertical translations of nodal degrees of freedom for an individual inverse-plane element. Subsequently, for this type of element, membrane strain terms are calculated using the strain-displacement relations, in the following manner:

$$\varepsilon_{xx} = \frac{\partial u}{\partial x} \tag{2.3a}$$

$$\varepsilon_{yy} = \frac{\partial v}{\partial y} \tag{2.3b}$$

$$\gamma_{xy} = \frac{\partial u}{\partial y} + \frac{\partial v}{\partial x} \tag{2.3c}$$

where the terms ε_{xx}, ε_{xx}, and γ_{xy}, that are calculated by taking the first derivative of the displacement terms with respect to the local coordinate system, are normal membrane strain term along x-axis, normal membrane strain term along y-axis, and in-plane membrane shear strain term (xy plane). Hence, the membrane strain vector at the element level is defined as a function of the displacements which are calculated locally, $\mathbf{u}^e$:

$$\mathbf{e}(\mathbf{u}^e) = \begin{Bmatrix} \varepsilon_{xx} \\ \varepsilon_{yy} \\ \gamma_{xy} \end{Bmatrix} = \mathbf{B}_p^m \mathbf{u}^e \tag{2.4a}$$

where

$$\mathbf{u}^e = \begin{bmatrix} \mathbf{u}_1^e & \mathbf{u}_2^e & \mathbf{u}_3^e & \mathbf{u}_4^e \end{bmatrix}^T \tag{2.4b}$$

$$\mathbf{u}_i^e = \begin{bmatrix} u_i & v_i \end{bmatrix}^T \quad (i = 1, 2, 3, 4) \tag{2.4c}$$

In the above equation, $\mathbf{e}(\mathbf{u}^e)$ is the membrane strain vector, and $\mathbf{B}_p^m$ is the notation for the membrane strain-displacement matrix for the inverse-plane element (Appendix A).

2.1.1 Strain Data Acquisition for Inverse-Plane Element

Owing to the fact that the inverse-plane element does not incorporate any form of strain other than the membrane strain, in conjunction with the fact that rotations cannot be calculated using this type of inverse element, the input strain data required for the inverse method are merely the membrane strains that are measured through mounting sensors only on one of the surfaces of the test samples. Additionally, in this type of inverse element, thickness effects are negligible, hence, acquiring strain data from only one of the bounding surfaces of the element is sufficient to provide the iFEM algorithm with the required input data (Figure 2.3). In this context, the measured membrane stiffness data for the inverse-plane element is defined as:

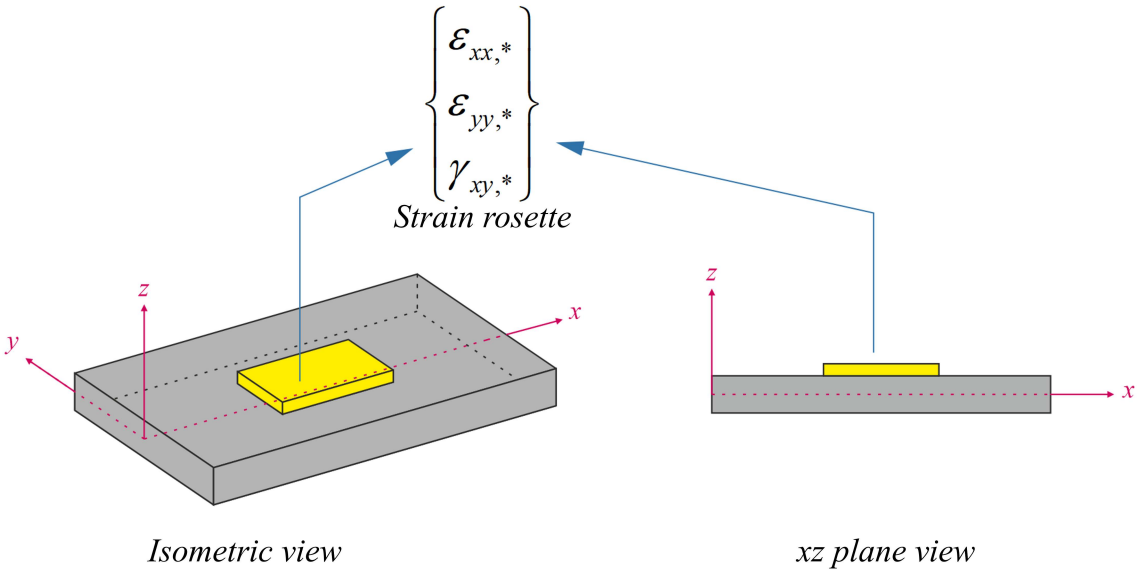

Figure 2.3 Strain data collection utilizing strain rosette with the inverse-plane assumption.

$$\mathbf{e}_i^{\varepsilon} = \begin{Bmatrix} \varepsilon_{xx,*} \\ \varepsilon_{yy,*} \\ \gamma_{xy,*} \end{Bmatrix} \quad (i = 1, n) \tag{2.5}$$

where the expression $\mathbf{e}_i^{\varepsilon}$ is used to show the in-situ strain data obtained from the plane structure. Moreover, $\varepsilon_{xx,*}$, $\varepsilon_{yy,*}$, and $\gamma_{xy,*}$ are the experimentally measured normal strain along x-axis, normal strain along y-axis, and in-plane shear strain in the xy plane. Also, n resembles the number of the data acquisition locations, i.e., the number of the sensors mounted on the test sample.

2.1.2 Weighted Least Squares Functional for Inverse-Plane Element

As it was discussed earlier, the iFEM model is based on the minimization of a weighted least squares functional, defined as the difference between the in-situ strain data, $\mathbf{e}^{\varepsilon}$, and the numerically calculated strains Eq. (2.4a), $\mathbf{e}(\mathbf{u}^e)$. Hence, for a single inverse-plane element, the functional is minimized through finding the optimum solution for the functional below:

$$\Phi_p^e(\mathbf{u}^e) = w_e \|\mathbf{e}(\mathbf{u}^e) - \mathbf{e}^{\varepsilon}\|^2 \tag{2.6}$$

In this equation, Φ_p^e is the functional for an individual inverse-plane element, defined in terms of the locally calculated displacements, $\mathbf{u}^e$. By extending Eq. (2.6), it can be written that:

$$\|\mathbf{e}(\mathbf{u}^e) - \mathbf{e}^{\varepsilon}\|^2 = \frac{1}{n} \iint_{A^e} \sum_{i=1}^{n} (\mathbf{e}(\mathbf{u}^e)_i - \mathbf{e}_i^{\varepsilon})^2 \, dx \, dy \tag{2.7}$$

This equation shows the normal Euclidean norm of the error functional. Furthermore, in Eq. (2.6), the term w_e is a weighting coefficient whose value is dependent on the availability of the sensor data at a specific location on the structure, i.e., if strain data is available for a certain element, then $w_e = 1$, however, if no sensor data is available for the inverse element, then for that element, $w_e = \alpha$ where α is selected very small relative to one, e.g., 10^{-3}. This coefficient is chosen such that it does not affect the solution of the problem. Moreover, the term A^e shows the surface area of the element, over which, the integral in Eq. (2.7) is calculated. In order to minimize the error, the local displacements corresponding to the minimum error must be calculated. Thus, the derivative of Eq. (2.6) is calculated with respect to the local displacement, i.e.,

$$\frac{\partial \Phi_p^e(\mathbf{u}^e)}{\partial \mathbf{u}^e} = 0 \tag{2.8a}$$

which yields the following:

$$\mathbf{k}^e \mathbf{u}^e = \mathbf{f}^e \tag{2.8b}$$

Here, $\mathbf{k}^e$ is the element stiffness matrix for the inverse-plane element, and by substituting Eq. (2.4) in Eq. (2.8), it can be derived as:

$$\mathbf{k}^e = \iint\limits_{A^e} w_e \left(\mathbf{B}_p^m\right)^T \mathbf{B}_p^m \, dx \, dy \tag{2.9}$$

and $\mathbf{f}^e$ is the element force vector for the inverse-plane element, and by using Eq. (2.4) with Eq. (2.8), it is defined as:

$$\mathbf{f}^e = \frac{1}{n} \iint\limits_{A^e} \sum_{i=1}^{n} w_e \left(\mathbf{B}_p^m\right)^T \mathbf{e}_i^{\varepsilon} \, dx \, dy \tag{2.10}$$

2.2 Quadrilateral Inverse-Shell Element

The theoretical framework for the inverse-shell element, known as iQS4, was set by Kefal et al. (2016). In contrast to the inverse-plane element, for the inverse-shell element, the effects of curvature and thickness of the shells must be considered. In this regard, other than in-plane membrane degrees of freedom, out-of-plane translations and rotations will be taken into consideration, too. Therefore, for each quadrilateral inverse-shell element, there are four nodes per element, and six degrees of freedom per node. As it is mentioned in Kefal et al. (2016) for this inverse element, the presence of an artificial drilling rotation degree of freedom, ensures that the calculated solutions are not singular. Figures 2.4-2.5 illustrate the configuration of an individual inverse-shell element with reference to the global, local, and isoparametric coordinate systems. The mapping relations between the local coordinate system and the isoparametric coordinate system provided in Eq. (2.1) are also applicable to this type of inverse element. However, the calculation of the displacement terms is different from those given in Eq. (2.2) due to the presence of rotation terms. In this context, the membrane displacements can be calculated using the following:

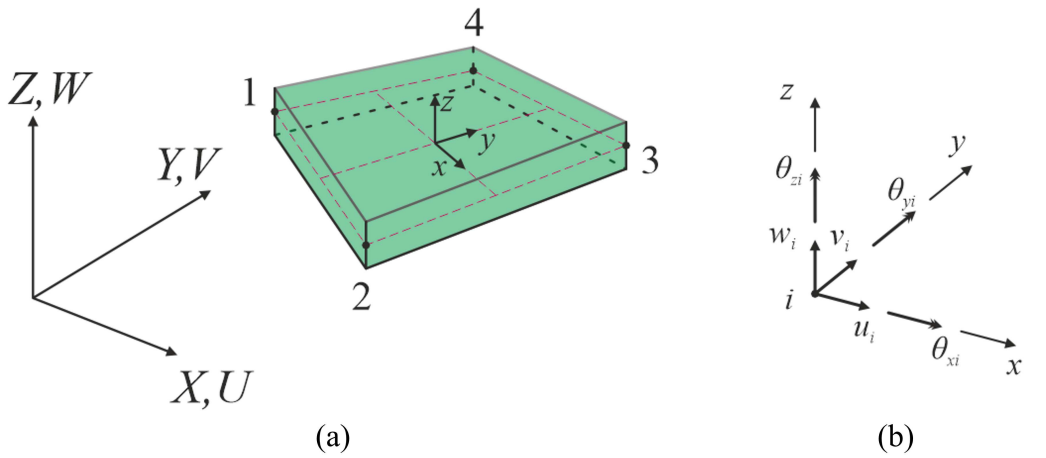

Figure 2.4 (a) Global coordinate system for the inverse-shell element, iQS4; (b) Positive degrees of freedom for the i-th node of the inverse-shell element, iQS4.

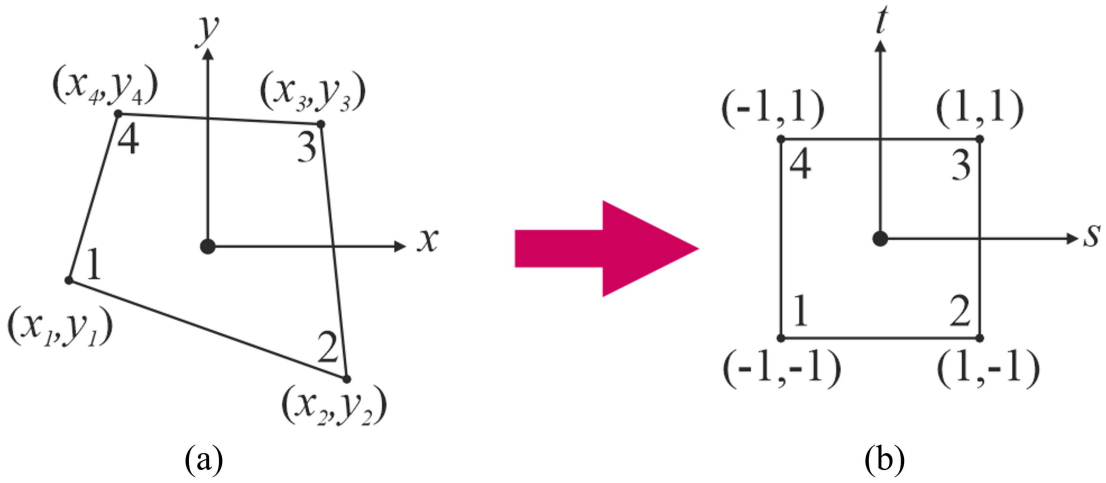

Figure 2.5 (a) Local coordinate system for the inverse-shell element, iQS4; (b) Isoparametric coordinate system.

$$u = \sum_{i=1}^{4} N_i u_i + \sum_{i=1}^{4} L_i \theta_{zi} \tag{2.11a}$$

$$v = \sum_{i=1}^{4} N_i v_i + \sum_{i=1}^{4} M_i \theta_{zi} \tag{2.11b}$$

Here, L_i and M_i are shape functions that are used to build a connection between membrane displacements and hierarchical artificial drilling degree of freedom, θ_{zi} which is deemed to be positive in clockwise rotations. It must also be noted that the membrane displacements are not only dependent on the positive translations, but they also rely on the artificial degree of freedom. As it was mentioned earlier,

each node of the inverse-shell element consists of six degrees of freedom; to this end, the degrees of freedom associated with displacement along z-axis, w, rotation about x-axis, θ_x, and rotation about y-axis, θ_y, are interpolated using their corresponding nodal values in Eq. (2.12), respectively (Tessler & Hughes, 1983):

$$w = \sum_{i=1}^{4} N_i w_i - \sum_{i=1}^{4} L_i \theta_{xi} - \sum_{i=1}^{4} M_i \theta_{yi} \tag{2.12a}$$

$$\theta_x = \sum_{i=1}^{4} N_i \theta_{xi} \tag{2.12b}$$

$$\theta_y = \sum_{i=1}^{4} N_i \theta_{yi} \tag{2.12c}$$

In the equations above, w_i are the nodal displacements along z-axis, whereas θ_x and θ_y are the nodal rotations about the x-axis and y-axis, respectively. Utilizing Eqs. (2.11-2.12) together, the displacement terms for each material point can be obtained:

$$u_x(x, y, z) \equiv u_x = u + z\theta_y \tag{2.13a}$$

$$u_y(x, y, z) \equiv u_y = v - z\theta_x \tag{2.13b}$$

$$u_z(x, y, z) \equiv u_z = w \tag{2.13c}$$

with u_x denoting displacement along x-axis, u_y displacement along y-axis, and u_z being the notation for z-displacement of a material point in the inverse-shell element, iQS4. Using the information acquired in Eq. (2.13), the membrane/bending strain and transverse-shear strain components are calculated as:

$$\varepsilon_{xx} = \frac{\partial u_x}{\partial x} = \frac{\partial u}{\partial x} + z\frac{\partial \theta_y}{\partial x} \tag{2.14a}$$

$$\varepsilon_{yy} = \frac{\partial u_y}{\partial y} = \frac{\partial v}{\partial y} - z\frac{\partial \theta_x}{\partial y} \tag{2.14b}$$

$$\gamma_{xy} = \frac{\partial u_y}{\partial x} + \frac{\partial u_x}{\partial y} = \frac{\partial v}{\partial x} + \frac{\partial u}{\partial y} + z\left(\frac{\partial \theta_y}{\partial y} - \frac{\partial \theta_x}{\partial x}\right) \tag{2.14c}$$

$$\gamma_{xz} = \frac{\partial u_z}{\partial x} + \frac{\partial u_x}{\partial z} = \frac{\partial w}{\partial x} + \theta_y \tag{2.14d}$$

$$\gamma_{yz} = \frac{\partial u_z}{\partial y} + \frac{\partial u_y}{\partial z} = \frac{\partial w}{\partial y} - \theta_x \tag{2.14e}$$

where, γ_{xz} is the transverse-shear strain in xz plane, and γ_{yz} is the transverse-shear strain in yz plane. The strain-displacement relations can be established by further utilization of the outcome of Eq. (2.14),

$$\mathbf{e}(\mathbf{u}^e) + z\mathbf{k}(\mathbf{u}^e) = \begin{Bmatrix} \varepsilon_{xx} \\ \varepsilon_{yy} \\ \gamma_{xy} \end{Bmatrix} = \mathbf{B}_s^m \mathbf{u}^e + z\mathbf{B}^b \mathbf{u}^e \tag{2.15a}$$

$$\mathbf{g}(\mathbf{u}^e) = \begin{Bmatrix} \gamma_{xz} \\ \gamma_{yz} \end{Bmatrix} = \mathbf{B}^s \mathbf{u}^e \tag{2.15b}$$

with $\mathbf{u}^e$ being the element (local) displacement vector and is similar to the term for the inverse-plane element given in Eq. (2.4b), however, the nodal displacements are different from those provided in Eq. (2.4c):

$$\mathbf{u}^e = \begin{bmatrix} u_i & v_i & w_i & \theta_{xi} & \theta_{yi} & \theta_{zi} \end{bmatrix}^T \quad (i = 1, 2, 3, 4) \tag{2.15c}$$

here, $\mathbf{k}(\mathbf{u}^e)$ denotes the bending strains, and $\mathbf{g}(\mathbf{u}^e)$ is used for showing the transverse-shear strains. Additionally, as can be seen in Eq. (2.15), three different strain-displacement matrices have been used, which correspond to the three different strain categories, i.e., $\mathbf{B}_s^m$ is used for membrane strains for the inverse-shell element, $\mathbf{B}^b$ for bending strains, and $\mathbf{B}^s$ for transverse-shear strains. For the shape functions and strain-displacement matrices, refer to Appendix A.

2.2.1 Strain Data Acquisition for Inverse-Shell Element

Given that the inverse-shell element in addition to membrane displacements accounts for the curvature data of the test sample as well, strain data from both bounding surfaces of the test specimen is required to be used in the iFEM algorithm. Hence, the in-situ strain data measured from the top and bottom surfaces of the shell can be decomposed into two separate vectors, constituting the membrane strains, and bending strains. Similar to the procedure for the inverse-plane element, assuming that strain data are available discretely at a number of n locations over the domain of interest, it can be written that:

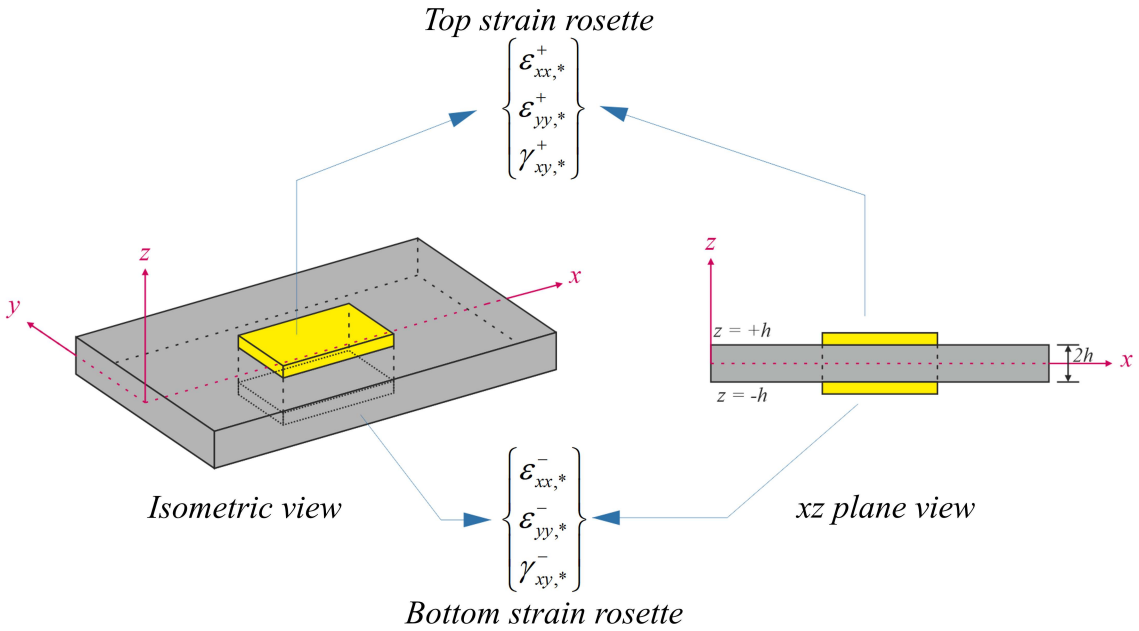

Figure 2.6 Strain data collection utilizing strain rosettes with the inverse-shell assumption.

$$\mathbf{e}_i^{\varepsilon} = \frac{1}{2}\begin{Bmatrix} \varepsilon^{+}_{xx,*} + \varepsilon^{-}_{xx,*} \\ \varepsilon^{+}_{yy,*} + \varepsilon^{-}_{yy,*} \\ \gamma^{+}_{xy,*} + \gamma^{-}_{xy,*} \end{Bmatrix} \quad (i = 1, n) \tag{2.16a}$$

$$\mathbf{k}_i^{\varepsilon} = \frac{1}{2h}\begin{Bmatrix} \varepsilon^{+}_{xx,*} - \varepsilon^{-}_{xx,*} \\ \varepsilon^{+}_{yy,*} - \varepsilon^{-}_{yy,*} \\ \gamma^{+}_{xy,*} - \gamma^{-}_{xy,*} \end{Bmatrix} \quad (i = 1, n) \tag{2.16b}$$

where $\mathbf{e}_i^{\varepsilon}$ is the measured membrane strain, and $\mathbf{k}_i^{\varepsilon}$ is the measured bending strain. It should also be mentioned that $\varepsilon^{+}_{xx,*}$, $\varepsilon^{+}_{yy,*}$, and $\gamma^{+}_{xy,*}$ are the strain measurements

made by the sensors mounted on the top surface of the shell, whereas $\varepsilon^{-}_{xx,*}$, $\varepsilon^{-}_{yy,*}$, and $\gamma^{-}_{xy,*}$ are measured from the bottom surface of the shell. In addition, the term $2h$ used in Eq. (2.16b) is the thickness of the shell.

2.2.2 Weighted Least Squares Functional for Inverse-Shell Element

The weighted least squares functional for the iQS4 element is defined as the sum of the error terms defined between the measured and numerically calculated values of the membrane, bending, and transverse-shear strains. In this regard, for an individual inverse-shell element, the functional will be an extended version of Eq. (2.6):

$$\Phi^e_s(\mathbf{u}^e) = w_e\|\mathbf{e}(\mathbf{u}^e) - \mathbf{e}^\varepsilon\|^2 + w_k\|\mathbf{k}(\mathbf{u}^e) - \mathbf{k}^\varepsilon\|^2 + w_g\|\mathbf{g}(\mathbf{u}^e) - \mathbf{g}^\varepsilon\|^2 \tag{2.17}$$

The expression $\mathbf{g}^\varepsilon$ is used to resemble the measured in-situ transverse-shear strains. w_k and w_g are the weighting coefficients associated with those terms of the error functional corresponding to bending and transverse-shear, respectively. Each of the norms can be written in the following manner:

$$\|\mathbf{e}(\mathbf{u}^e) - \mathbf{e}^\varepsilon\|^2 = \frac{1}{n}\iint\limits_{A^e}\sum_{i=1}^{n}\left(\mathbf{e}(\mathbf{u}^e)_i - \mathbf{e}^\varepsilon_i\right)^2 dx\,dy \tag{2.18a}$$

$$\|\mathbf{k}(\mathbf{u}^e) - \mathbf{k}^\varepsilon\|^2 = \frac{(2h)^2}{n}\iint\limits_{A^e}\sum_{i=1}^{n}\left(\mathbf{k}(\mathbf{u}^e)_i - \mathbf{k}^\varepsilon_i\right)^2 dx\,dy \tag{2.18b}$$

$$\|\mathbf{g}(\mathbf{u}^e) - \mathbf{g}^\varepsilon\|^2 = \frac{1}{n}\iint\limits_{A^e}\sum_{i=1}^{n}\left(\mathbf{g}(\mathbf{u}^e)_i - \mathbf{g}^\varepsilon_i\right)^2 dx\,dy \tag{2.18c}$$

For the inverse-shell elements with in-situ strain data available within their domain, the weighting coefficients are set as $w_e = w_k = w_g = 1$, whereas for the inverse elements with no measured strain data available, these coefficients are set as a very small value relative to one, i.e., $w_e = w_k = w_g = \alpha$ (e.g., $\alpha = 10^{-5}$). The functional provided in Eq. (2.17) is minimized subjected to the local displacements, $\mathbf{u}^e$:

$$\frac{\partial\Phi^e_s(\mathbf{u}^e)}{\partial\mathbf{u}^e} = 0 \tag{2.19a}$$

that gives:

$$\mathbf{k}^e \mathbf{u}^e = \mathbf{f}^e \tag{2.19b}$$

where $\mathbf{k}^e$ is the element stiffness matrix for the inverse-shell element and is defined as:

$$\mathbf{k}^e = \iint\limits_{A^e} \left(w_e \left(\mathbf{B}_s^m\right)^T \mathbf{B}_s^m + (2h)^2 w_k \left(\mathbf{B}^b\right)^T \mathbf{B}^b + w_g \left(\mathbf{B}^s\right)^T \mathbf{B}^s \right) dx\, dy \tag{2.20}$$

and $\mathbf{f}^e$ is the element force vector for the inverse-shell element and is defined as:

$$\mathbf{f}^e = \frac{1}{n} \iint\limits_{A^e} \sum_{i=1}^{n} \left(w_e \left(\mathbf{B}_s^m\right)^T \mathbf{e}_i^\varepsilon + (2h)^2 w_k \left(\mathbf{B}^b\right)^T \mathbf{k}_i^\varepsilon + w_g \left(\mathbf{B}^s\right)^T \mathbf{g}_i^\varepsilon \right) dx\, dy \tag{2.21}$$

By comparing Eqs. (2.9-2.10) with Eqs. (2.20-2.21), the more sophisticated mathematical basis of the iQS4 element, which emanates from employing the curvature data and transverse-shear terms, is highlighted.

2.3 Quadrilateral Inverse-Shell Element Coupled with RZT

The fundamental difference between the formulation for the iQS4 element and the iRZT4 formulation stems from the definition of the zigzag rotations which affect the expressions for the displacements of the material points. With the iRZT4 assumption, for a laminated material with a total of N layers, the displacements of the material points at each layer k are given as the following:

$$u_x^{(k)}(x, y, z) = u + z\theta_x + \phi_x^{(k)} \psi_x \tag{2.22a}$$

$$u_y^{(k)}(x, y, z) = v + z\theta_y + \phi_y^{(k)} \psi_y \tag{2.22b}$$

$$u_z(x, y) = w \tag{2.22c}$$

consequently,

$$\mathbf{u}(x,y) \equiv \mathbf{u} = \begin{bmatrix} u & v & w & \theta_x & \theta_y & \psi_x & \psi_y \end{bmatrix}^T \tag{2.22d}$$

The first three terms, namely (u, v, w) are the displacement terms associated with translations, θ_x, θ_y are bending rotations, and ψ_x, ψ_y are zigzag rotations based on RZT theory. According to RZT, through-the-thickness displacements of each ply in a laminate may vary drastically from one layer to another, hence, a set of piecewise functions are defined which account for the zigzag rotations of the laminae. These functions are provided as:

$$\phi_i^{(k)} = z\beta_i^{(k)} + \alpha_i^{(k)} \quad (i = x, y) \tag{2.23a}$$

where the slope of the piecewise function defined through the thickness of the lamina, $\beta_i^{(k)}$, is given as:

$$\beta_i^{(k)} = \frac{G_i}{Q_{ii}^{(k)}} - 1 \quad (i = x, y; k = 1, 2, ..., N) \tag{2.23b}$$

the constant $\alpha_i^{(k)}$ is defined to maintain the continuity of the piecewise zigzag lines through the thickness of the laminate:

$$\alpha_i^{(k)} = \beta_i^{(k)} h + \sum_{j=2}^{k} 2h^{(j-1)} \left(\frac{G_i}{Q_{ii}^{(k)}} - \frac{G_i}{Q_{ii}^{(j-1)}} \right) \quad (i = x, y) \tag{2.23c}$$

and the term G_i is the average shear stiffness of the layered material:

$$G_i = \left(\frac{1}{h} \sum_{j=1}^{N} \frac{h^{(j)}}{Q_{ii}^{(j)}} \right) \quad (i = x, y) \tag{2.23d}$$

In the above set of equations, $2h^{(k)}$ is used to denote the thickness of a single lamina. In addition, $Q_{xx}^{(k)}$ is the transformed shear modulus of the lamina for xz plane, whereas, $Q_{yy}^{(k)}$ is the transformed shear modulus of the lamina for yz plane. The elasticity relations for the k-th ply of the laminate is established in the order presented below:

$$\boldsymbol{\varepsilon}^{(k)} \equiv \begin{Bmatrix} \varepsilon_{xx}^{(k)} \\ \varepsilon_{yy}^{(k)} \\ \gamma_{xy}^{(k)} \end{Bmatrix} = \mathbf{e}(\mathbf{u}) + z\boldsymbol{\kappa}(\mathbf{u}) + \boldsymbol{\mu}^{(k)}(\mathbf{u}, z) \tag{2.24a}$$

$$\boldsymbol{\gamma}^{(k)} \equiv \begin{Bmatrix} \gamma_{xz}^{(k)} \\ \gamma_{yz}^{(k)} \end{Bmatrix} = \mathbf{H}_{\gamma}^{(k)}(z)\boldsymbol{\gamma}(\mathbf{u}) + \mathbf{H}_{\eta}^{(k)}(z)\boldsymbol{\eta}(\mathbf{u}) \tag{2.24b}$$

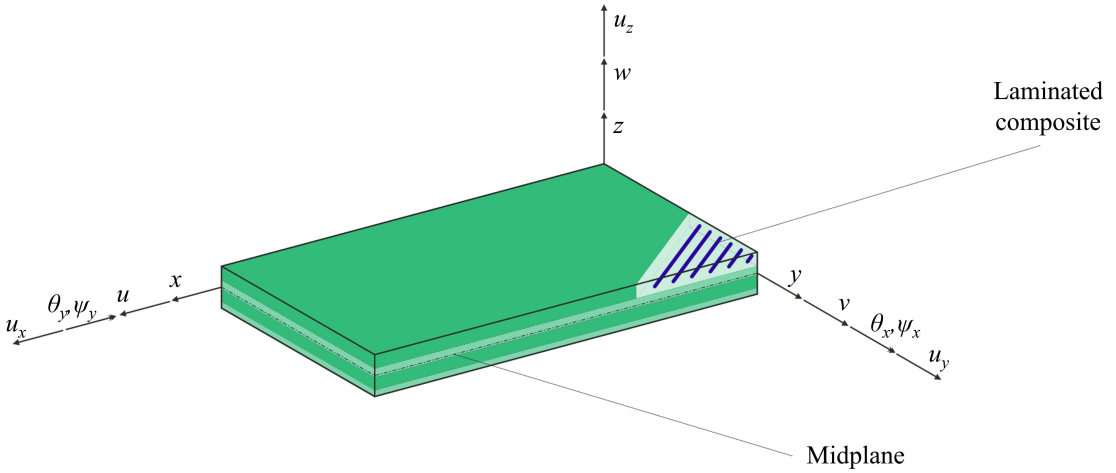

(a)

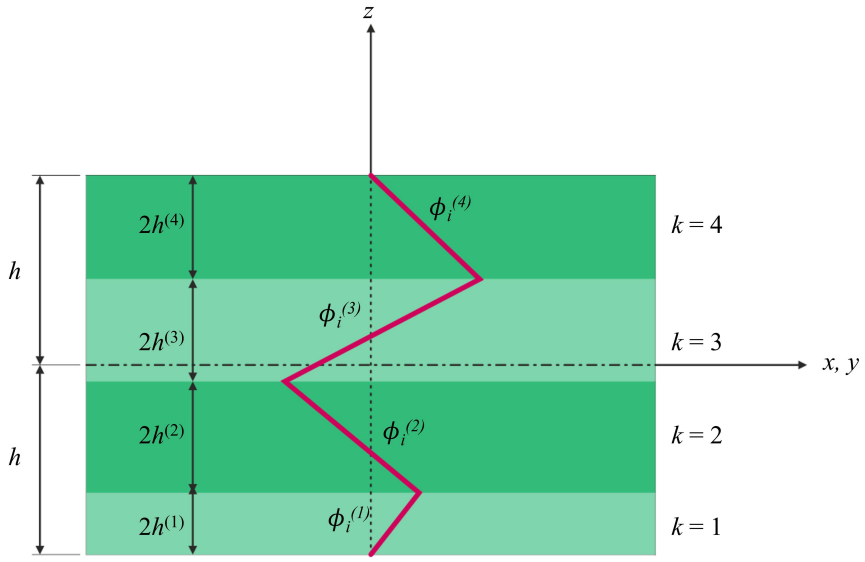

(b)

Figure 2.7 (a) Laminated composite and its kinematic variables in global Cartesian coordinates; (b) Zigzag rotations through the thickness of the laminated composite.

The in-plane membrane strain term, $\mathbf{e}(\mathbf{u})$, and the in-plane bending strain term, $\boldsymbol{\kappa}(\mathbf{u})$, and the term accounting for the strain as a result of zigzag rotations, $\boldsymbol{\mu}^{(k)}(\mathbf{u}, z)$, are:

$$\mathbf{e}(\mathbf{u}) = \begin{bmatrix} \frac{\partial u}{\partial x} & \frac{\partial v}{\partial y} & \frac{\partial u}{\partial y} + \frac{\partial v}{\partial x} \end{bmatrix}^T \tag{2.25a}$$

$$\boldsymbol{\kappa}(\mathbf{u}) = \begin{bmatrix} \frac{\partial \theta_x}{\partial x} & \frac{\partial \theta_y}{\partial y} & \frac{\partial \theta_x}{\partial y} + \frac{\partial \theta_y}{\partial x} \end{bmatrix}^T \tag{2.25b}$$

$$\boldsymbol{\mu}^{(k)}(\mathbf{u}, z) = \mathbf{H}_{\phi}^{(k)}(z) \begin{bmatrix} \frac{\partial \psi_x}{\partial x} & \frac{\partial \psi_y}{\partial y} & \frac{\partial \psi_x}{\partial y} & \frac{\partial \psi_y}{\partial x} \end{bmatrix}^T \tag{2.25c}$$

where,

$$\mathbf{H}_{\phi}^{(k)} = \begin{bmatrix} \phi_x^{(k)} & 0 & 0 & 0 \\ 0 & \phi_y^{(k)} & 0 & 0 \\ 0 & 0 & \phi_x^{(k)} & \phi_y^{(k)} \end{bmatrix} \tag{2.25d}$$

By the same token, the strain terms associated with the transverse-shear strain given in Eq. (2.24b), are calculated using the following:

$$\boldsymbol{\gamma}(\mathbf{u}) \equiv \begin{bmatrix} \gamma_x & \gamma_y \end{bmatrix}^T = \begin{bmatrix} \frac{\partial w}{\partial x} + \theta_x & \frac{\partial w}{\partial y} + \theta_y \end{bmatrix}^T \tag{2.26a}$$

$$\boldsymbol{\eta}(\mathbf{u}) = \begin{bmatrix} \gamma_x - \psi_x & \gamma_y - \psi_y \end{bmatrix}^T \tag{2.26b}$$

Furthermore, the matrices of constants, $\mathbf{H}_{\gamma}^{(k)}$ and $\mathbf{H}_{\eta}^{(k)}$, are defined as:

$$\mathbf{H}_{\gamma}^{(k)} = \begin{bmatrix} 1 + \beta_x^{(k)} & 0 \\ 0 & 1 + \beta_y^{(k)} \end{bmatrix} \tag{2.26c}$$

$$\mathbf{H}_{\eta}^{(k)} = \begin{bmatrix} -\beta_x^{(k)} & 0 \\ 0 & -\beta_y^{(k)} \end{bmatrix} \tag{2.26d}$$

The constant matrices, $\mathbf{H}_{\phi}^{(k)}$, $\mathbf{H}_{\gamma}^{(k)}$, and $\mathbf{H}_{\eta}^{(k)}$, are only functions of the thickness position of the laminate, z, and they are deemed to be constant over the in-plane domain of each ply. Conversely, membrane/bending strain terms, i.e., the section strains, are constant through the thickness of the plies and vary only over the in-plane domain. The kinematic variables presented in Eqs. (2.25a-2.25c, 2.26a-2.26b) are approximated using shape functions and their respective strain-displacement relations are as follows:

$$\chi(\mathbf{u}^e) = \mathbf{B}^{\chi}\mathbf{u}^e \quad (\chi = \mathbf{e}, \boldsymbol{\kappa}, \boldsymbol{\mu}, \boldsymbol{\gamma}, \boldsymbol{\eta}) \tag{2.27}$$

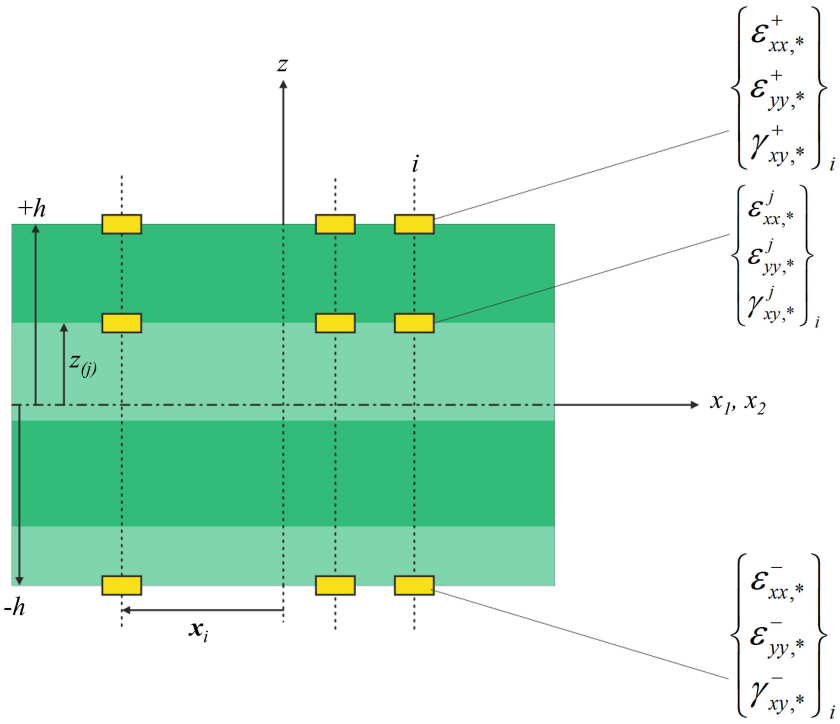

Figure 2.8 Experimental data acquisition from laminated composite with strain rosettes mounted on bounding surfaces and FGB sensors embedded within the laminate.

Experimental data used as the input for the iFEM-RZT algorithm are collected in a process similar to what was seen for the inverse-shell element. However, one important advantage of using iFEM-RZT is that its mathematical framework enables the use of interlaminar strain data, which can be acquired via embedding FBG sensors at various locations through the thickness of the composite laminate. Hence, an additional equation should be added to Eq. (2.16), which represents the experimentally collected zigzag strain data at the j-th boundary surface (between two plies) of the laminate:

$$\mathbf{m}_i^j = \boldsymbol{\varepsilon}_i^j - \mathbf{e}_i^{\varepsilon} - z_{(j)}\mathbf{k}_i^{\varepsilon} \quad (i = 1, 2, ..., n) \tag{2.28}$$

where $\boldsymbol{\varepsilon}_i^j$ is the strain at the j-th interface of the laminate measured at $z = z_{(j)}$, and the subscript i is used to show the number of data acquisition locations. Furthermore, by illustrating the experimental transverse-shear strain terms with the notations, $\boldsymbol{\Gamma}$ and $\mathbf{H}$, the weighted least squares functional can be developed over the entire volume of the problem domain as the following:

$$\begin{aligned}\Phi(\mathbf{u}) = w_e\|\mathbf{e}(\mathbf{u}) - \mathbf{e}_i^{\varepsilon}\|^2 + w_\kappa\|\boldsymbol{\kappa}(\mathbf{u}) - \mathbf{k}_i^{\varepsilon}\|^2 + w_\mu\|\boldsymbol{\mu}^{(k)}(\mathbf{u}, z_j) - \mathbf{m}^j\|^2 + \\ w_\gamma\|\boldsymbol{\gamma}(\mathbf{u}) - \boldsymbol{\Gamma}\|^2 + w_\eta\|\boldsymbol{\eta}(\mathbf{u}) - \mathbf{H}\|^2\end{aligned} \tag{2.29}$$

By incorporating Eq. (2.27) in Eq. (2.29), the functional is obtained at the element

level, $\Phi(\mathbf{u}^e)$, and by minimizing it subject to the unknown local displacements, Eq. (2.19) is repeated, hence the local stiffness matrix, $\mathbf{k}^e$, is derived as:

$$\begin{aligned}\mathbf{k}^e = \iint\limits_{A^e} \Big[& w_e \left(\mathbf{B}^e\right)^T \mathbf{B}^e + (2h)^2 w_\kappa \left(\mathbf{B}^\kappa\right)^T \mathbf{B}^\kappa + w_\mu \left(\mathbf{B}^\mu\right)^T \mathbf{B}^\mu \\ & + w_\gamma \left(\mathbf{B}^\gamma\right)^T \mathbf{B}^\gamma + w_\eta \left(\mathbf{B}^\eta\right)^T \mathbf{B}^\eta \Big] \, dx \, dy\end{aligned} \tag{2.30}$$

and the local force vector, $\mathbf{f}^e$, is:

$$\begin{aligned}\mathbf{f}^e = \frac{1}{n} \iint\limits_{A^e} \sum_{i=1}^{n} \Big[& w_e \left(\mathbf{B}^e\right)^T \mathbf{e}_i^\varepsilon + (2h)^2 w_\kappa \left(\mathbf{B}^\kappa\right)^T \mathbf{k}_i^\varepsilon + w_\mu \left(\mathbf{B}^\mu\right)^T \mathbf{m}_i^j \\ & + w_\gamma \left(\mathbf{B}^\gamma\right)^T \mathbf{\Gamma}_i + w_\eta \left(\mathbf{B}^\eta\right)^T \mathbf{H}_i \Big] \, dx \, dy\end{aligned} \tag{2.31}$$

2.4 Inverse Finite Element Method Solution

After the local (element) stiffness matrices, $\mathbf{k}^e$, and the local (element) force vectors, $\mathbf{f}^e$, are obtained for the inverse element, the same procedure must be followed for determining the solution of the inverse method, regardless of the inverse element type. Consequently, the global stiffness matrix $\mathbf{K}$, and the global force vector $\mathbf{F}$, are calculated through assembly of the transformed local stiffness matrices (Eqs. 2.9, 2.20, and 2.30) and local force vectors (Eqs. 2.10, 2.21, and 2.31).

$$\mathbf{K} = \sum_{i=1}^{numel} (\mathbf{T}^e)^T \mathbf{k}^e \mathbf{T}^e \tag{2.32a}$$

$$\mathbf{F} = \sum_{i=1}^{numel} (\mathbf{T}^e)^T \mathbf{f}^e \tag{2.32b}$$

$$\mathbf{U} = \sum_{i=1}^{numel} (\mathbf{T}^e)^T \mathbf{u}^e \tag{2.32c}$$

where $\mathbf{U}$ is the global displacement vector, and $\mathbf{T}^e$ is the mapping from the local reference frame to the global reference frame. Thereby, the equation below can be written:

$$\mathbf{KU} = \mathbf{F} \tag{2.33}$$

The solution to the shape-sensing problem is solved through calculating the global displacements from Eq. (2.33). To solve this equation in terms of the global displacements, proper boundary conditions must be applied, and through elimination of rows and columns corresponding to natural boundary conditions in the global stiffness matrix and the global force and displacement vectors, the reduced global displacement vector is obtained.

$$\mathbf{K}^R\mathbf{U}^R = \mathbf{F}^R \tag{2.34a}$$

$$\mathbf{U}^R = \left(\mathbf{K}^R\right)^{-1}\mathbf{F}^R \tag{2.34b}$$

In this equation, $\mathbf{K}^R$, $\mathbf{F}^R$, and $\mathbf{U}^R$ are the reduced global stiffness matrix, reduced global force vector, and reduced global displacement vector, respectively. The global displacement vector is then, determined by the assembly of the displacement values corresponding to constrained degrees of freedom and the reduced global displacement vector. The procedure associated with the iFEM algorithm is summarized through a step-by-step schematic flowchart presentation in Figure 2.9.

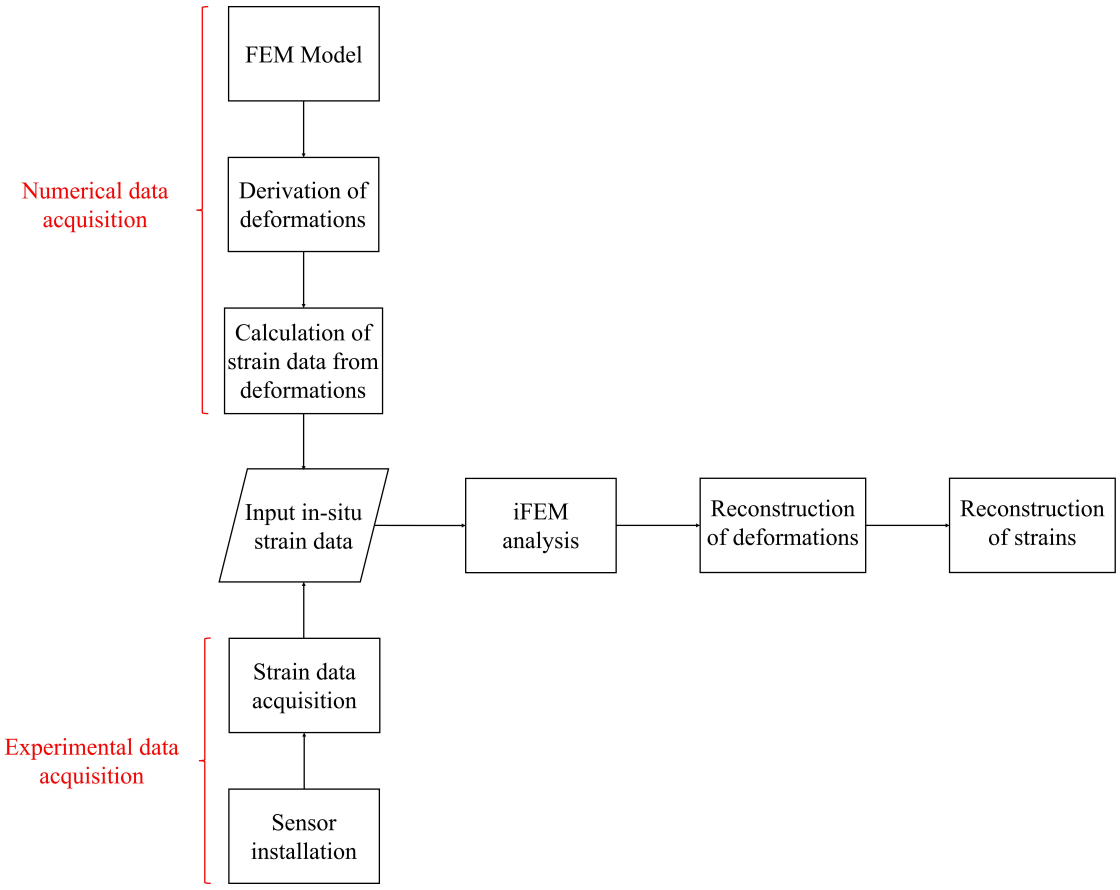

Figure 2.9 The flowchart illustrating the iFEM algorithm.

3. DAMAGE DETECTION STRATEGY

3.1 Stiffness Degradation

In the present effort, damage in the problem domain appears as a region with lesser stiffness than the overall stiffness of the structure, indicating that damaged region is pre-defined. The damaged domains are defined by introducing a stiffness degradation factor, λ (Taheri-Behrooz & Bakhshan, 2018). Assuming that for an intact element, the stiffness matrix is shown with $\mathbf{D}^U$, where the superscript U is used to identify the undamaged state of the material, the mathematical representation of the stiffness degradation is written in the following format:

$$\mathbf{D}^e = (\lambda \mathbf{I})\mathbf{D}^U \tag{3.1}$$

In this equation, $\mathbf{D}^e$ is the element stiffness, and $\mathbf{I}$ is the identity matrix with the same dimensions as the stiffness matrix. The identity matrix is used to guarantee that the degradation coefficient is multiplied only by the diagonal terms of the $\mathbf{D}^U$ matrix. It is also worth mentioning that $0 < \lambda \leq 1$, with $\lambda = 1$ corresponding to the undamaged state of the material whereas $0 < \lambda < 1$ representing the damaged state of the material.

3.2 Damage Detection

Structural damage can be determined through monitoring damage over the problem domain with high concentrations of equivalent strain measures. In the present work,

to achieve a clear understanding of the damage, equivalent strains are calculated, and consequently, a damage index is defined using the calculated equivalent strain terms for quantifying damage, as using the equivalent strains solely, might cause misinterpretations of the damage (Li et al., 2020). Damage detection procedure can be undertaken with specific considerations.

Damage monitoring can be performed in a basic manner, where through using the iFEM, the in-plane position, shape, and size of the defected region are detected. Hence, the damage index is defined as the percent error between the equivalent von Mises strain for the intact state of the material and its damaged configuration. The equivalent von Mises strain for a two-dimensional problem presented in this case study can be calculated using the equation below:

$$\varepsilon_{VM} = \sqrt{(\varepsilon_1)^2 - \varepsilon_1\varepsilon_2 + (\varepsilon_2)^2} \tag{3.2a}$$

where,

$$\begin{cases} \varepsilon_1 = \frac{\varepsilon_{xx}+\varepsilon_{yy}}{2} + \sqrt{(\frac{\varepsilon_{xx}-\varepsilon_{yy}}{2})^2 + (\frac{\gamma_{xy}}{2})^2} \\ \varepsilon_2 = \frac{\varepsilon_{xx}+\varepsilon_{yy}}{2} - \sqrt{(\frac{\varepsilon_{xx}-\varepsilon_{yy}}{2})^2 + (\frac{\gamma_{xy}}{2})^2} \end{cases} \tag{3.2b}$$

Thus, the damage index for this general assumption is achievable through the following equation:

$$DI(\varepsilon_{VM}) = \left| \frac{\varepsilon_{VM}^{U} - \varepsilon_{VM}}{\varepsilon_{VM}^{max}} \right| \times 100\% \tag{3.3}$$

with ε_{VM}^{U} being the equivalent von Mises strain calculated using iFEM with intact material assumption, and ε_{VM}^{max} denoting the maximum reconstructed von Mises strain. Although the expression derived in Eq. (3.3) is capable of detecting damage in laminated composite materials, it does not involve layer-by-layer investigation of the flaws. In this context, a more sophisticated damage detection strategy is developed within the framework of iFEM-RZT, which also makes through-the-thickness identification of the damage in materials, such as composite shells, possible; all the while, it provides this information with strain data available only at certain locations over the problem domain. Additionally, it is suitable for real-time monitoring of laminated composite structures.

After the global displacement vector is calculated using the iFEM algorithm, membrane/bending strains can be reconstructed. Similar to the damage detection strategy introduced earlier, equivalent strain measures are calculated for both the in-plane membrane strain, $\begin{bmatrix} \varepsilon_{xx} & \varepsilon_{yy} & \gamma_{xy} \end{bmatrix}^T$, and in-plane bending strain, $\begin{bmatrix} \kappa_{xx} & \kappa_{yy} & \kappa_{xy} \end{bmatrix}^T$.

$$\varepsilon_{VM}^{\chi} = \sqrt{\left(\varepsilon_1^{\chi}\right)^2 - \varepsilon_1^{\chi}\varepsilon_2^{\chi} + \left(\varepsilon_2^{\chi}\right)^2} \quad (\chi = \varepsilon, \kappa) \tag{3.4a}$$

where,

$$\begin{cases} \varepsilon_1^{\chi} = \frac{\chi_{xx}+\chi_{yy}}{2} + \sqrt{(\frac{\chi_{xx}-\chi_{yy}}{2})^2 + (\frac{\chi_{xy}}{2})^2} \\ \varepsilon_2^{\chi} = \frac{\chi_{xx}+\chi_{yy}}{2} - \sqrt{(\frac{\chi_{xx}-\chi_{yy}}{2})^2 + (\frac{\chi_{xy}}{2})^2} \end{cases} \quad (\chi = \varepsilon, \kappa) \tag{3.4b}$$

are the principal section strain terms calculated for the in-plane membrane and in-plane bending strains. The equivalent strain obtained from Eq. (3.4a) does not vary through the thickness of the layered structure, as a consequence, it can be used as a tool for identifying the in-plane location and approximating the morphology of the defected region. Additionally, employing RZT in the iFEM algorithm further enhances the damage detection capabilities of the method for detecting through-the-thickness flaws. In this regard, the average equivalent von Mises section strains for each lamina is obtained via using the following equation:

$$\bar{\varepsilon}_{VM}^{(k)} = \frac{1}{2h^{(k)}} \int_{z_{(k-1)}}^{z_{(k)}} \sqrt{\left(\varepsilon_1^{(k)}\right)^2 - \varepsilon_1^{(k)}\varepsilon_2^{(k)} + \left(\varepsilon_2^{(k)}\right)^2}\, dz \tag{3.5a}$$

with $\varepsilon_1^{(k)}$ and $\varepsilon_2^{(k)}$ being the principal section strains of each layer:

$$\begin{cases} \varepsilon_1^{(k)} = \frac{\varepsilon_{xx}^{(k)}+\varepsilon_{yy}^{(k)}}{2} + \sqrt{(\frac{\varepsilon_{xx}^{(k)}-\varepsilon_{yy}^{(k)}}{2})^2 + (\frac{\gamma_{xy}^{(k)}}{2})^2} \\ \varepsilon_2^{(k)} = \frac{\varepsilon_{xx}^{(k)}+\varepsilon_{yy}^{(k)}}{2} - \sqrt{(\frac{\varepsilon_{xx}^{(k)}-\varepsilon_{yy}^{(k)}}{2})^2 + (\frac{\gamma_{xy}^{(k)}}{2})^2} \end{cases} \tag{3.5b}$$

here, $\varepsilon_{xx}^{(k)}$, $\varepsilon_{yy}^{(k)}$, and $\gamma_{xy}^{(k)}$, are obtained from Eq. (2.24a). Now, by utilizing the equivalent section strains for the entire laminate, the in-plane location of the defected region is determined by establishing a relation similar to Eq. (3.3).

$$DI^{\chi}(\varepsilon_{VM}^{\chi}) = \left| \frac{\varepsilon_{VM}^{\chi,U} - \varepsilon_{VM}^{\chi}}{\varepsilon_{VM}^{\chi,max}} \right| \times 100\% \quad (\chi = \varepsilon, \kappa) \tag{3.6}$$

DI^{χ} is the damage index corresponding to each section strain term derived for the in-plane damage detection of the laminate. On the other hand, the location of the defect through the thickness of the laminate is determined by using the average

equivalent strain for each ply.

$$DI^{(k)}(\bar{\varepsilon}_{VM}^{(k)}) = \left| \frac{(\bar{\varepsilon}_{VM}^{(k)})^{U} - \bar{\varepsilon}_{VM}^{(k)}}{(\bar{\varepsilon}_{VM}^{(k)})^{max}} \right| \times 100\% \tag{3.7}$$

In the equation above, $DI^{(k)}$ is the damage index for each ply. The maximum value of the damage indices obtained in Eqs. (3.3, 3.6-3.7), highlights a region with an irregular distribution of the equivalent strain measure (irregular gradient of the equivalent strain measure) over the problem domain, indicating the existence of damage in that area. For a more clear understanding of the damage detection process, a flowchart is provided in Figure 3.1 that describes the road-map associated with the damage detection method developed herein.

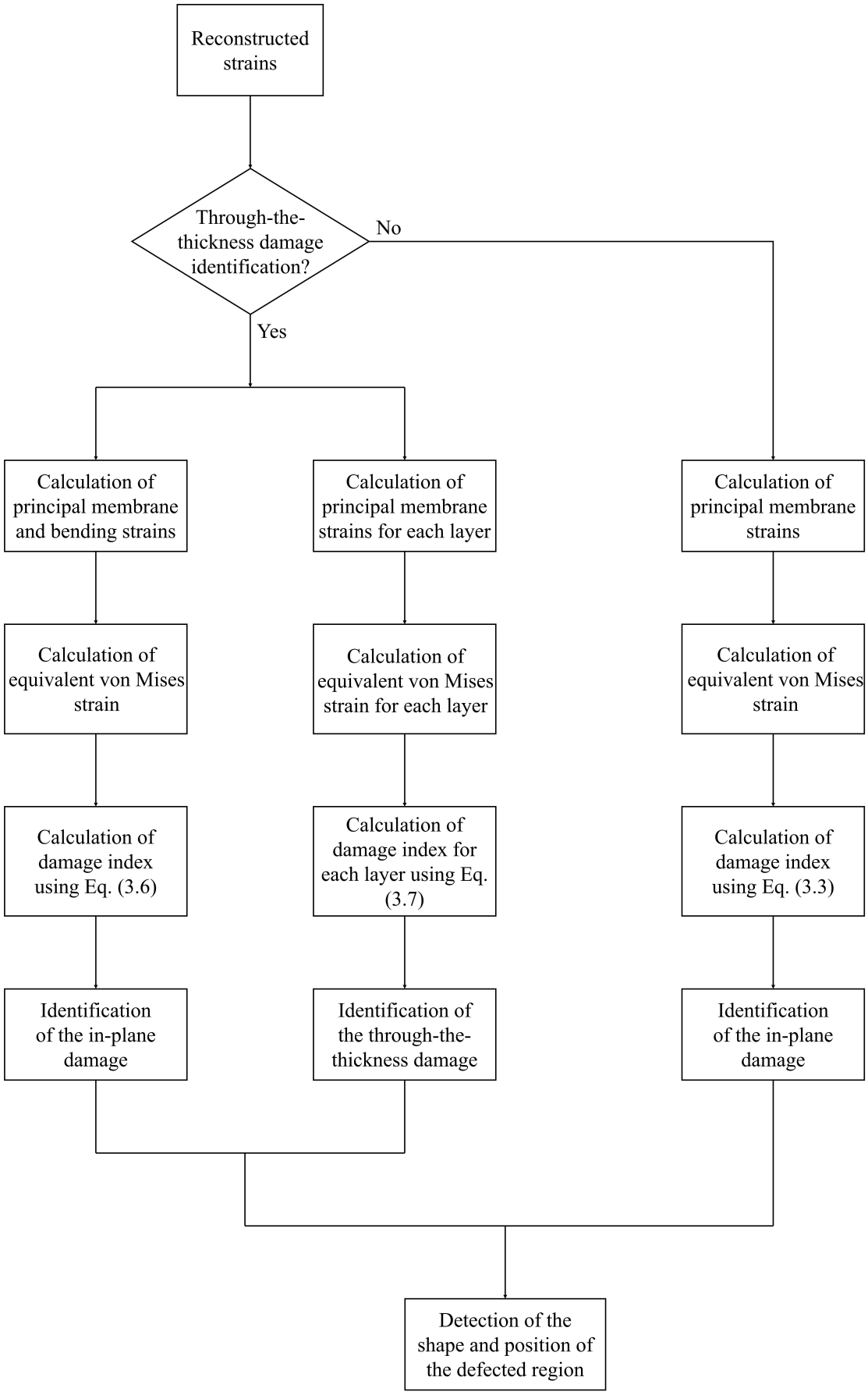

Figure 3.1 The flowchart illustrating the damage detection process.

4. NUMERICAL EXAMPLES

The inverse elements, for which the formulation was provided in the previous section, are implemented in case studies presented herein. These case studies include different problems, and in the problem domain for each case, one or multiple pre-defined defected regions exist. These problems include a plate with damage, a composite shell with damage, transverse bending of a T-beam with damage, a cross-ply composite plate with torsional load, and a curved composite panel subjected to axial loading. The in-situ strain measurements are acquired numerically via running high fidelity forward analysis. In order to better assess the capability of the iFEM method, damage sensitivity plots have been provided, which show the variation of the maximum damage index as the stiffness degradation factor acquires different values.

4.1 Tensile Loading of a Plate

In this case study, a rectangular plate is subjected to tensile loading. In the center of the plate, a circular defected region exists. The plate has a width of 0.01 m, a length of 0.03 m, and a thickness of 0.0001 m. As mentioned, the center of the plate is damaged, and the defected region has a radius of 0.001 m. The geometry of the plate yields a span-to-thickness ratio of $\frac{0.03}{0.0001} = 300$, characterizing this geometry as a thin plate. Additionally, the plate is isotropic, with its Young's modulus equal to 200 GPa, and its Poisson's ratio equal to 0.3. Two ends of the plate, along the vertical direction, are subjected to 120 N/mm of force. In Figure 4.1, the geometry of the plate, loading conditions, and boundary conditions are depicted.

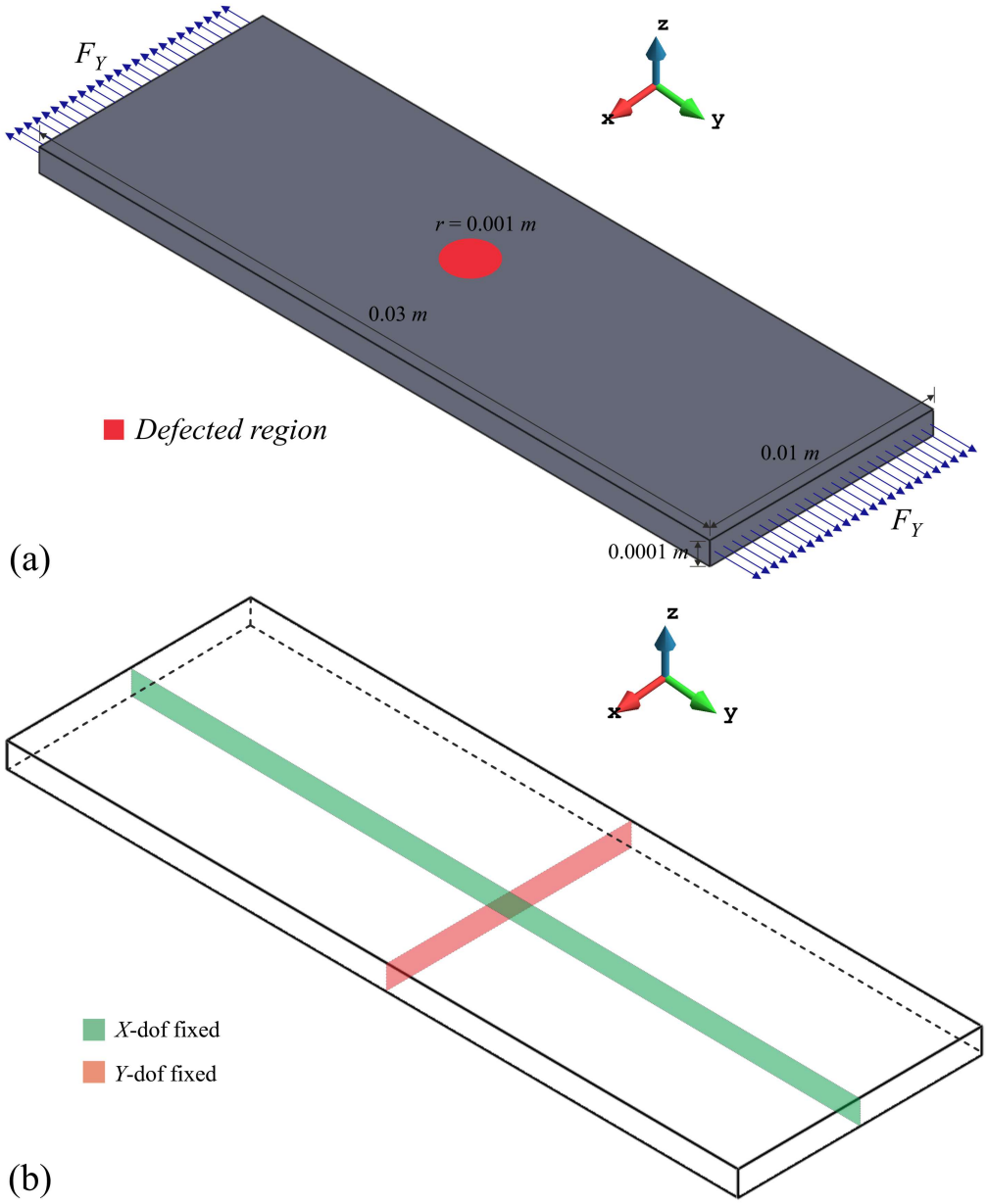

Figure 4.1 (a) Geometry and loading conditions for the plate; (b) Boundary conditions.

For nodes along the green line, degrees of freedom along the X-axis are fixed, whereas, for the nodes along the red line, degrees of freedom are constrained along the Y-axis. Furthermore, the in-situ strain measurements are provided numerically using high fidelity forward analysis. The FE model used for this purpose consists of 1296 elements (Figure 4.2). As it is evident in this figure, a detailed, fine mesh is generated for the FEM analysis. This mesh also takes into account the circular pre-defined damaged region. On the other hand, for the inverse analysis, the mesh is considerably coarser, with a structured grid. In this context, the number of inverse-plane elements for this case study is 48 elements. The data collection scheme is

devised through building 3×3 blocks of elements (Figure 4.3) in the forward model and then using the strain data from the center element of these blocks for the inverse analysis.

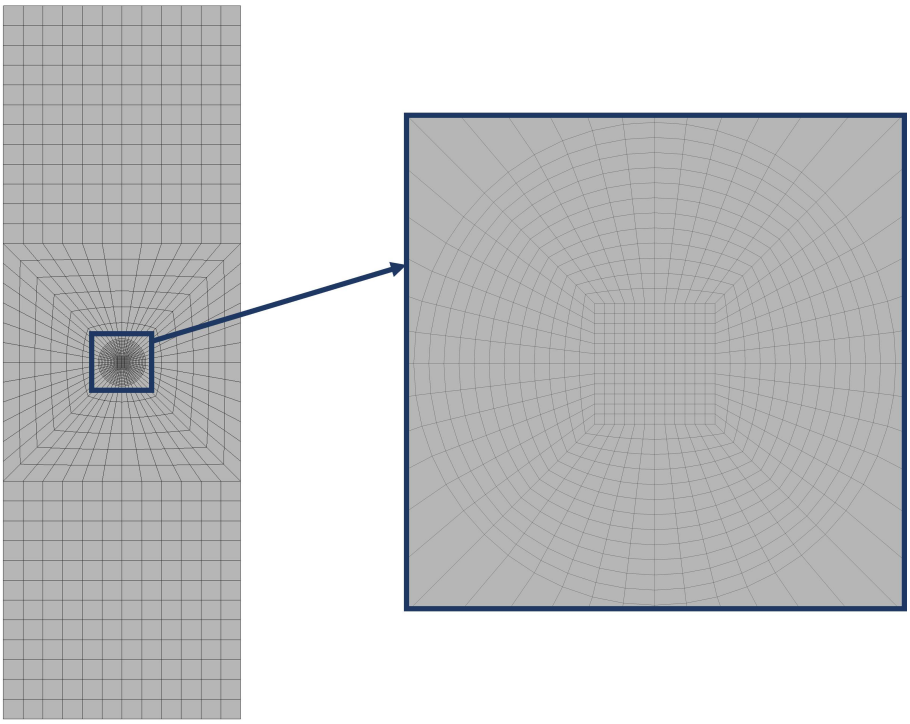

Figure 4.2 Discretization of the problem domain with 1296 elements for conducting the forward analysis.

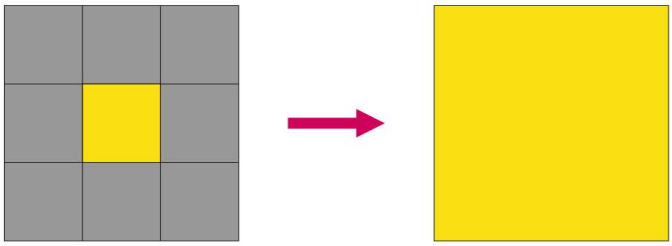

Figure 4.3 Data collection scheme from the forward analysis to the inverse analysis (color yellow denotes the presence of sensor data).

Herein, two distinct sensor placement models have been implemented. These models are namely dense (D), and sparse (S) sensor distribution models. For the dense model, strain data are provided for all the inverse elements, while for the sparse model only a number of the elements are equipped with the in-situ strain measurements. Figure 4.4 shows the iFEM mesh, as well as the sensor deployment models for the inverse analysis.

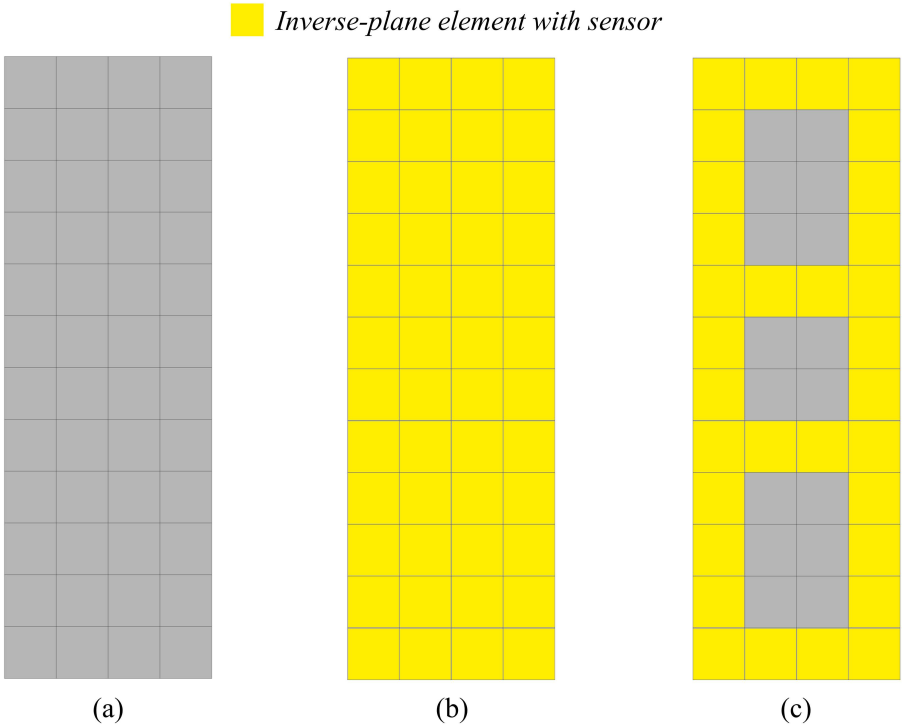

Figure 4.4 (a) Discretization of the problem domain with 48 inverse-plane elements in order to conduct inverse analysis; (b) Dense, D, sensor placement model; (c) Sparse, S, sensor placement model.

Through performing the forward analysis, the strain data are collected from the FEM model depicted in Figure 4.2, and as depicted in the schematic plot of Figure 4.3, they are transferred to the iFEM algorithm. Then, based on the sensor placement models depicted in Figure 4.4, they are utilized to perform the inverse simulations with the aim of detecting the location and the shape of the damaged region on the plate. Here, the results of the forward analysis are used as reference values, and the displacement values calculated using the inverse analysis are compared with the reference solution. Moreover, when using the sparse model, the weighting coefficient α, for inverse-plane elements with no sensor data is set as $\alpha = 10^{-3}$. For the displacements along the X-axis, the results are illustrated in Figure 4.5. The results of iFEM analysis are also depicted in Figures 4.5(b-c). As it is evident, the inverse algorithm has been able to show the variation of the displacement field in the vicinity of the damaged region. Through comparison of the maximum values presented in the U contours, for FEM and iFEM solutions, the percent errors are calculated as 7.83%, and 11.85% for the dense model and the sparse model, respectively. However, the vertical component of the displacement field is reconstructed more accurately in comparison to the horizontal component. The percent errors are given as 1.91% for the dense model, and 0.53% for the sparse model (Figure 4.6). Counter-intuitively, it is seen that the sparse model has a better performance than the dense model in

this case.

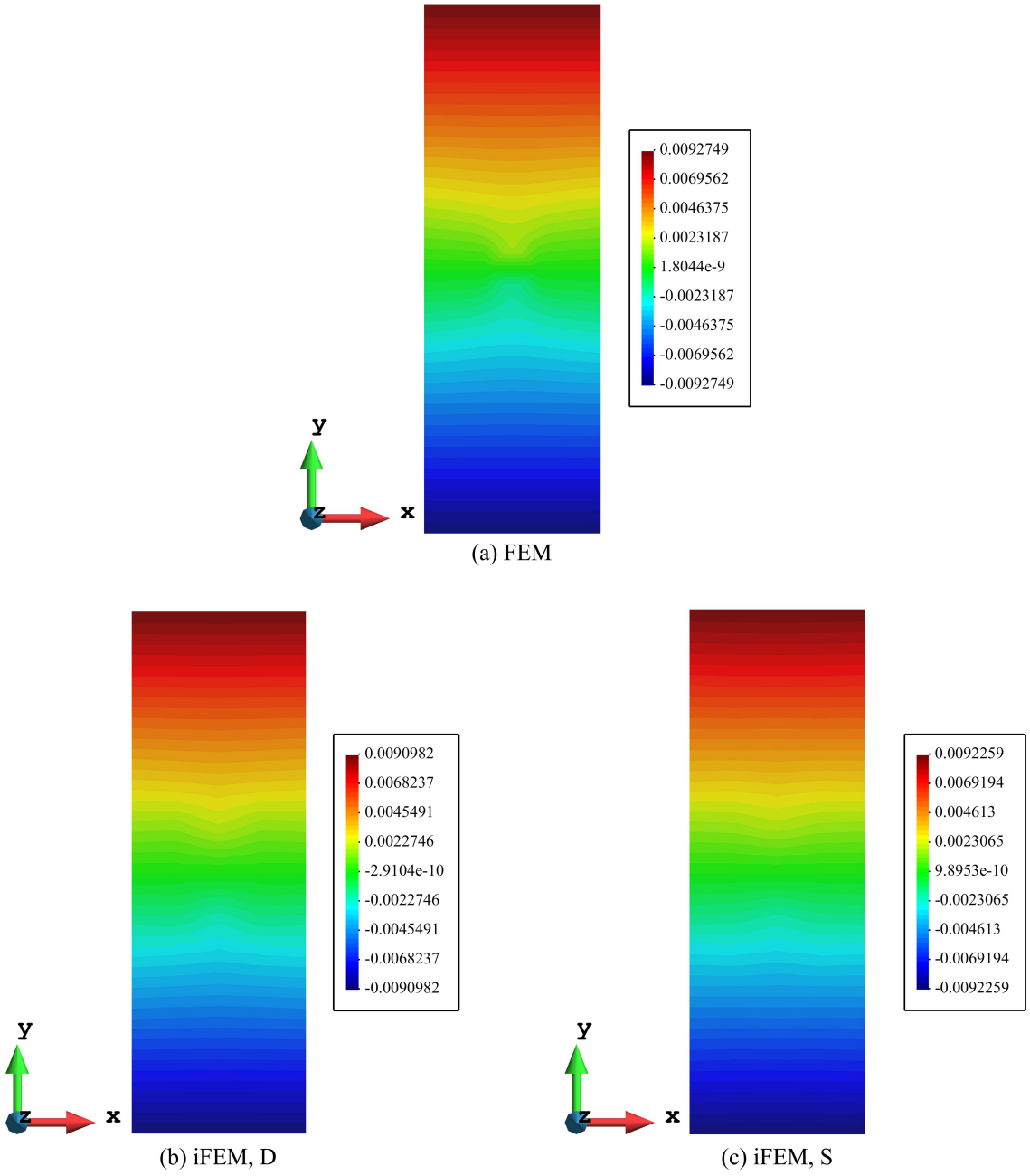

Figure 4.6 Displacement V contours: (a) Forward FEM analysis; (b) iFEM analysis using dense sensor distribution; (c) iFEM analysis using sparse sensor distribution.

In continuation, the contour plots for the von Mises strain are presented in Figure 4.7. The contours in these Figures show that a region of high von Mises strain gradient has been identified using either the dense sensor placement model or the sparse model. This indicates that the plate, at this hot spot is experiencing structural damage.

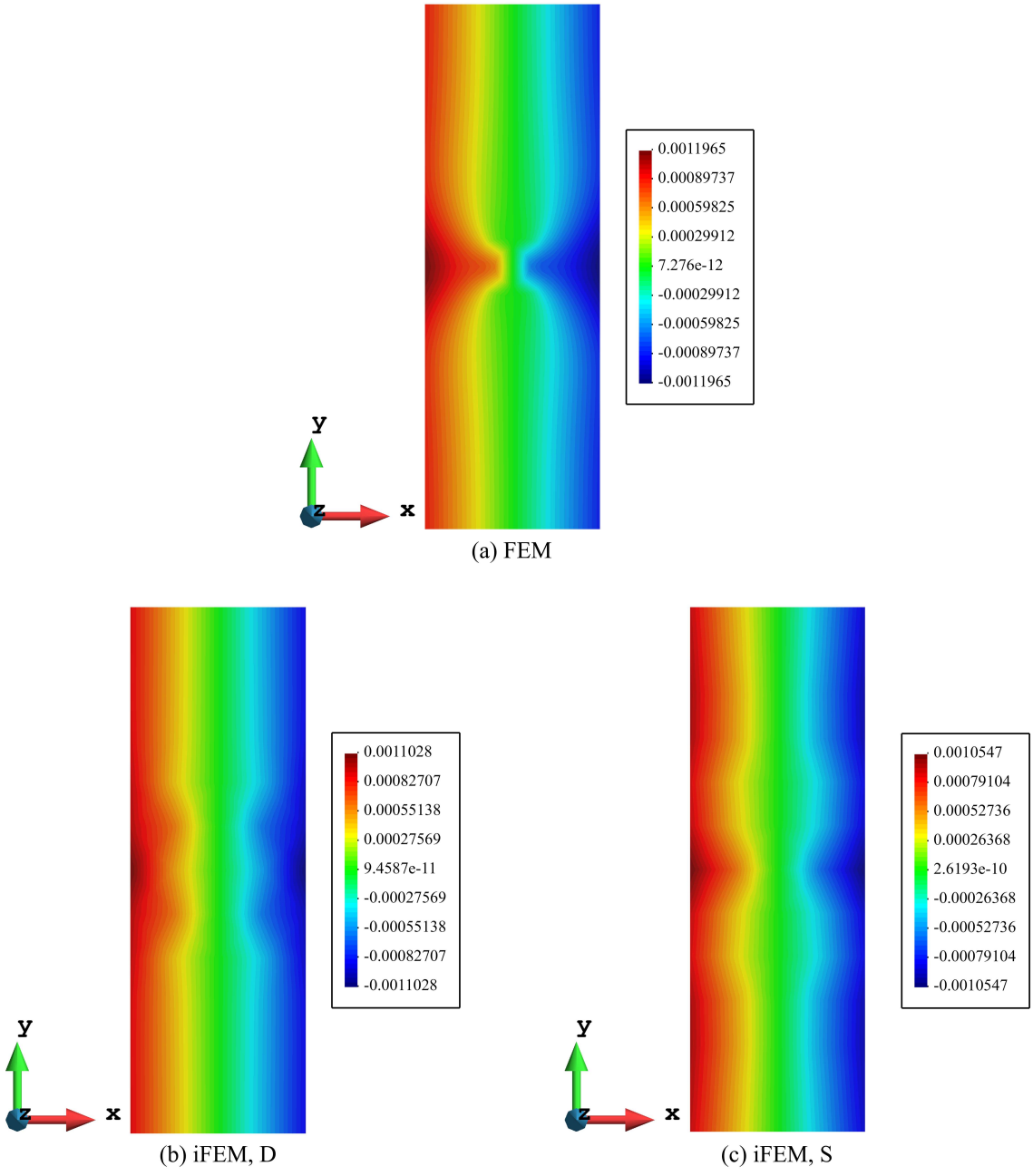

Figure 4.5 Displacement U contours: (a) Forward FEM analysis; (b) iFEM analysis using dense sensor distribution; (c) iFEM analysis using sparse sensor distribution.

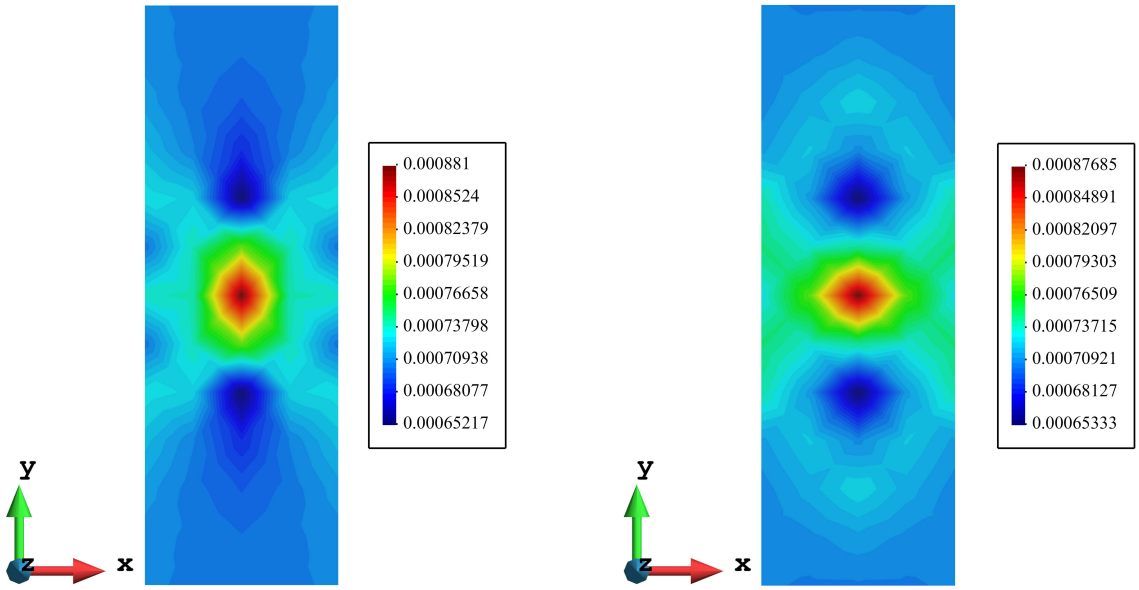

(a) iFEM, D (b) iFEM, S

Figure 4.7 Equivalent strain ε_{VM} contours: (a) iFEM analysis using dense sensor distribution; (b) iFEM analysis using sparse sensor distribution.

Hence, the relation for calculating the damage index provided in Eq. (3.3) is used. As shown in Figure 4.8, the damage has been successfully detected and quantified using both sensor deployment models as a circular region at the center of the plate.

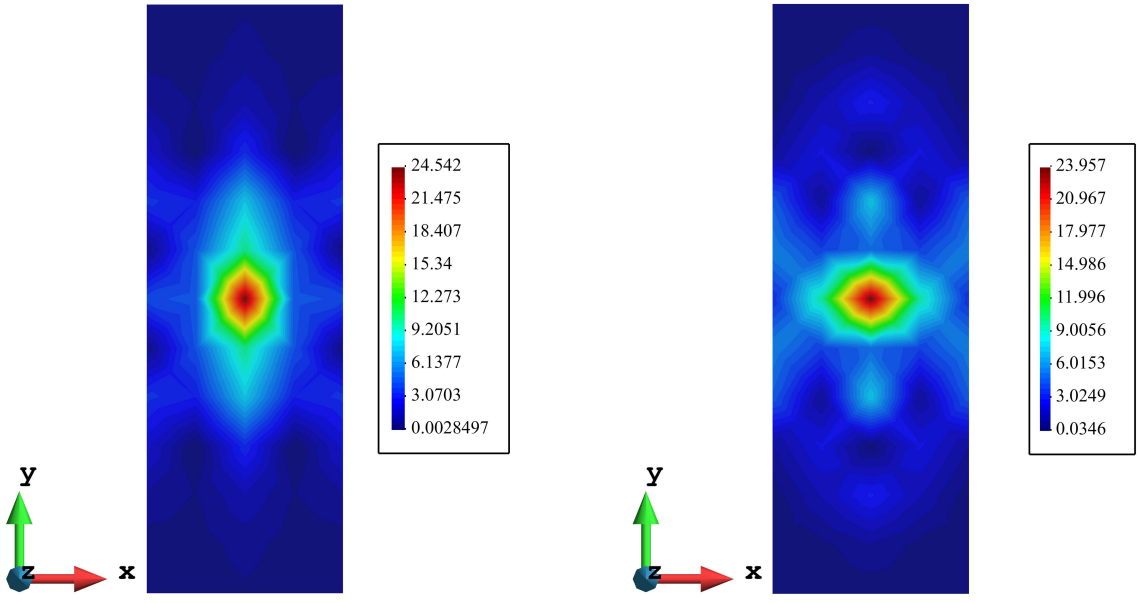

(a) iFEM, D (b) iFEM, S

Figure 4.8 Damage index $DI(\varepsilon_{VM})$ contours: (a) iFEM analysis using dense sensor distribution; (b) iFEM analysis using sparse sensor distribution.

It can be noted that both models have captured the location of the damage and have delivered a rough approximation of the shape of the damage, too. Figure

4.8(a), depicts more conservative results for damage index, with its maximum value computed 24.542%, while for the sparse model, Figure 4.6(b), the maximum damage index is calculated as 23.957%. Nonetheless, the difference between these values is negligible, indicating that the sparse model can confidently be implemented instead of the dense model, which is an important remark, considering that by using this model, less instrumentation equipment is used, hence it is more economical.

In addition to the results of this subsection, damage sensitivity plots have also been demonstrated, plotting the maximum damage index obtained for various stiffness degradation coefficients, λ , prove to be useful tools in order to evaluate the damage detection capabilities of the inverse algorithm. For both models, the graphs in Figure 4.9 follow the same trend. It is seen that as the degradation factor approaches one, the maximum damage index calculated utilizing the equivalent strain becomes lower. According to the results presented in this subsection, it can be concluded that the application of inverse-plane element for two-dimensional problems, with the aim of studying and detecting damage guarantees reliable results. The use of this element can be further extended to experimental applications, where the requisite input strain measurements are provided via strain gauges, and/or FBG sensors.

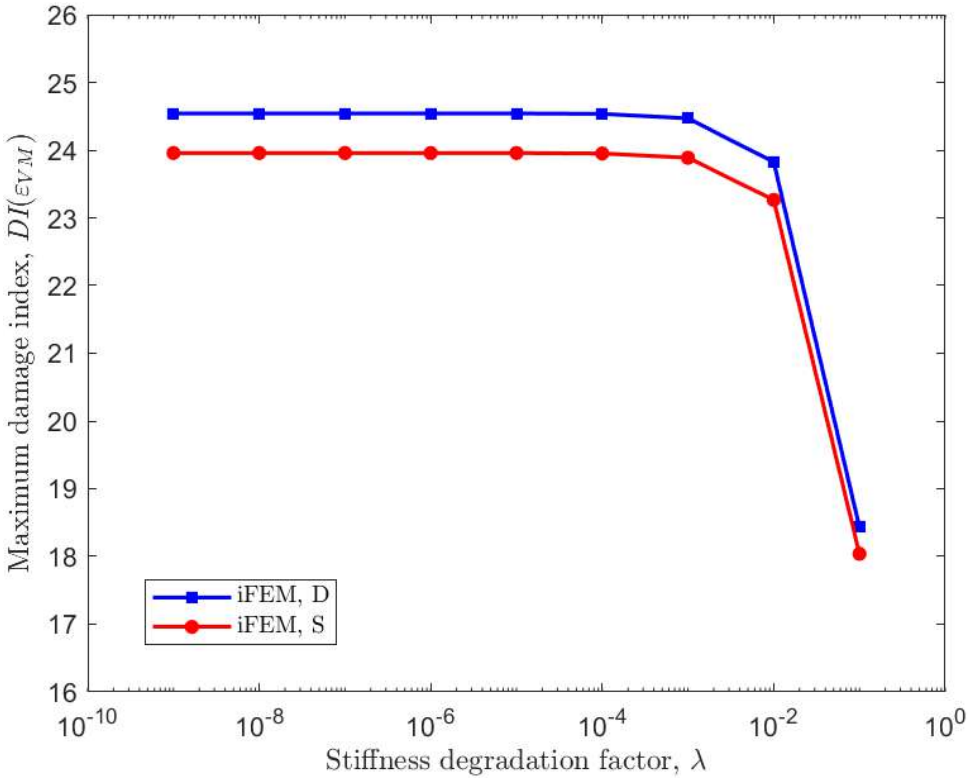

Figure 4.9 Damage sensitivity for plate with pre-defined damage.

4.2 Transverse Bending of a Laminated Composite Shell

Laminated composite materials are prone to various damage mechanisms, which makes their health monitoring a crucial topic for study. To this end, for a composite laminate with a stacking sequence of $[90, 0, -90, 0]_s$, a distributed transverse bending load with a magnitude of 1 kN is applied to its free edge. The shell has a width of 0.08 m and a length of 0.24 m, with the thickness of the laminate being 0.0024 m, indicating that $2h = 0.0024$ m (the thickness of each lamina being 0.0003 m), hence the span-to-thickness ratio is $\frac{0.24}{0.0024} = 100$ and it is seen that this case study, similar to the previous one, is a thin shell problem. Moreover, two damaged areas are present over the problem domain, which are similar to each other, both in terms of their geometries, and stiffness degradation. Additionally, it is assumed that in the damaged region, all of the plies in the laminate are weakened by the same degradation factor, λ. Furthermore, the orthotropic material properties for a single lamina are listed in Table 4.1, and are chosen with reference to Tabrizi et al. (2019).

Unidirectional Carbon-Epoxy Composite		
Young's Modulus [GPa]	Poisson's Ratio	Shear Modulus [GPa]
$E_1 = 133.9$	$\nu_{12} = \nu_{13} = 0.32$	$G_{12} = G_{13} = 4.8$
$E_2 = E_3 = 11.5$	$\nu_{23} = 0.37$	$G_{23} = 4.2$

Table 4.1 Material properties of a single ply: Transverse bending of a laminated composite shell.

The geometry and boundary conditions associated with the composite shell are depicted in Figure 4.10. As illustrated, the left edge of the composite laminate is clamped. The two shaded areas represent the damaged region. The centroids of these damaged regions are at 0.06 m and 0.18 m from the clamped edge, respectively.

The required in-situ strain values are provided through performing high fidelity forward analysis. The forward FEM analysis is conducted utilizing the commercial finite element software, ANSYS-APDL. Then, after acquiring strain data from the model, they are transferred to in-house iFEM code, which is developed within the mathematical framework of iQS4 inverse-shell element. For the inverse analysis, two different sensor placement schemes have been devised. These sensor placement models consist of one dense model (denoted by D), and one sparse model (denoted by S) (Figure 4.11). Herein, Figure 4.11(b), shows the dense distribution of strain measurement devices over the laminate. In this model, all of the inverse elements are

equipped with sensor data in their respective top and bottom surfaces. On the other hand, Figure 4.11(c), shows the sparse sensor placement scheme, and as depicted, only a select set of inverse-shell elements possess sensor data.

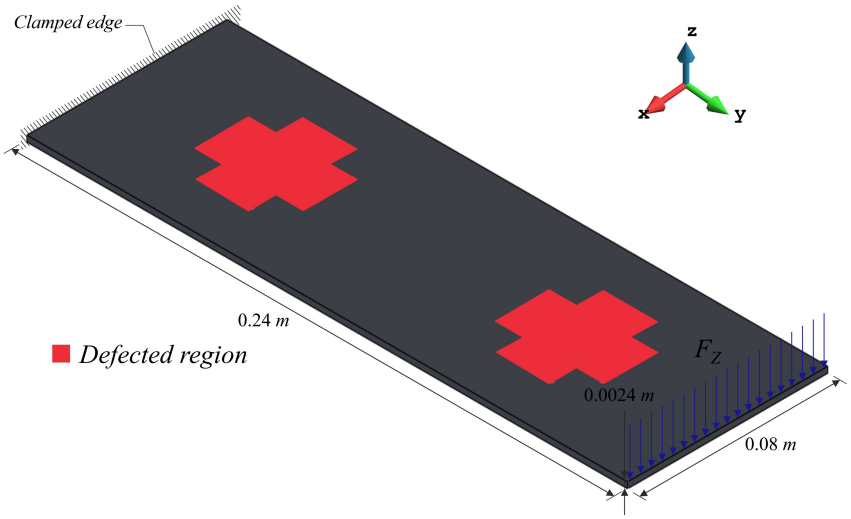

Figure 4.10 The geometry, boundary conditions, and loading conditions of the laminated composite shell.

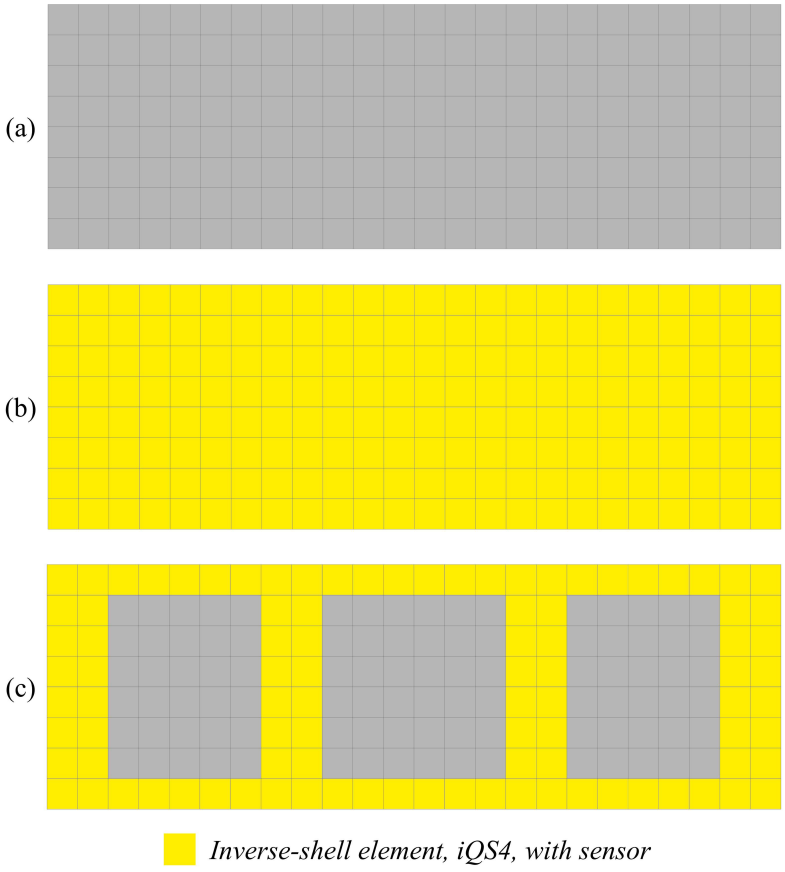

Figure 4.11 (a) Discretization of the laminated composite shell with 192 inverse-shell elements in order to perform inverse analysis; (b) Dense, D, sensor placement model; (c) Sparse, S, sensor placement model.

As it was discussed in the previous section, for the inverse-shell element, after the strain data are collected from both bounding surfaces of the shell, i.e., top and bottom surfaces, via strain gauges and/or FBG sensors, or numerically through running high fidelity forward FEM simulations, Eq. (2.16) is used to process these data and feed them as an input to the inverse algorithm. For inverse-shell elements with sensors mounted on or embedded within them, the weighting coefficients in Eq. (2.17) are set as $w_e = w_k = w_g = 1$, whereas for inverse elements with no input strain information, $w_e = w_k = w_g = \alpha = 10^{-5}$. In this problem, the results obtained from the FEM simulation are set as a reference for the results of the inverse approach. Next, through implementation of dense and sparse models (Figures 4.11(b-c)) in the iFEM algorithm, results for W, θ_X, and θ_Y are obtained and compared to the reference solution, as for other degrees of freedom the displacement and rotation components are equal to zero.

The results for W are illustrated in Figure 4.12. It is evident that iFEM has reconstructed the displacement field in an accurate manner (Figures 4.12(b-c)). The percent error calculated using the maximum displacements shown in Figure 4.12 yields 0.06% for the dense model and 0.37% when the sparse model is implemented. Besides, the rotations about the X- and Y-axes have also been calculated, and their contour plots are displayed in Figures 4.13-4.14. For rotations about the X-axis, θ_X, the percent error is calculated by utilizing the maximum values of the rotation, and in this regard, for the dense model 9.11% error is calculated, whereas, for the sparse model, the percent error is 2.37%. On the other hand, the reconstruction of the rotations about the Y-axis, θ_Y, using iFEM yields better results. It is seen that the dense model has an error of 0.006%, whereas the sparse model has a percent error of 0.096%. In this case study, iFEM proves to be a positively powerful means of SHM, as it provides results that are extremely close to the reference solution.

(a) FEM

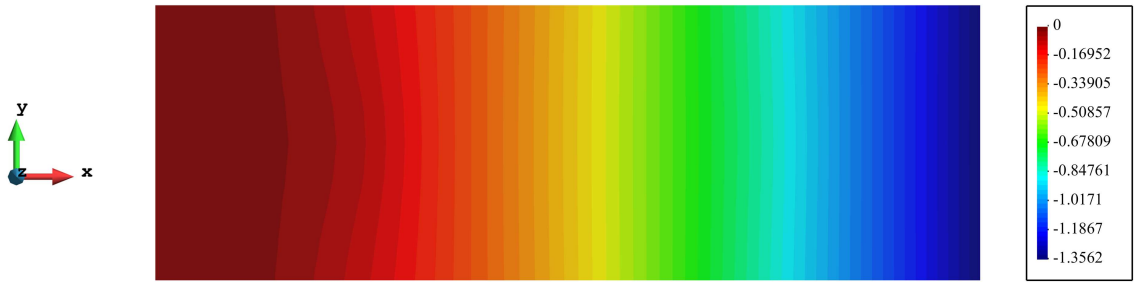

(b) iFEM, D

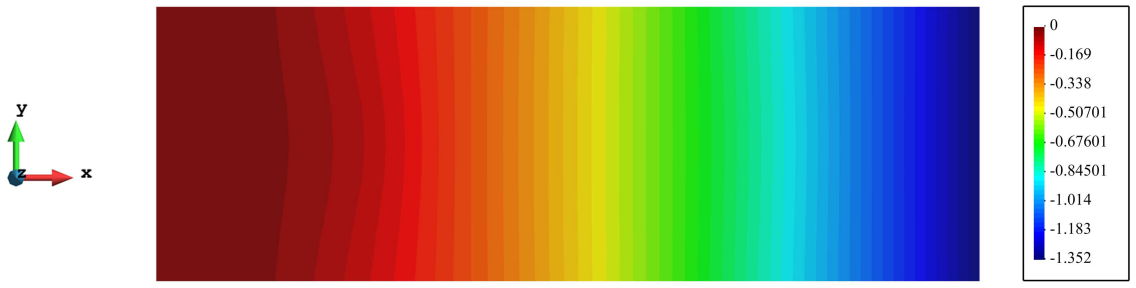

(c) iFEM, S

Figure 4.12 Displacement W contours: (a) Forward FEM analysis; (b) iFEM analysis using dense sensor distribution; (c) iFEM analysis using sparse sensor distribution.

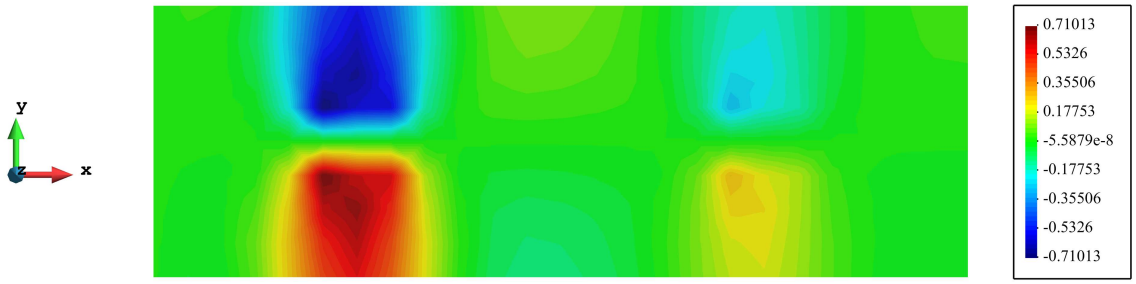

(a) FEM

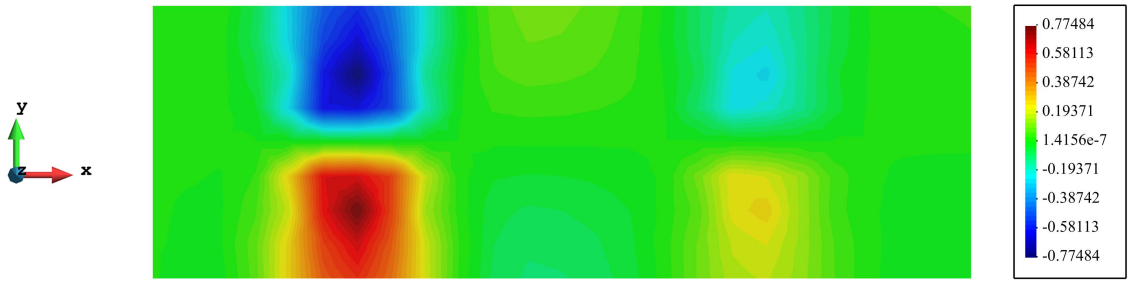

(b) iFEM, D

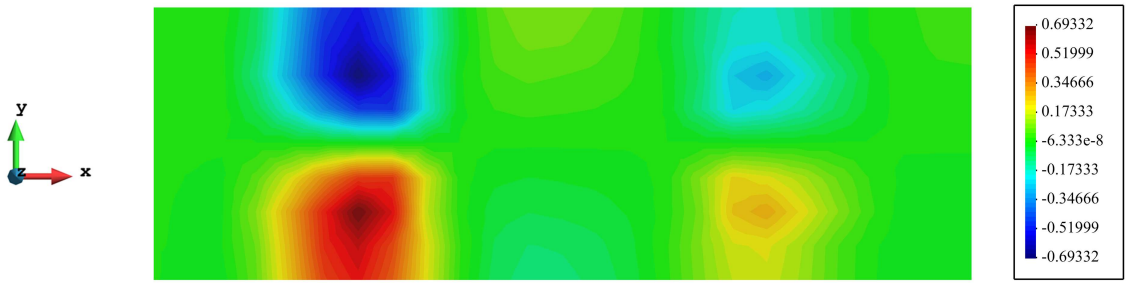

(c) iFEM, S

Figure 4.13 Rotation θ_X contours: (a) Forward FEM analysis; (b) iFEM analysis using dense sensor distribution; (c) iFEM analysis using sparse sensor distribution.

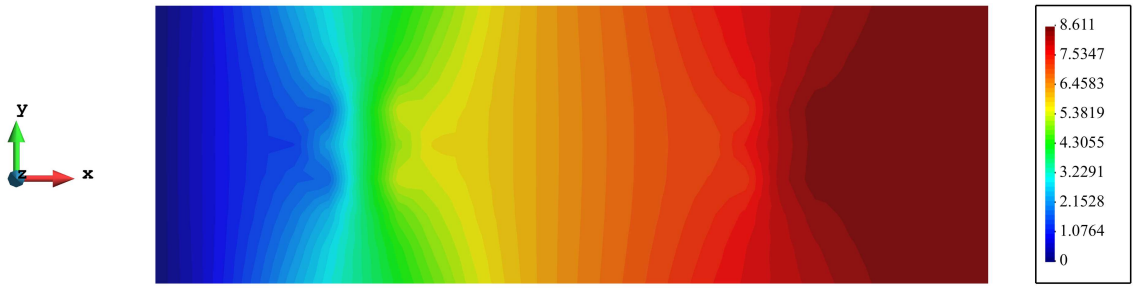

(a) FEM

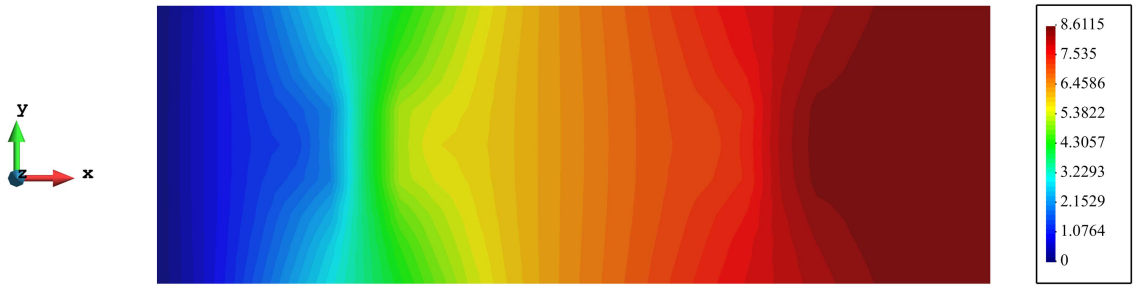

(b) iFEM, D

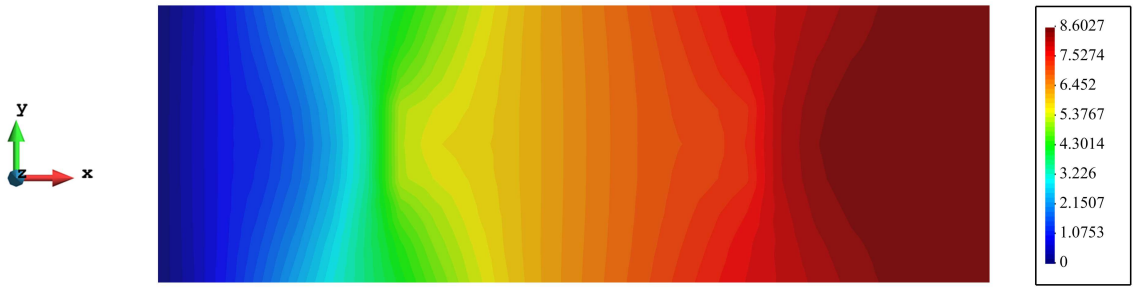

(c) iFEM, S

Figure 4.14 Rotation θ_Y contours: (a) Forward FEM analysis; (b) iFEM analysis using dense sensor distribution; (c) iFEM analysis using sparse sensor distribution.

Moreover, in order to conduct the damage detection study, it is of paramount importance to use the equivalent von Mises strain contours and the damage index contours together. As a result, the equivalent von Mises strain can be calculated using Eq. (4.1). Evidently, this equation is different from the definition provided in Eq. (3.4a), and it stems from the fact that, for the inverse-shell element, in conjunction with the membrane strain terms, normal strain component ε_{zz} transverse-shear strain terms, namely γ_{xz} and γ_{yz}, also exist.

$$\varepsilon_{VM} = \frac{1}{3}\sqrt{2\left[(\varepsilon_{xx}-\varepsilon_{yy})^2+(\varepsilon_{yy}-\varepsilon_{zz})^2+(\varepsilon_{zz}-\varepsilon_{xx})^2+\frac{3}{2}(\gamma_{xy}^2+\gamma_{yz}^2+\gamma_{zx}^2)\right]} \quad (4.1)$$

The contour plots for the equivalent von Mises strains are presented below. Evidently, the iFEM has successfully detected the flawed regions. The gradient of the

von Mises strain is proof of the matter. A comparison between the results of both sensor models can also be conducted, and thereby, it is seen that they capture a relatively similar shape for the regions with a high probability of damage and relatively similar ranges for the values of the equivalent strains that are captured via the iFEM (Figure 4.15).

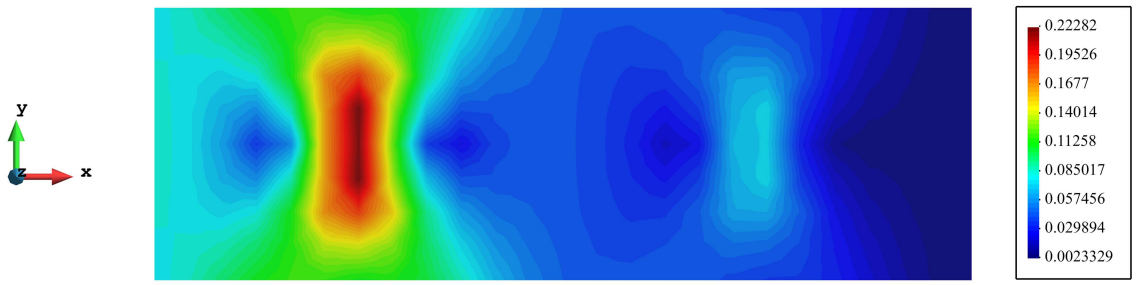

(a) iFEM, D

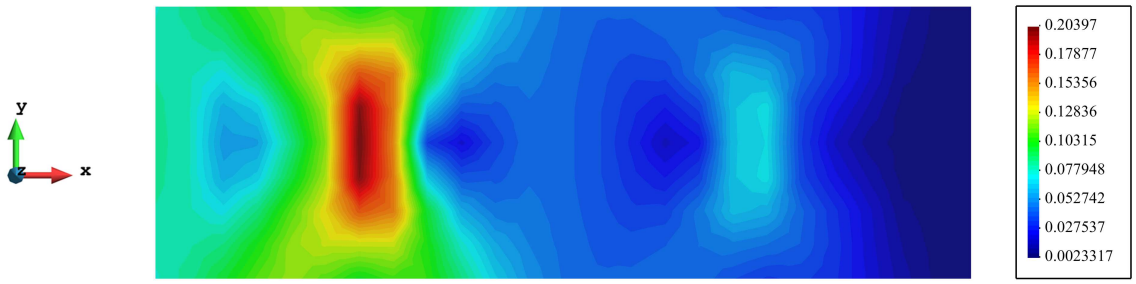

(b) iFEM, S

Figure 4.15 Equivalent strain ε_{VM} contours: (a) iFEM analysis using dense sensor distribution; (b) iFEM analysis using sparse sensor distribution.

Additionally, the damage index for both inverse solutions can be calculated using Eq. (3.3). This, along with the results illustrated in Figure 4.15, will contribute to understanding the state and extent of damage in the laminated composite shell. The damage index contours, as depicted in Figure 4.16, show that for both of the damaged areas, the intensity of the damage is similar, and almost indistinguishable. Conversely, this is not the visual conclusion to be made by using the plots in Figure 4.15. Thus, in terms of understanding damage, the contour plots in Figures 4.15-4.16 must be studied together.

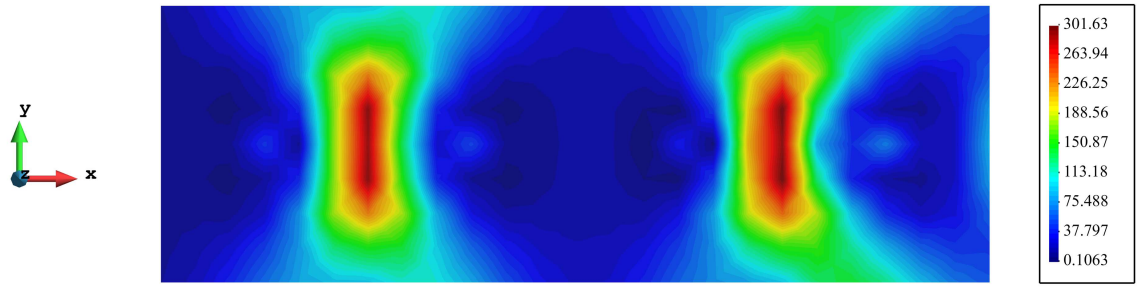

(a) iFEM, D

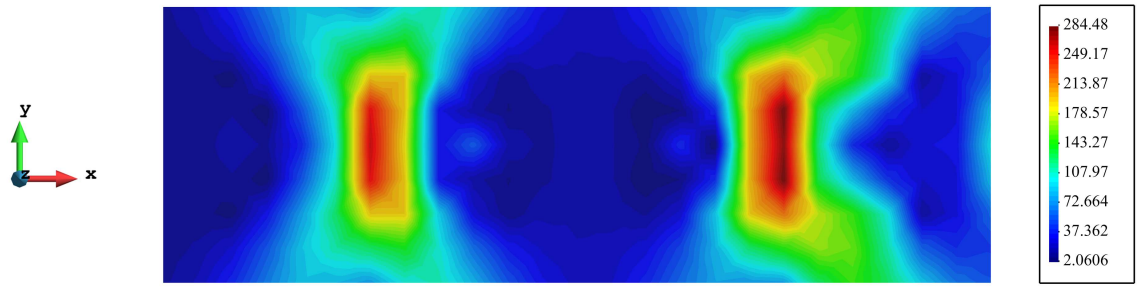

(b) iFEM, S

Figure 4.16 Damage index $DI(\varepsilon_{VM})$ contours: (a) iFEM analysis using dense sensor distribution; (b) iFEM analysis using sparse sensor distribution.

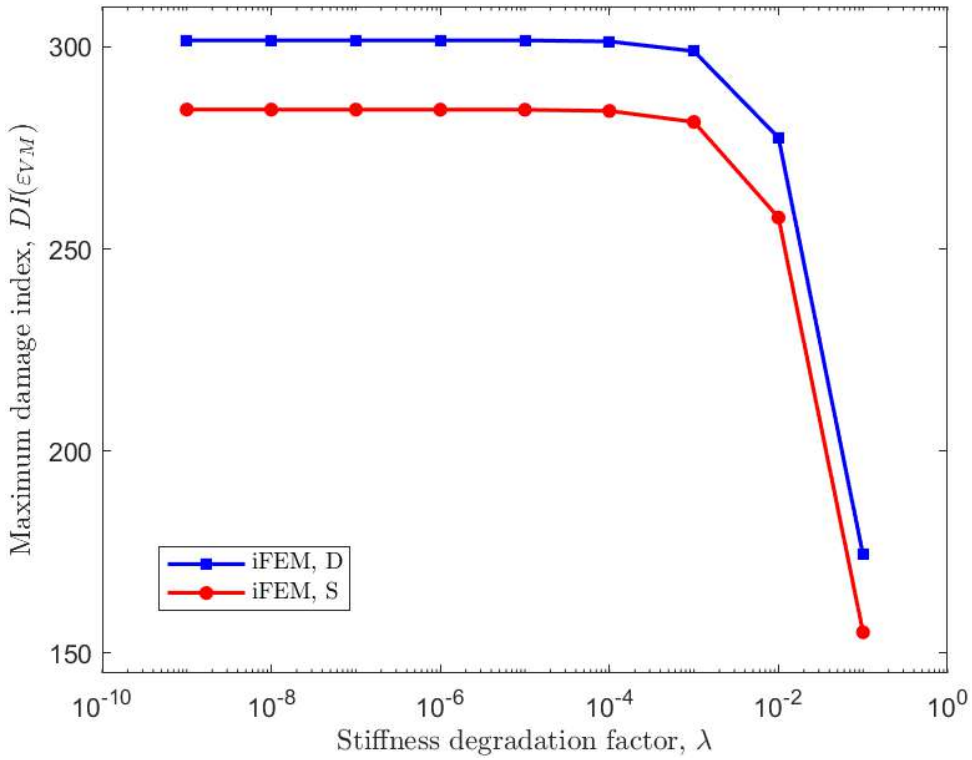

Figure 4.17 Damage sensitivity for laminated composite shell with pre-defined damage.

Furthermore, it is visible that the locations of the defected regions are predicted correctly, while the shape of the damage is roughly estimated as a rectangular area. To this end, the sensitivity of iFEM, when using iQS4 element can also be assessed. As a consequence, the damage sensitivity plots show that the sensitivity of both sensor placement models to damage decrease at $\lambda = 10^{-5}$. The graphs show that the damage sensitivity follows the same pattern for both models, with the dense model being more conservative than the sparse model, given that for the same strain input, the maximum damage index calculated for dense sensor deployment is more than that of sparse sensor deployment model, similar to the case with the inverse-plane element. Nevertheless, this phenomenon is expected, because in the dense model, strain data are available over the entire problem domain. By the same token, through close examination of the reconstructed displacement field for both the dense and the sparse models, it is concluded that using the sparse model is more preferable as the solution of the iFEM with this model is adequately precise and to implement it, lesser number of sensors is required.

4.3 Transverse Bending of a T-Beam Structure

T-beams are widely used in maritime and aerospace industries. T-beams are structured in way that a haphazard loading can be experienced as either an in-plane or transverse load by its various constituents, i.e., the base plate and stiffeners. In this case study, inverse analysis is performed on a T-beam structure. The geometry of the structure, in conjunction with a cross-sectional view of the T-beam used in this study, can be seen in Figure 4.18. This Figure also shows the boundary conditions applied to the structure. As depicted in the Figure, the structure is clamped in one of its edges, while the other edge undergoes a distributed bending load applied along Z direction. The structure is assumed to have a defected region which includes parts of a stiffener (Figure 4.18). Similar to the previous examples, $\lambda = 10^{-9}$. This study is performed with the aim to capture damage in structures that are more complicated than a simple shell structure. Furthermore, since promising results were achieved by implementing the iQS4 element for the inverse analysis of a shell structure, the T-beam can be modeled as a combination of multiple shells, making it feasible to utilize the mentioned inverse-shell element, iQS4. The structure is assumed to be composed of an isotropic material, with Young's modulus of 210 GPa, and a Poisson's ratio of 0.3.

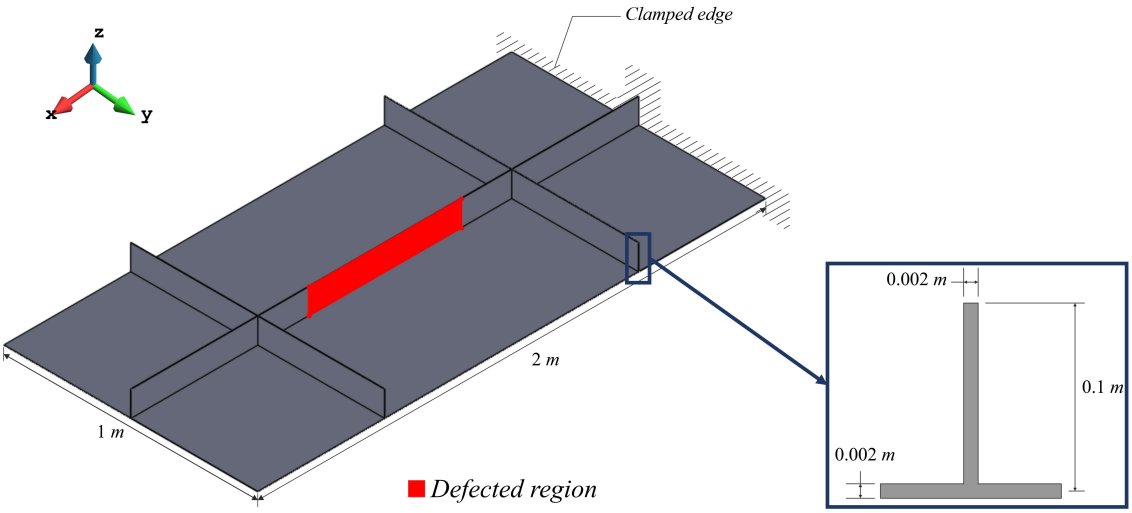

Figure 4.18 The geometry, dimensions, and the boundary conditions of the T-beam structure.

Considering that the performance of the inverse-shell element with various types of sensor placement models was evaluated in the previous case study, for this problem, only one sparse sensor placement scheme is utilized. The iFEM discretization and the sensor placement scheme of the T-beam are illustrated in Figure 4.20. The problem domain is discretized into 240 inverse-shell elements. Moreover, in the inverse analysis, the strain data for the corresponding inverse elements are provided in both the top and bottom surfaces of the element (local coordinate system perspective). The strain data set is acquired via simulations performed in ANSYS-APDL, and then they are processed in the inverse algorithm. The same weighting coefficients for Eq. (2.17), which were used in the previous case study are utilized.

The loading condition for this example problem is defined as a distributed force with a magnitude of 2 kN applied in the negative direction of the Z-axis (Figure 4.19). At the first glance, it might be speculated that this load is going to affect the overall stiffened structured as a bending load does to a plate, however, as discussed earlier, during a load case, different components of the T-beam are subjected to different modes of loading.

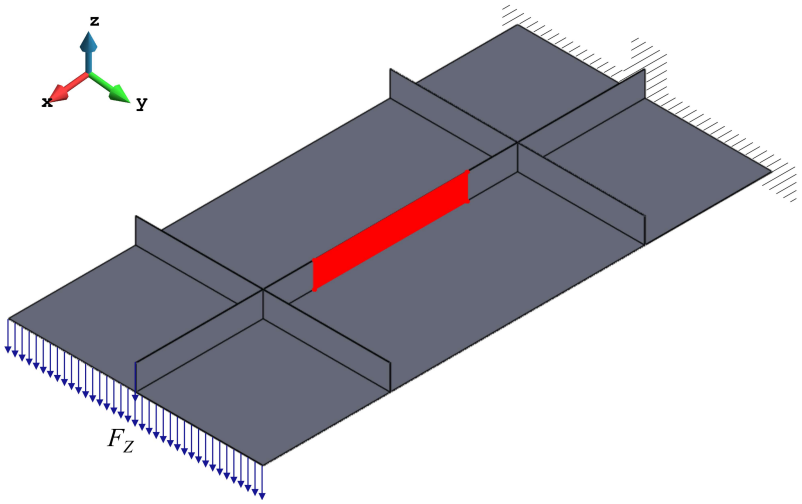

Figure 4.19 Distributed load along Z-axis exerted on the T-beam.

The field variable calculated via iFEM, global displacement vector, consists of components of displacement (translations), U, V, and W, and components of rotation, θ_X, θ_Y, and θ_Z. In order to present the results in a more cohesive and comprehensible manner, the magnitude of the vector sum of the nodal values of the displacement (translation) terms, U_T, and rotation terms, θ_T, have been displayed (Eq. 4.2). In this context, the contour plots of the displacements (translations) and rotations for both the forward analysis and inverse analysis, have been exhibited with an isometric perspective in Figures 4.21-4.22.

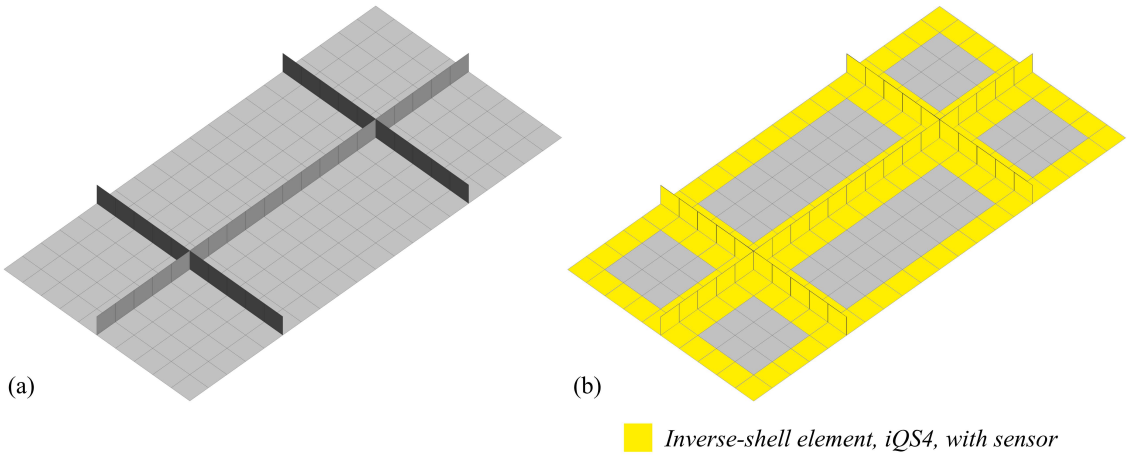

Figure 4.20 (a) Discretization of the T-beam structure with 240 inverse-shell elements in order to perform inverse analysis; (b) Sensor placement model for the inverse analysis.

$$U_T = \sqrt{U^2 + V^2 + W^2} \tag{4.2a}$$

$$\theta_T = \sqrt{\theta_X^2 + \theta_Y^2 + \theta_Z^2} \tag{4.2b}$$

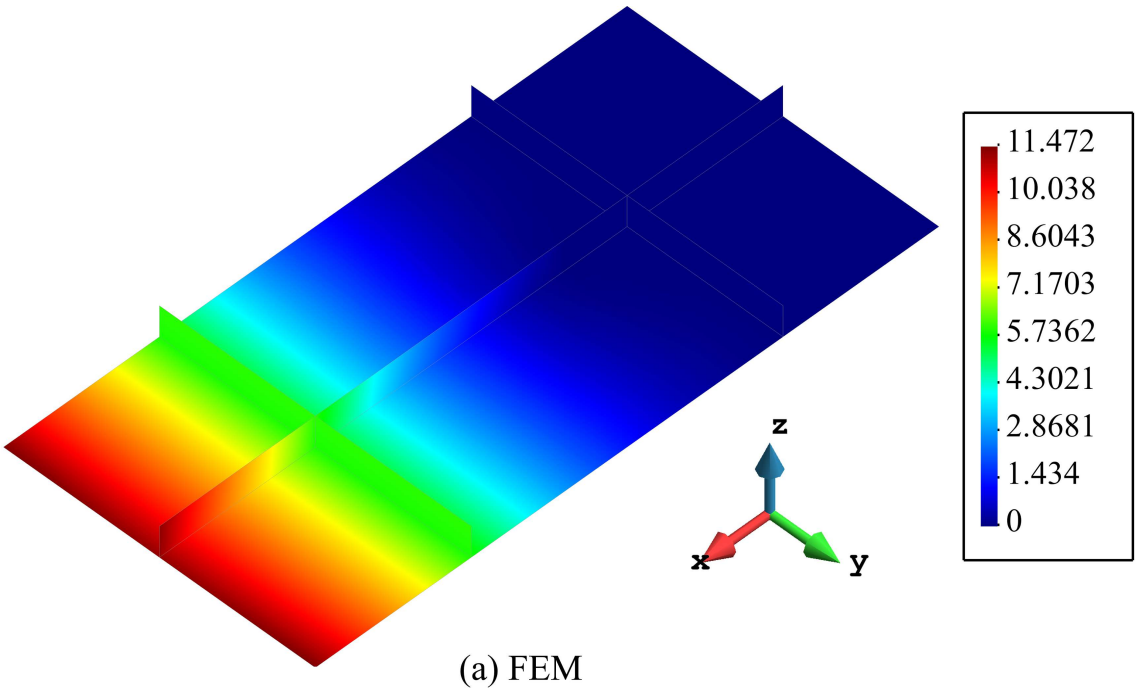

(a) FEM

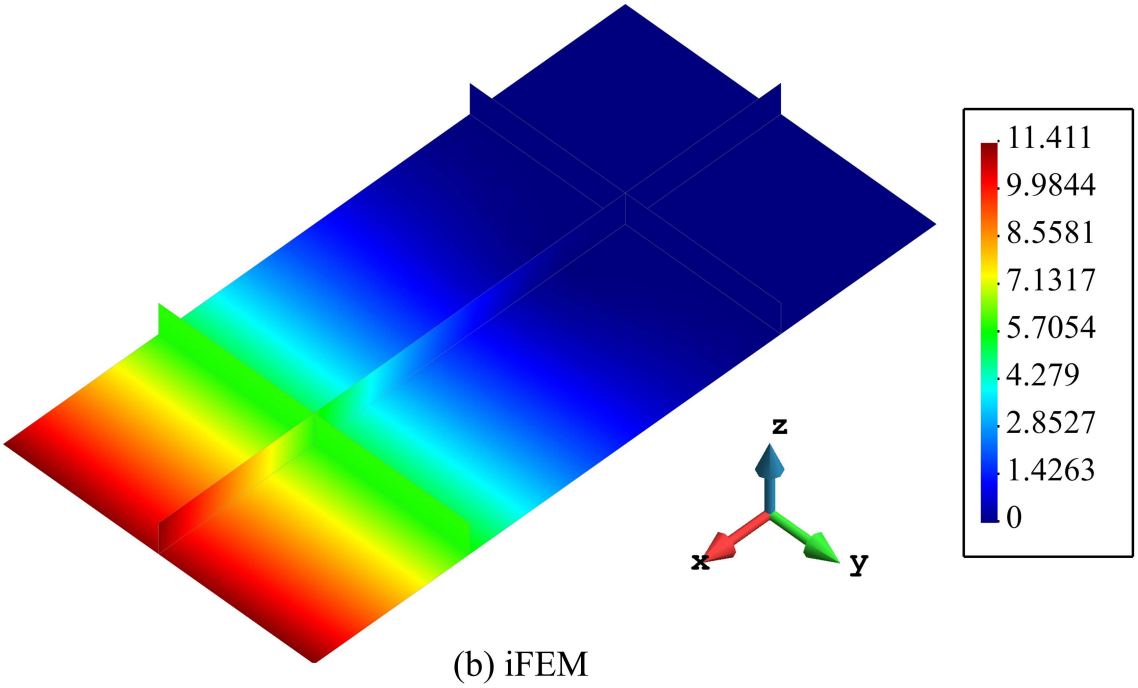

(b) iFEM

Figure 4.21 Total displacement U_T contours for distributed load along Z-axis: (a) FEM solution; (b) iFEM solution.

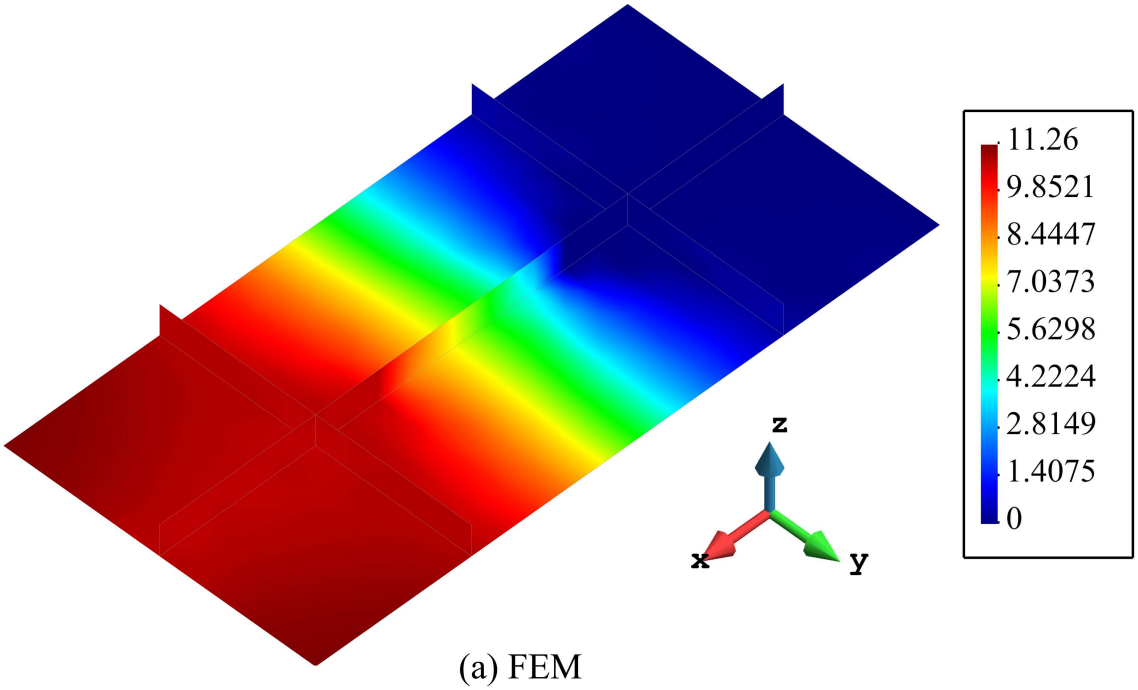

(a) FEM

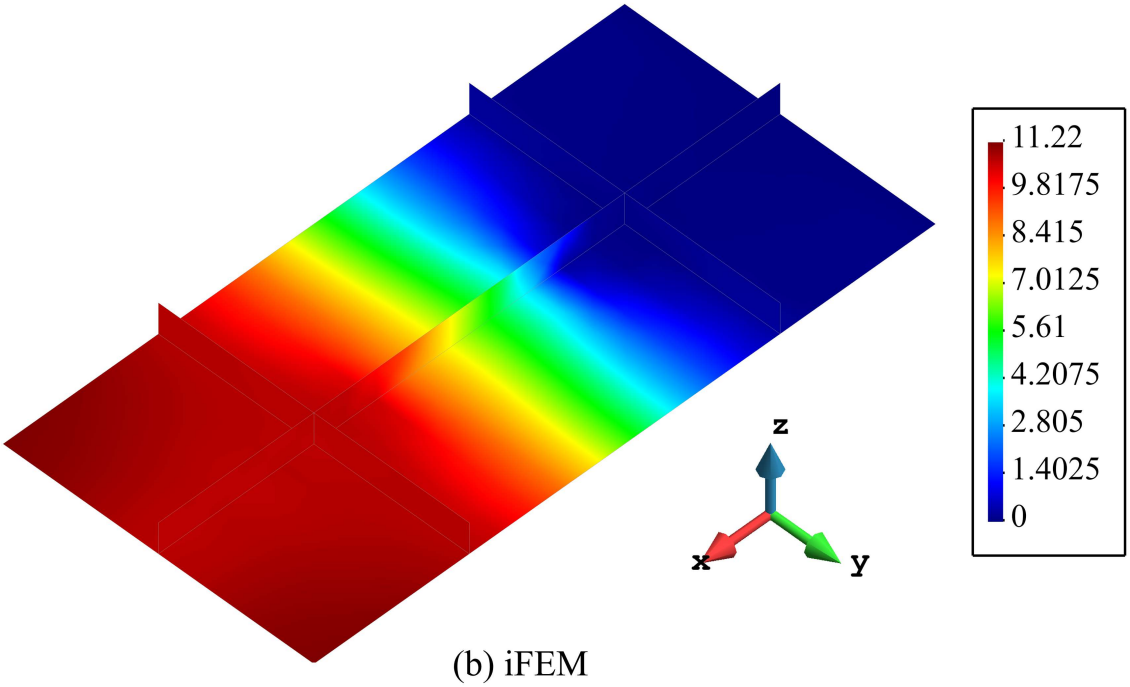

(b) iFEM

Figure 4.22 Total rotation θ_T contours for distributed load along Z-axis: (a) FEM solution; (b) iFEM solution.

The results for the total nodal displacement show a decent agreement between FEM and iFEM. The percent error calculated using the maximum values of total displacement is 0.53%. In addition, the total nodal rotations are also computed and exhibited in Figure 4.22, which shows the percent error for the rotations derived as 0.36%. These percentages indicate that iFEM accurately reconstructs the displacement field. Besides, considering that iFEM-iQS4 is occasionally prone to exhibiting inaccurate results in the cases of in-plane bending (stiffener perspective), these values show successful implementation of this inverse element type which has led to minimization of the functional derived in Eq. (2.17) to produce decent results. Additionally, the displacement field shows traces of discontinuity, which is a sign of damage. Yet, as a more reliable and precise means of detecting damage, the equivalent von Mises strain is calculated using Eq. (4.1), and the corresponding contour plot is visible in Figure 4.23.

The von Mises strain contour shows that over the problem domain, on one of the stiffeners which will be denoted as the horizontal stiffener, strain gradient is formed, demonstrating the existence of defect. In addition, more important and noteworthy results can be observed from the damage index contour (Figure 4.24). The defected areas over the problem domain are revealed in the contour plots by consulting the regions where an equivalent strain hot spot has been generated. In this regard, Figure 4.24 shows a high concentration of damage index at this location with a percentage of 99.949%, indicating that this region is experiencing almost complete structural failure.

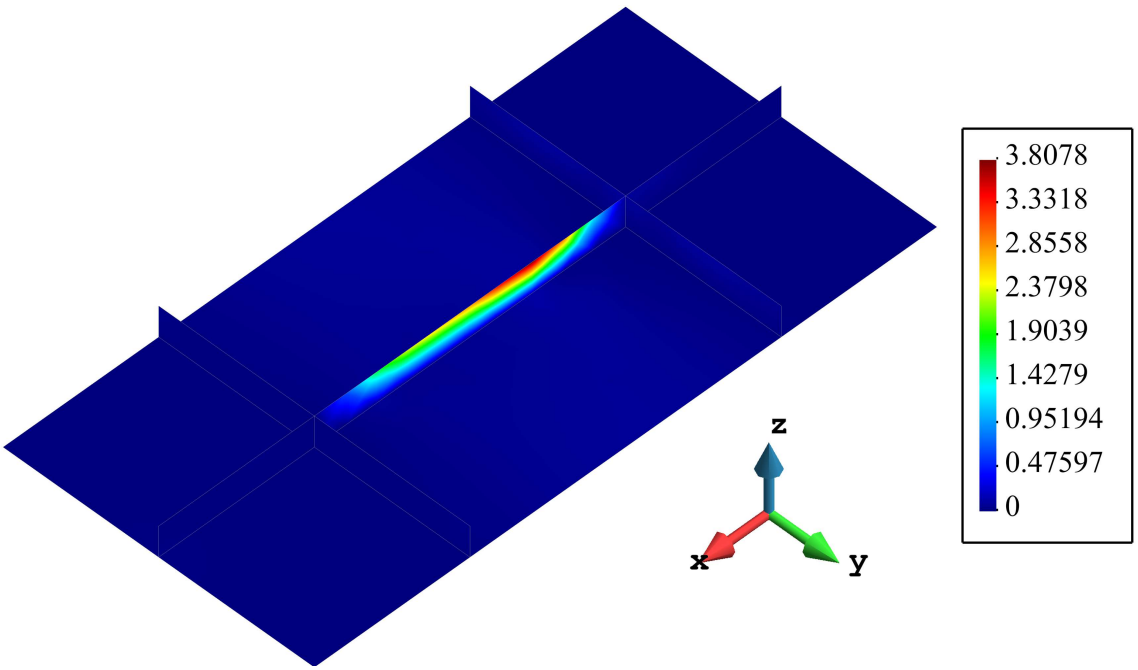

Figure 4.23 Equivalent strain ε_{VM} contours for distributed load along Z-axis, obtained via the iFEM algorithm.

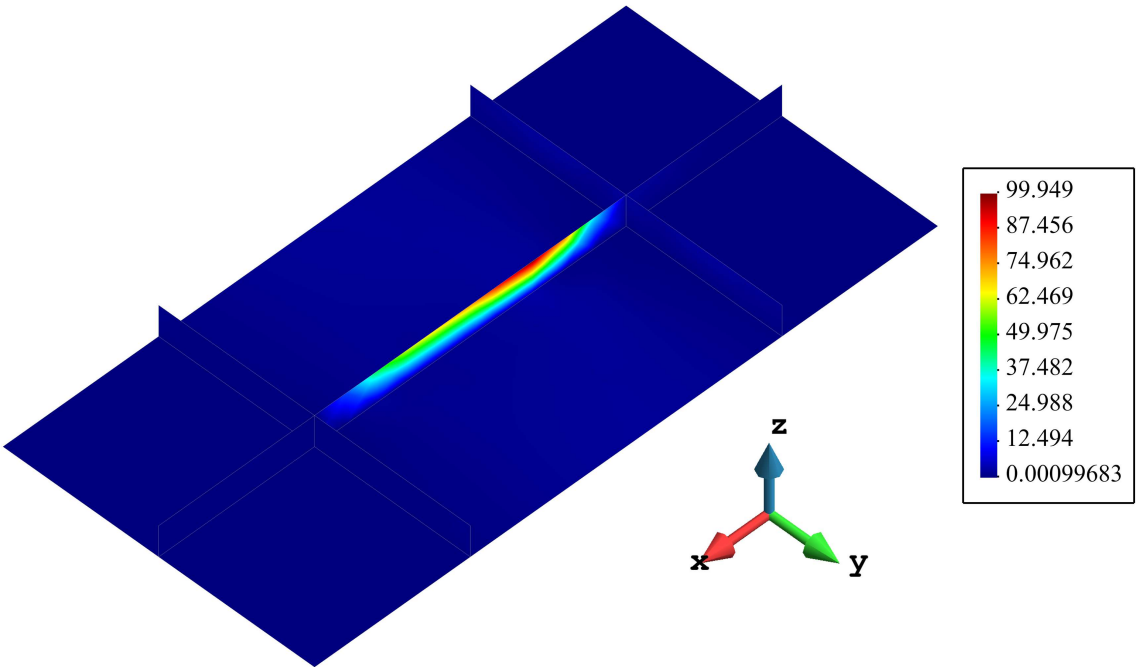

Figure 4.24 Damage index $DI(\varepsilon_{VM})$ contours for distributed load along Z-axis.

4.4 Composite Plate with Torsional Loading

The examples studied earlier show the robustness of the iFEM in its ability to detect in-plane location of the damage successfully, for both simple and relatively complicated structures such as T-beams. However, in the case of laminated structures, through-the-thickness location of damage also gains significance. In the example of the laminated composite shell subjected to bending load, the in-plane location of the flaw was depicted with high precision, however, iFEM did not provide further information which could attest to its capability in determining the position of the defect through the thickness of the laminated shell. To give the iFEM the ability to predict through-the-thickness defects, RZT was incorporated within iFEM (Kefal & Tessler, 2021).

This section of the present study has targeted through-the-thickness damage detection in a cross-ply laminated composite plate. In the mentioned plate, laminae have been oriented according to the stacking sequence $[0, 90, 0, 90, 0]$. The plate is clamped in one end and over its free edge, a torsional distributed force with a magnitude of 90 N/m is applied (Figure 4.25). The 100×400 mm^2 plate has a thickness of 2 mm (0.4 mm/lamina), making it a thin structure (span-to-thickness ratio$= \frac{400}{2} = 200$).

The orthotropic material properties for the plate are presented in Table (4.2). It is assumed that damage is a circular domain in the second layer of the laminated plate, and in the location of the defected region, the material properties are reduced by a factor of 10^{-5}.

Unidirectional Carbon-Epoxy Composite		
Young's Modulus [GPa]	Poisson's Ratio	Shear Modulus [GPa]
$E_1 = 157.9$	$\nu_{12} = \nu_{13} = 0.32$	$G_{12} = G_{13} = 5.93$
$E_2 = E_3 = 9.584$	$\nu_{23} = 0.49$	$G_{23} = 3.227$

Table 4.2 Material properties of a single ply: Composite plate with torsional loading.

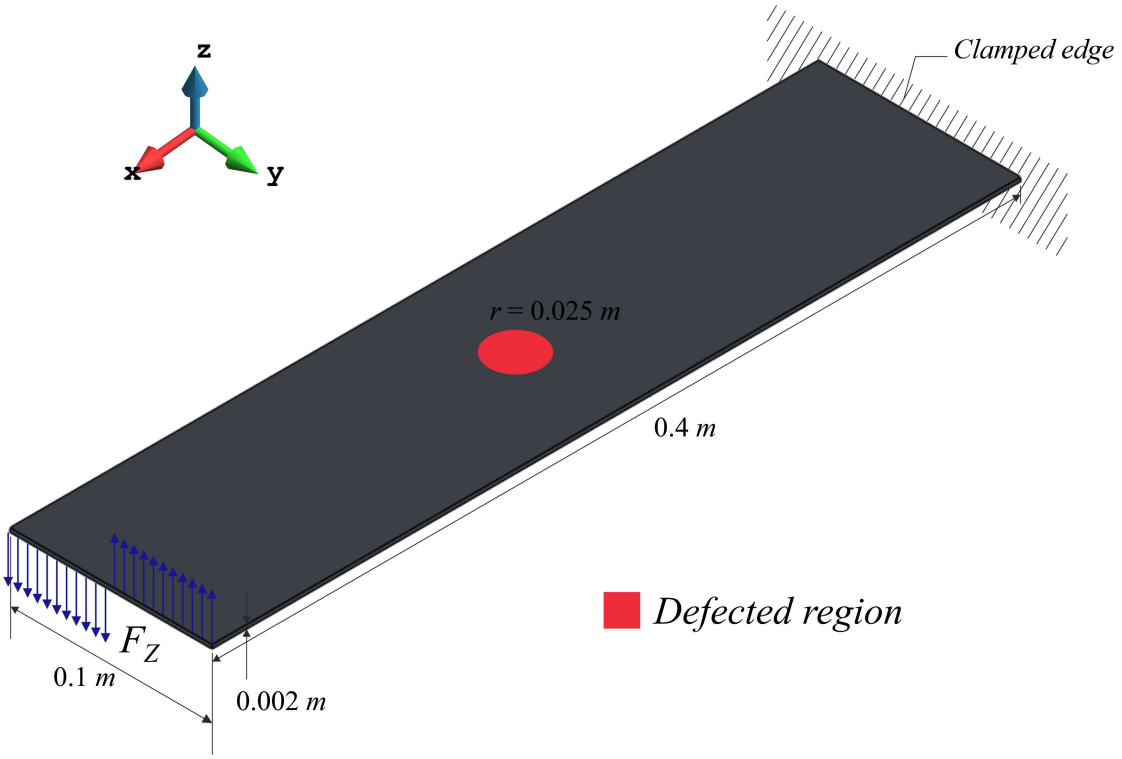

Figure 4.25 Geometry, loading conditions, and boundary conditions of the composite plate with torsional loading.

In this example problem, the strain data are acquired from the top and bottom bounding surfaces of the laminated plate. Moreover, from within the structure strain data are collected from the interface of the fourth and fifth layers of the plate, i.e., the farthest through-the-thickness location from the defected region where strain data can be collected through embedding sensors (e.g., FBG sensors) as illustrated in Figure 2.8. The discretization of the model in the forward analysis consists of a 288×72 grid (20736 elements in total). Then, the strain data which are utilized in the iFEM algorithm are selected in a similar method as depicted in Figure 4.3,

however, in this case study, an individual element block in the forward analysis is a 9×9 grid, indicating that the inverse model consists of 256 elements (Figure 4.26).

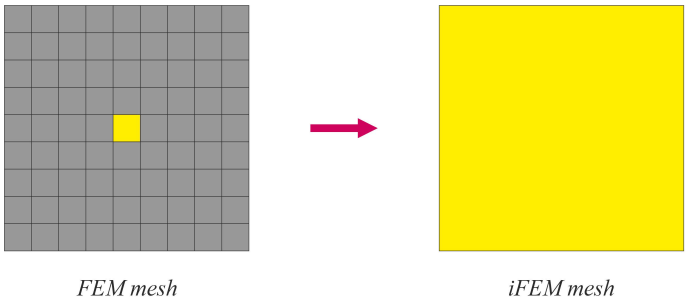

Figure 4.26 Strain data processing from FEM to iFEM.

Strain data used in the inverse algorithm are gathered according to a sparse sensor deployment scheme, illustrated in Figure 4.27(b).

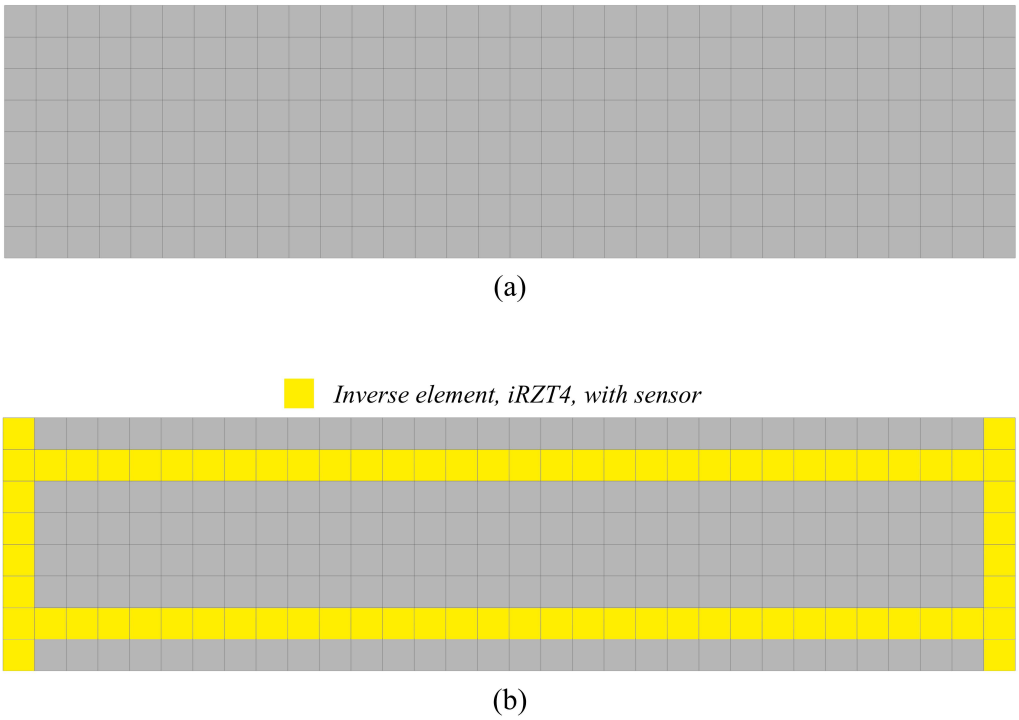

Figure 4.27 Laminated composite plate: (a) iFEM mesh; (b) Sparse sensor placement scheme.

The first set of results in this case study, include the reconstruction of the displacement field through employing the strain data obtained from FEM in iFEM algorithm according to Figures 4.26 and 4.27. The total displacement contours calculated using Eq. (4.2a) are plotted in Figure 4.28. As evident, the iFEM results are presented with reference FEM solution. The percent error calculated using the maximum displacement values is 0.218%, attesting to the robustness of the iFEM in

processing strain data obtained as a result of relatively complex loading condition, e.g., torsional loading, as well its performance even when operating with a set of sparsely provided data.

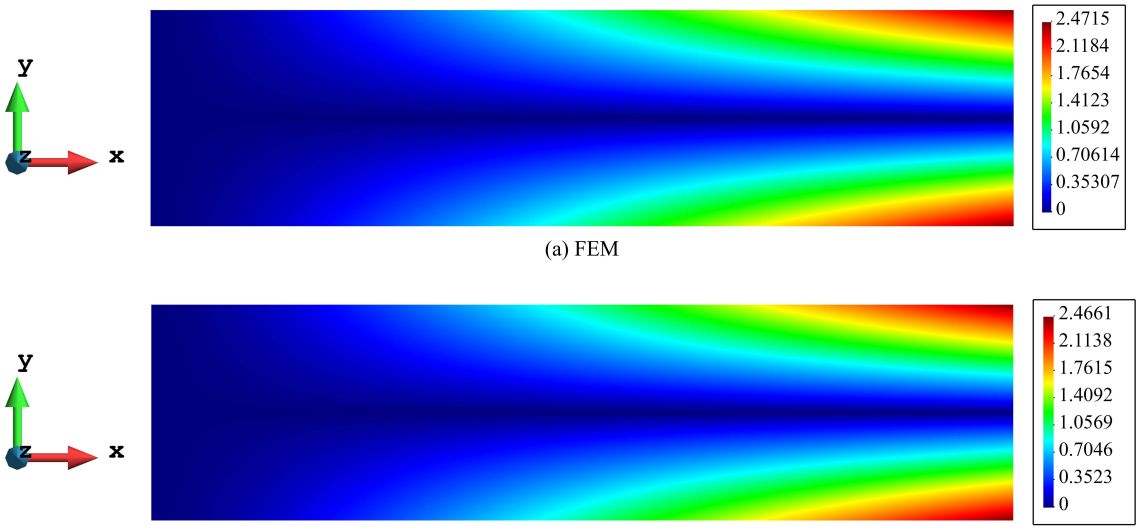

Figure 4.28 Total displacement U_T contours for torsional loading of the laminated composite plate: (a) FEM solution; (b) iFEM solution.

The weighting coefficients for the iRZT4 element (Eq. 2.29) play a key role in obtaining accurate results. These coefficients must be chosen with utmost care in accordance to the problem type and even the geometry of the problem domain. The inverse elements with available sensor data, the weighting coefficients are set as $w_\chi = 1$ ($\chi = \mathbf{e}, \boldsymbol{\kappa}, \boldsymbol{\mu}, \boldsymbol{\gamma}, \boldsymbol{\eta}$). Conversely, for the elements which do not possess any strain inputs, the coefficients are chosen as $w_\chi = \alpha = 10^{-6}$.

The damage sensing capabilities of iFEM-RZT are assessed using two outputs from the study. The membrane damage index which is obtained from Eq. (3.6) when $\chi = \varepsilon$ outlines a region where the existence of damage is the most probable (Figure 4.29) and thereby, highlighting the in-plane position and shape of the defected region.

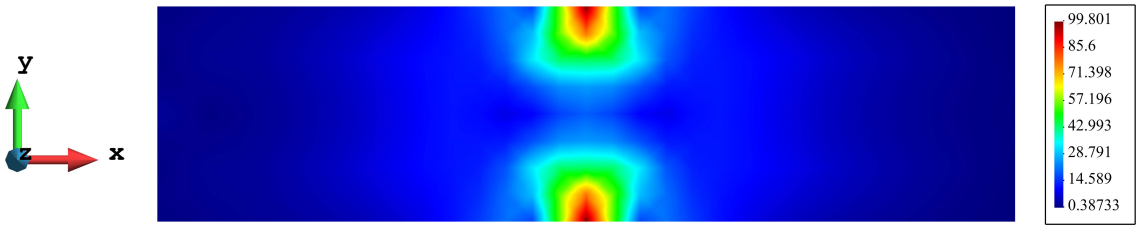

Figure 4.29 Membrane damage index contour for torsional loading of the laminated composite plate; Specifying the region with high probability of damage.

Additionally the twisting damage (Eq. (3.6) with $\chi = \kappa$) predicts the in-plane location of the defected region, and as it is shown, it also provides an estimation of the circular morphology of the defected region at the center of the plate, too (Figure 4.30).

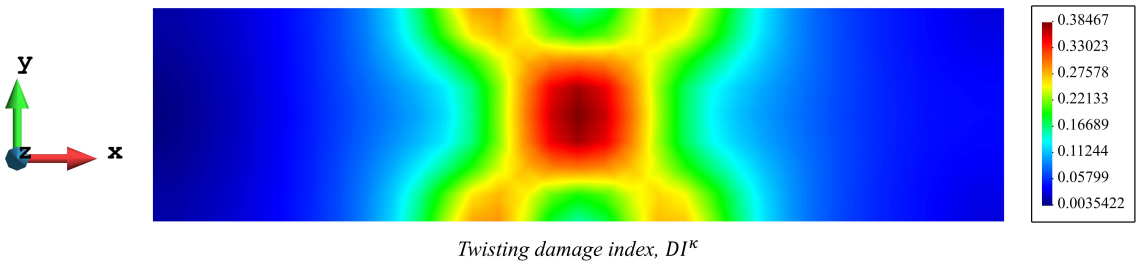

Figure 4.30 Twisting damage index contour for torsional loading of the laminated composite plate; Specifying the location and morphology of the defected region.

Nevertheless, the main advantage of the iFEM-RZT coupling is that it gives further insight regarding through-the-thickness location of the damage. For laminated shells, one of the most common modes of failure is delamination damage. The strain data obtained through-the-thickness of the laminated plate numerically or via embedded sensors can be utilized for detecting damage of this sort. Figure 4.31 shows that the iFEM has predicted the location of the damage in the laminated structure successfully, even when the sensors within the structure are embedded at the farthest location from the damage.

A close examination of the results presented in the Figures 4.29-4.30, exhibited the localization of the damage index at the center of the plate, i.e., the in-plane configuration of the flawed region was identified. By the same token, layer-by-layer scrutiny of the damage index values at the area of interest (the region with localized damage index values), shows the respective damage indices calculated based on the principal strains for each layer, using Eq. (3.7), at the said location is the maximum for the layer corresponding to the counter $k = 2$, namely the second layer (Figure 4.31).

The results obtained thus far show that by using a sparse sensor distribution model the in-plane location and shape of the defected region are captured successfully. Additionally, through-the-thickness damage detection results are obtained in the circumstance that the strain data within the structure was acquired from the interface of the fourth and fifth layers in laminated plate according to the same sparse sensor placement model illustrated in Figure 4.27(b), vividly revealing the superior performance of the iFEM-RZT for study and detection of damage mechanisms such as delamination damage, which occur through-the-thickness of the structure.

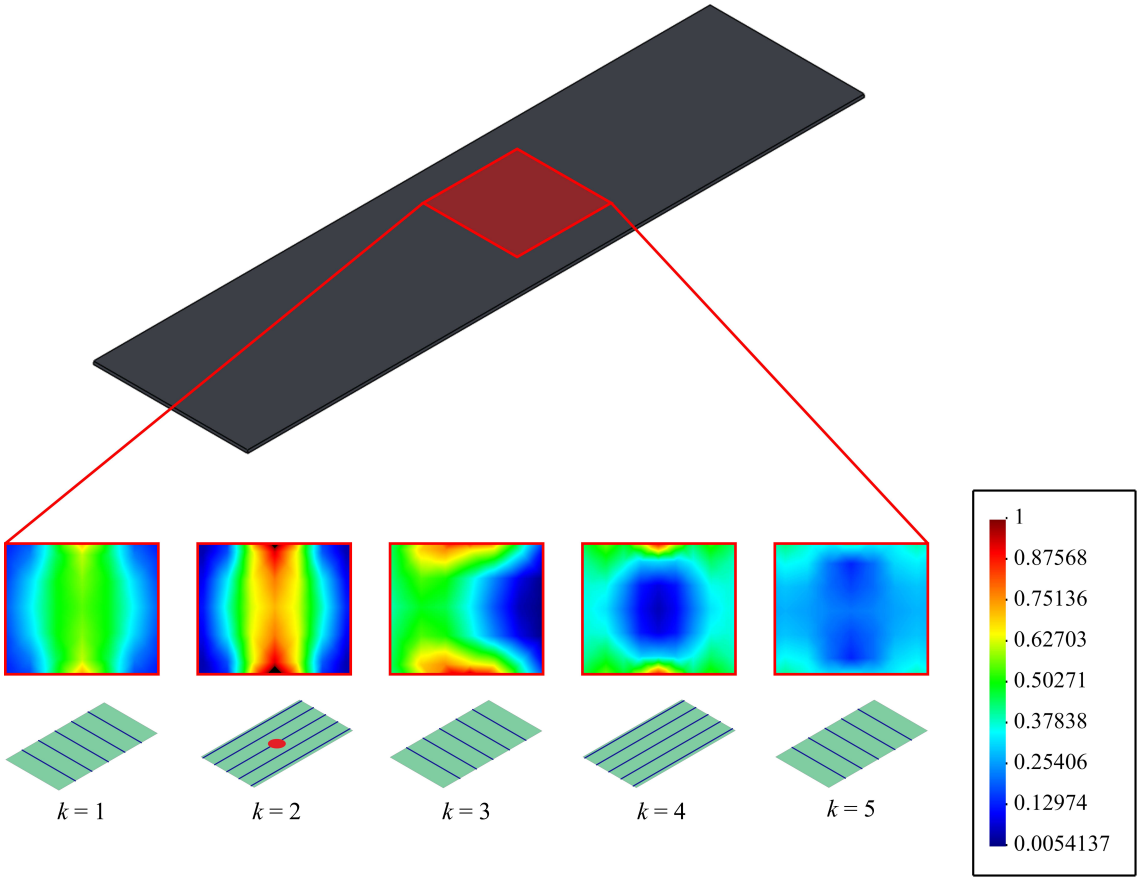

Figure 4.31 Damage index contours for each layer at the region of interest for detecting through-the-thickness location of the damage.

4.5 Axial Loading of a Curved Composite Panel

In the previous subsection the damage detection capabilities of iFEM-RZT for determining the in-plane and through-the-thickness location and morphology of the flawed domain were evaluated successfully by employing this coupled algorithm to a simple flat geometry with a complex loading condition. Albeit the results of this case study were promising and shed light on the study of damage in laminated composite shells, it is by no means sufficient to reach general conclusions based on these results, solely. In this context, an additional case study involving the axial loading of a curved panel is presented herein.

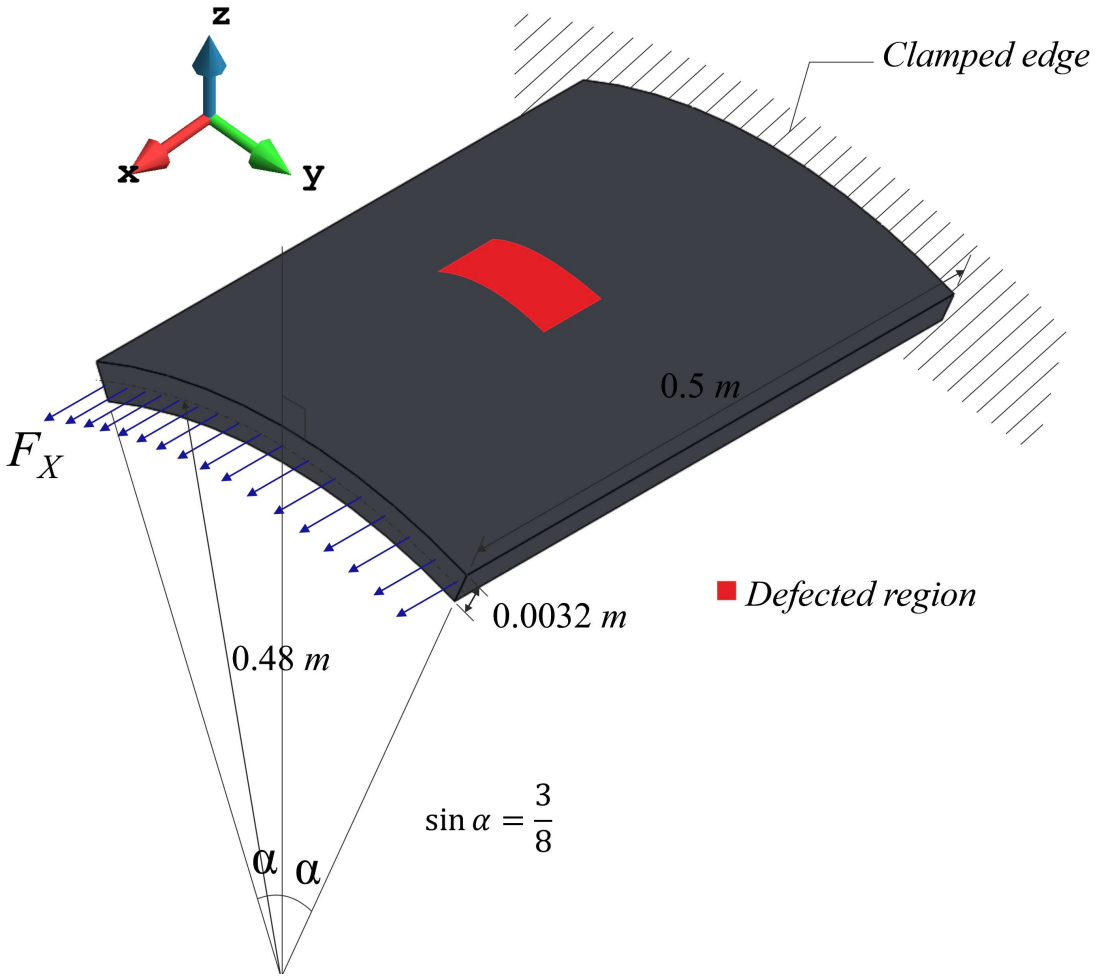

Figure 4.32 Geometry, loading conditions, and boundary conditions of the curved composite panel.

The curved composite panel in this example problem is a quasi-isotropic laminate with a stacking sequence of $[0, \pm 45, 90]_s$. One edge of the panel, as can be seen in Figure 4.32, is clamped, while an axial load is applied to the other end with its magnitude 3200 N/mm. The Geometry of the structure is evident in Figure 4.32. The panel has a thickness of 3.2 mm (0.4 mm/lamina) and as can be seen, this curved panel is also a thin structure similar to the case studies presented before (span-to-thickness ratio $\frac{0.5}{0.0032} \approx 156$). The material model for curved structure is developed based on the material properties provided in Table 4.2 for a single lamina. Furthermore, a curved rectangular defected region ($\lambda = 10^{-5}$) between the seventh and eighth layers of the panel (Figure 4.32).

The strain data for the inverse analysis of this curved composite panel are collected in a procedure similar to what is shown in Figure 4.26. The inverse model of the panel consists of 15×20 elements. As depicted in Figure 4.33, sensors are distributed over the bounding surfaces of the laminated panel and embedded in the interface region

between the first and second laminae in order to prevent the data from having a dominant effect on the solution of the inverse analysis and producing biased results.

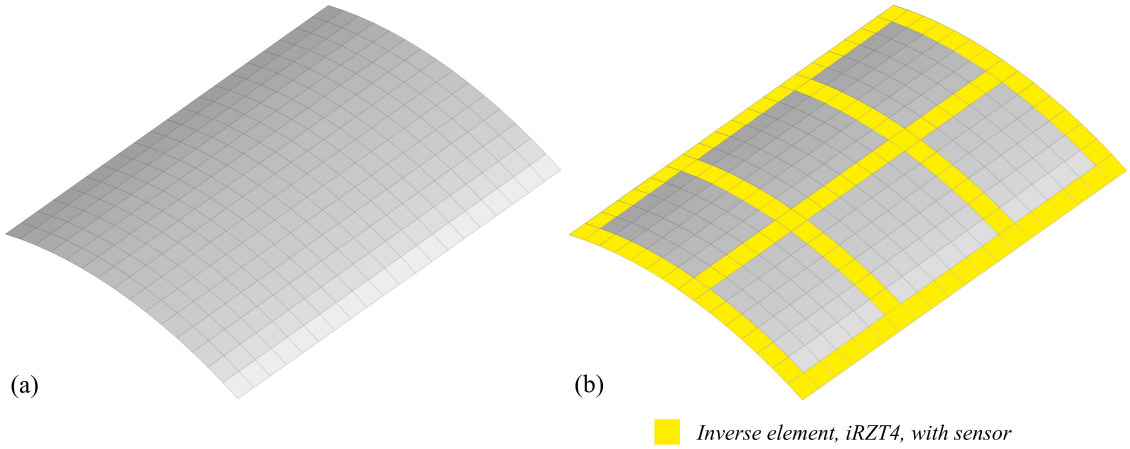

Figure 4.33 Curved composite panel: (a) iFEM Mesh; (b) Sparse sensor placement scheme.

Total displacement contours of the curved shell are derived using the FEM, and then, the displacement field of this structure is reconstructed using the iFEM-RZT algorithm. The respective weighting coefficients (Eq. 2.29) of the elements for which the sensor data are available are assigned as $w_\chi = 1$, whereas for the elements with no strain sensor data, $w_\chi = 10^{-6}$ $(\chi = \mathbf{e}, \boldsymbol{\kappa}, \boldsymbol{\mu}, \boldsymbol{\gamma}, \boldsymbol{\eta})$.

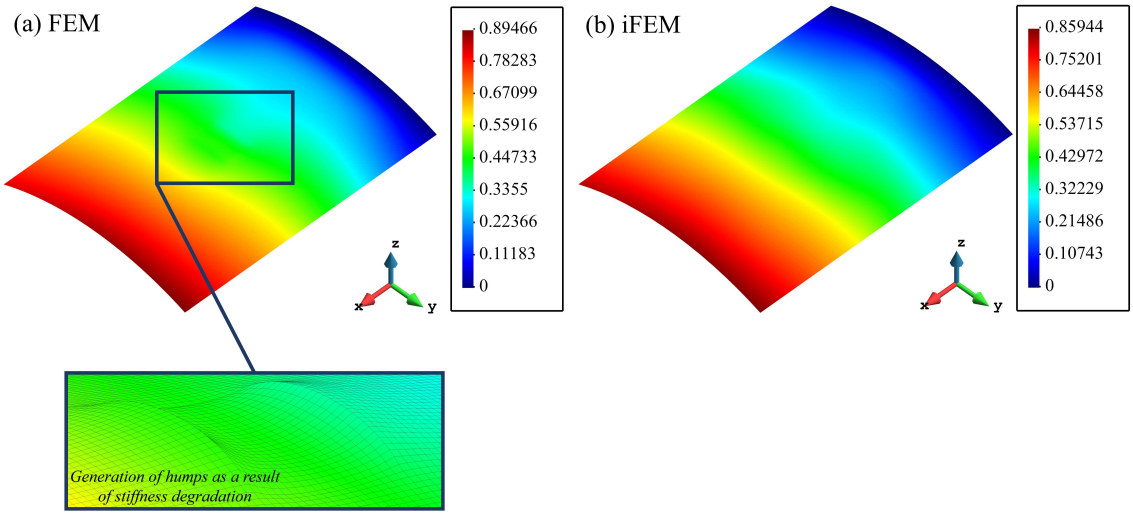

Figure 4.34 Total displacement U_T for axial loading of the curved composite panel: (a) FEM solution; (b) iFEM solution.

The error between the total displacement calculated via FEM and iFEM is calculated as 3.94%. As it is evident from Figure 4.34, the results of the forward analysis show a region where the structure is disturbed as a consequence of the stiffness degradation.

The robustness of the iFEM-RZT algorithm enables reconstruction of the detailed features of the structure as such (Figure 4.35).

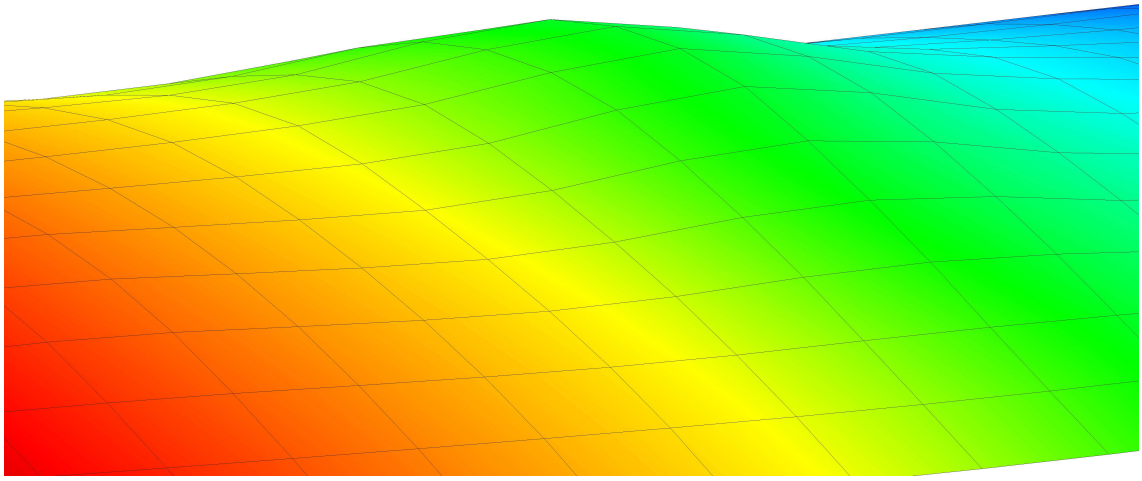

Figure 4.35 Detailed reconstruction of the displacement field utilizing iFEM-RZT algorithm with a sparse distribution of the strain sensors.

Damage monitoring capabilities of the iFEM-RZT have been assessed herein, similar to the previous case studies. In this regard, first, the in-plane detection of damage is undertaken. This goal is accomplished through determining and plotting the membrane (Figure 4.36) and twisting (Figure 4.37) damage indices over the entire domain of the problem. Herein, it is seen that the contours for these damage indices show a rectangular region with a high gradient of the damage index at the center of the structure, which clearly indicates the approximate location and shape of the defected region.

On the other hand, the location of the damage, in this case delamination damage, along the thickness of the laminated curved panel is determined by evaluating the damage indices obtained for each ply, and comparing the maximum value of the index calculated for each lamina.

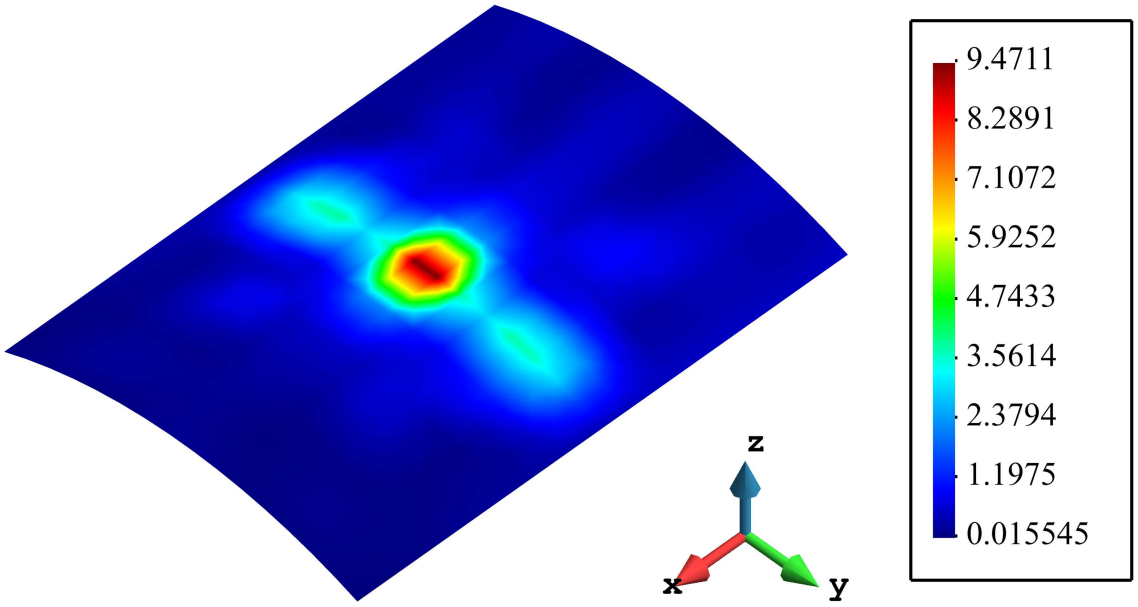

Membrane damage index, DI^{ε}

Figure 4.36 Membrane damage contour for torsional loading of the curved composite panel.

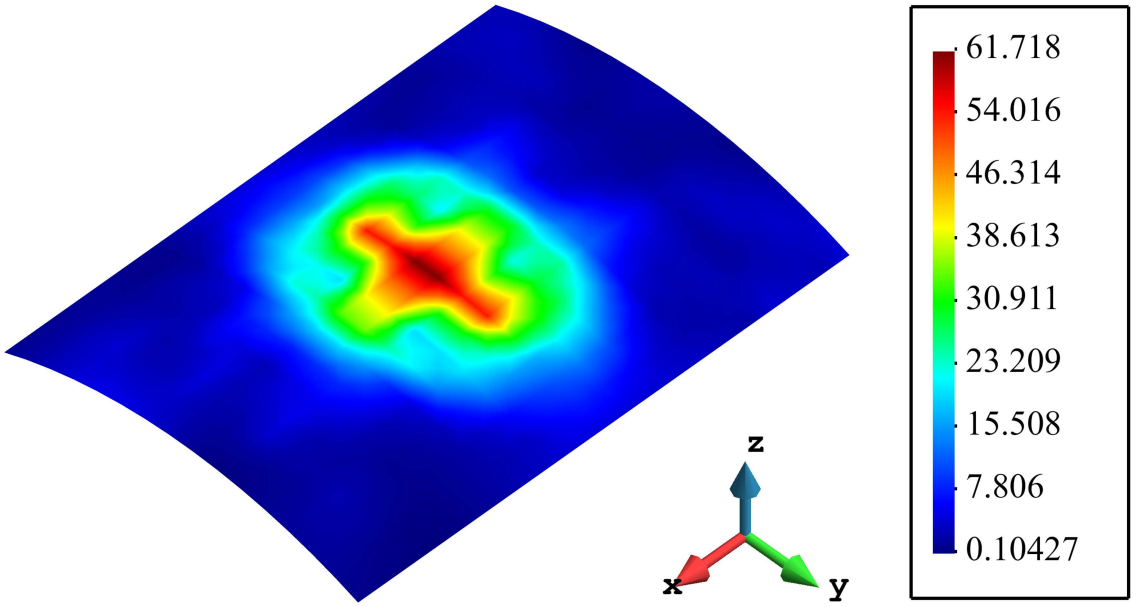

Twisting damage index, DI^{κ}

Figure 4.37 Twisting damage contour for torsional loading of the curved composite panel.

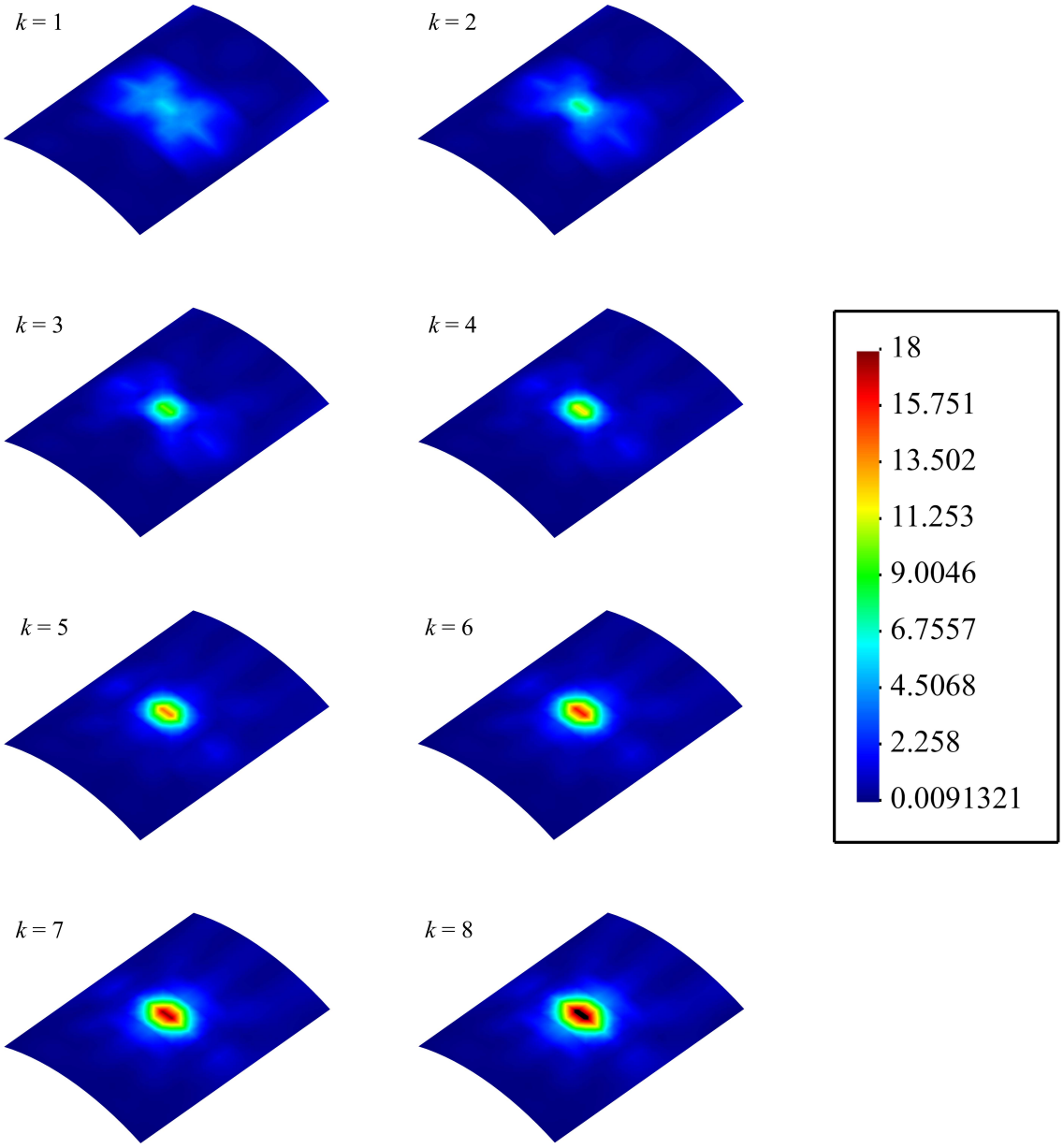

Figure 4.38 Damage indices calculated for each layer of the curved composite panel, for detection of the through-the-thickness location of the defected region.

Through studying the contour plots for the layer-wise damage indices, it is determined that the location of damage, is either at the seventh, or the eighth layer or in the interfacial region between the two plies. This conclusion is supported by the maximum damage index values calculated for these laminae. Hence, iFEM-RZT algorithm proves to be a viable and powerful tool for detection and monitoring of damage both in terms of identifying the in-plane location and shape of the defect and at the same time its through-the-thickness position.

5. CONCLUDING REMARKS

In the present work, several case studies including tensile loading of a plate, transverse bending of laminate composite, and a T-beam, laminated plate with torsional load, and a curved composite panel with axial loading were analyzed to assess the shape-sensing and damage detection capabilities of iFEM. All of these structures were thin plane and plate/shell structures and in all of the case studies, the problem domain possessed a single region or multiple areas with degraded stiffness at various locations over the domain, with similar or different morphology. The inverse analysis was conducted using inverse element types with plane assumption, shell assumption, iQS4, and a combination of the inverse-shell element with RZT assumptions, iRZT4. The input data for the iFEM were generated numerically through performing forward FEM analysis, afterwards, displacement field, equivalent strain, and damage index were exhibited using contour plots. It was seen that the solutions achieved by iFEM are in keeping with the FEM solutions. Nevertheless, in terms of the proximity of results of the inverse method to reference FEM solutions, the inverse-shell element had a better performance in comparison to the inverse-plane element, as the calculated percent errors were considerably lower, and in cases approaching zero. For the first example problem, albeit the results were in an acceptable range, the application of the inverse element is not practical, due to the fact that the solution does not provide results other than two-dimensional displacements, while in complex structures that are commonly used in maritime or aviation industries, a three-dimensional reconstruction of the displacements is required, in conjunction with the recovery of the rotations. In addition, the successful application of the inverse-shell element, iQS4, to a defected composite shell illustrated the robustness of iFEM. The shape-sensing of the laminated shell subjected to transverse bending was precisely conducted, and the locations and shapes of the defected areas were detected.

The validity of the results for the first two case studies paved the way for the application of the iQS4 inverse element to the detection of damage in a more complex structure. To this end, a flawed T-beam was modeled with a distributed bending

load applied along Z direction. The solution to the inverse analysis demonstrated the superior performance of iFEM concerning the shape-sensing of the T-beam structure. In particular, the iQS4 element proved to be very effective in its capability to reconstruct the displacement field with an acceptable correlation between the reference and calculated results, independent of the nature of loading, while specifying the damage and its extent in the problem domain. Yet, owing to the structural design of T-beams, and to the fact that various components of such structures undergo various types of loading, damage index, being a function of the equivalent von Mises strain, appeared to be a reliable source of studying damage when used along with the equivalent strain measures, highlighting the essence of using the von Mises strain contours. The outcome of this case study becomes even more critical as the real-world applications of this method to more complex structures, which can be readily found in maritime and aerospace industries, are considered. T-beams can be deemed as a simplified version of such structures, and with the accurate results obtained herein, it can confidently be concluded that iFEM as a SHM approach, possesses a high potential and efficiency as a damage-sensing approach.

In conjunction with these results, the essence of the through-the-thickness study of damage was also acknowledged, and a novel strategy was developed to address this problem. In this context, the RZT was employed within the iFEM. In this method, the equivalent strain measure, von Mises strain is calculated using the principal section strains, resulting in an approximation of the shape and location of the damage. In addition, a layer-wise calculation of the von Mises strain based on the principal strain values for each lamina is also performed, using which, the damage index for every ply is calculated. Then through comparison of the damage index values for all of the layers of the laminated material, the defected layer in the material is identified. By applying this strategy to a composite plate under torsional loading and a curved composite panel, the position, shape, and size of the damage, both through-the-thickness and in-plane, were configured accurately. The significance of these results is further underscored considering that the strain data acquired from within the laminated structure were from the layer farthest from the delamination damage location, and the sparse placement of the strain sensors, along with preventing the reconstruction of a set of biased solutions, imposes further numerical challenges for the operation of the iFEM-RZT algorithm.

Overall, it was shown that iFEM as a SHM technique, is able to administer solutions to shape-sensing and damage detection of thin laminated structures and composite materials, utilizing the inverse-plane element, the inverse-shell element, or the inverse-shell element coupled with the RZT. Nonetheless, due to the rapid growth of composite technologies and their various industrial applications, the use of this

method can be beneficial in the respective fields. Specifically, for composite materials, the results of this work can be further extended to conduct a study on various damage mechanisms in composite structures. In this context, future studies are expected to detect non-deterministic flaws in composite materials by using experimental test data, and further extending the present damage detection toolbox for identifying the modes of the failure as well.

BIBLIOGRAPHY

Abdollahzadeh, M., Tabrizi, I., Kefal, A., & Yildiz, M. (2021). A combined experimental/numerical study on deformation sensing of sandwich structures through inverse analysis of pre-extrapolated strain measurements. *Measurement*, *185*, 110031.

Abdollahzadeh, M. A., Kefal, A., & Yildiz, M. (2020). A comparative and review study on shape and stress sensing of flat/curved shell geometries using c0-continuous family of ifem elements. *Sensors*, *20*(14), 3808.

Bogert, P., Haugse, E., & Gehrki, R. (2003). Structural shape identification from experimental strains using a modal transformation technique. In *44th AIAA/ASME/ASCE/AHS/ASC Structures, Structural Dynamics, and Materials Conference*, (pp. 1626).

Bruno, R., Toomarian, N., & Salama, M. (1994). Shape estimation from incomplete measurements: A neural-net approach. *Smart Materials and Structures*, *3*(2), 92.

Cerracchio, P., Gherlone, M., Di Sciuva, M., & Tessler, A. (2015). A novel approach for displacement and stress monitoring of sandwich structures based on the inverse finite element method. *Composite Structures*, *127*, 69–76.

Cerracchio, P., Gherlone, M., & Tessler, A. (2015). Real-time displacement monitoring of a composite stiffened panel subjected to mechanical and thermal loads. *Meccanica*, *50*(10), 2487–2496.

Colombo, L., Oboe, D., Sbarufatti, C., Cadini, F., Russo, S., & Giglio, M. (2021). Shape sensing and damage identification with ifem on a composite structure subjected to impact damage and non-trivial boundary conditions. *Mechanical Systems and Signal Processing*, *148*, 107163.

Colombo, L., Sbarufatti, C., & Giglio, M. (2019). Definition of a load adaptive baseline by inverse finite element method for structural damage identification. *Mechanical Systems and Signal Processing*, *120*, 584–607.

De Mooij, C., Martinez, M., & Benedictus, R. (2019). ifem benchmark problems for solid elements. *Smart Materials and Structures*, *28*(6), 065003.

Esposito, M. & Gherlone, M. (2020). Composite wing box deformed-shape reconstruction based on measured strains: Optimization and comparison of existing approaches. *Aerospace Science and Technology*, *99*, 105758.

Gherlone, M., Cerracchio, P., & Mattone, M. (2018). Shape sensing methods: Review and experimental comparison on a wing-shaped plate. *Progress in Aerospace Sciences*, *99*, 14–26.

Gherlone, M., Cerracchio, P., Mattone, M., Di Sciuva, M., & Tessler, A. (2014). An inverse finite element method for beam shape sensing: theoretical framework and experimental validation. *Smart Materials and Structures*, *23*(4), 045027.

Kang, L.-H., Kim, D.-K., & Han, J.-H. (2007). Estimation of dynamic structural displacements using fiber bragg grating strain sensors. *Journal of sound and vibration*, *305*(3), 534–542.

Kefal, A. (2019). An efficient curved inverse-shell element for shape sensing and structural health monitoring of cylindrical marine structures. *Ocean Engineering*, *188*, 106262.

Kefal, A., Mayang, J. B., Oterkus, E., & Yildiz, M. (2018). Three dimensional shape and stress monitoring of bulk carriers based on ifem methodology. *Ocean Engineering*, *147*, 256–267.

Kefal, A. & Oterkus, E. (2015). Structural health monitoring of marine structures by using inverse finite element method. (pp. 341–349). CRC Press.

Kefal, A. & Oterkus, E. (2016a). Displacement and stress monitoring of a chemical tanker based on inverse finite element method. *Ocean Engineering*, *112*, 33–46.

Kefal, A. & Oterkus, E. (2016b). Displacement and stress monitoring of a panamax containership using inverse finite element method. *Ocean Engineering*, *119*, 16–29.

Kefal, A. & Oterkus, E. (2020). Isogeometric ifem analysis of thin shell structures. *Sensors*, *20*(9), 2685.

Kefal, A., Oterkus, E., Tessler, A., & Spangler, J. L. (2016). A quadrilateral inverse-shell element with drilling degrees of freedom for shape sensing and structural health monitoring. *Engineering science and technology, an international journal*, *19*(3), 1299–1313.

Kefal, A., Tabrizi, I., Tansan, M., Kisa, E., & Yildiz, M. (2021). An experimental implementation of inverse finite element method for real-time shape and strain sensing of composite and sandwich structures. *Composite Structures*, *258*, 113431.

Kefal, A., Tabrizi, I., & Yildiz, M. (2021). Real-time monitoring of crack propagation in fiber-reinforced composite plates using ifem methodology. In *Developments in the Analysis and Design of Marine Structures* (pp. 345–353). CRC Press.

Kefal, A., Tabrizi, I. E., Yildiz, M., & Tessler, A. (2021). A smoothed ifem approach for efficient shape-sensing applications: Numerical and experimental validation on composite structures. *Mechanical Systems and Signal Processing*, *152*, 107486.

Kefal, A. & Tessler, A. (2021). Delamination damage identification in composite shell structures based on inverse finite element method and refined zigzag theory. In *Developments in the Analysis and Design of Marine Structures* (pp. 354–363). CRC Press.

Kefal, A., Tessler, A., & Oterkus, E. (2017). An enhanced inverse finite element method for displacement and stress monitoring of multilayered composite and sandwich structures. *Composite Structures*, *179*, 514–540.

Kefal, A. & Yildiz, M. (2017). Modeling of sensor placement strategy for shape sensing and structural health monitoring of a wing-shaped sandwich panel using inverse finite element method. *Sensors*, *17*(12), 2775.

Kim, H.-I., Kang, L.-H., & Han, J.-H. (2011). Shape estimation with distributed fiber bragg grating sensors for rotating structures. *Smart Materials and Structures*, *20*(3), 035011.

Ko, W. L., Richards, W. L., & Fleischer, V. T. (2009). Applications of ko displacement theory to the deformed shape predictions of the doubly-tapered ikhana wing. Technical report.

Ko, W. L., Richards, W. L., & Tran, V. T. (2007). Displacement theories for in-flight deformed shape predictions of aerospace structures. Technical report.

Li, M., Kefal, A., Cerik, B. C., & Oterkus, E. (2020). Dent damage identification in stiffened cylindrical structures using inverse finite element method. *Ocean Engineering*, *198*, 106944.

Li, M., Kefal, A., Oterkus, E., & Oterkus, S. (2020). Structural health monitoring of an offshore wind turbine tower using ifem methodology. *Ocean Engineering*, *204*, 107291.

Liu, M., Zhang, X., Song, H., Zhou, S., Zhou, Z., & Zhou, W. (2018). Inverse finite element method for reconstruction of deformation in the gantry structure of heavy-duty machine tool using fbg sensors. *Sensors*, *18*(7), 2173.

Miller, E. J., Manalo, R., & Tessler, A. (2016). Full-field reconstruction of structural deformations and loads from measured strain data on a wing using the inverse finite element method. Technical report.

Oboe, D., Colombo, L., Sbarufatti, C., & Giglio, M. (2021a). Comparison of strain pre-extrapolation techniques for shape and strain sensing by ifem of a composite plate subjected to compression buckling. *Composite Structures*, *262*, 113587.

Oboe, D., Colombo, L., Sbarufatti, C., & Giglio, M. (2021b). Shape sensing of a complex aeronautical structure with inverse finite element method. *Sensors*, *21*(4), 1388.

Papa, U., Russo, S., Lamboglia, A., Del Core, G., & Iannuzzo, G. (2017). Health structure monitoring for the design of an innovative uas fixed wing through inverse finite element method (ifem). *Aerospace Science and Technology*, *69*, 439–448.

Pisoni, A. C., Santolini, C., Hauf, D. E., & Dubowsky, S. (1995). Displacements in a vibrating body by strain gage measurements. In *Proceedings-SPIE the International Society for Optical Engineering*, (pp. 119–119). SPIE INTERNATIONAL SOCIETY FOR OPTICAL.

Rapp, S., Kang, L.-H., Han, J.-H., Mueller, U. C., & Baier, H. (2009). Displacement field estimation for a two-dimensional structure using fiber bragg grating sensors. *Smart Materials and Structures*, *18*(2), 025006.

Roy, R., Gherlone, M., Surace, C., & Tessler, A. (2021). Full-field strain reconstruction using uniaxial strain measurements: Application to damage detection. *Applied Sciences*, *11*(4), 1681.

Roy, R., Tessler, A., Surace, C., & Gherlone, M. (2020). Shape sensing of plate structures using the inverse finite element method: Investigation of efficient strain–sensor patterns. *Sensors*, *20*(24), 7049.

Tabrizi, I. E., Khan, R. M. A., Massarwa, E., Zanjani, J. S. M., Ali, H. Q., Demir, E., & Yildiz, M. (2019). Determining tab material for tensile test of cfrp laminates with combined usage of digital image correlation and acoustic emission techniques. *Composites Part A: Applied Science and Manufacturing*, *127*, 105623.

Taheri-Behrooz, F. & Bakhshan, H. (2018). Characteristic length determination of notched woven composites. *Advanced Composite Materials*, *27*(1), 67–83.

Tessler, A., Di Sciuva, M., & Gherlone, M. (2010). A consistent refinement of first-order shear deformation theory for laminated composite and sandwich plates using improved zigzag kinematics. *Journal of Mechanics of Materials and Structures*, *5*(2), 341–367.

Tessler, A. & Hughes, T. J. (1983). An improved treatment of transverse shear in the mindlin-type four-node quadrilateral element. *Computer methods in applied mechanics and engineering*, *39*(3), 311–335.

Tessler, A. & Spangler, J. L. (2004). Inverse fem for full-field reconstruction of

elastic deformations in shear deformable plates and shells. In *2nd European Workshop on Structural Health Monitoring*.

Tessler, A. & Spangler, J. L. (2005). A least-squares variational method for full-field reconstruction of elastic deformations in shear-deformable plates and shells. *Computer methods in applied mechanics and engineering*, *194*(2-5), 327–339.

APPENDIX A

A complementary set of equations is presented herein in connection with the shape functions and the strain-displacement matrices for both the inverse-plane and inverse-shell elements. The shape functions N_i are defined in the following order:

$$N_1 = \frac{1}{4}(1-s)(1-t) \tag{A.1}$$

$$N_2 = \frac{1}{4}(1+s)(1-t) \tag{A.2}$$

$$N_3 = \frac{1}{4}(1+s)(1+t) \tag{A.3}$$

$$N_4 = \frac{1}{4}(1-s)(1+t) \tag{A.4}$$

$$N_5 = \frac{1}{16}(1-s^2)(1-t) \tag{A.5}$$

$$N_6 = \frac{1}{16}(1+s)(1-t^2) \tag{A.6}$$

$$N_7 = \frac{1}{16}(1-s^2)(1+t) \tag{A.7}$$

$$N_8 = \frac{1}{16}(1+s)(1-t^2) \tag{A.8}$$

As illustrated, these functions are defined in the isoparametric space, with $-1 \leq s,t \leq +1$. The Eqs. (A.1-A.4) are used for the inverse-plane element, while for the inverse-shell element, all of the shape functions in Eqs. (A.1-A.8) are utilized. The strain-displacement matrix for the inverse-plane element, mentioned in Eq. (2.4), is obtained by calculating the derivative of the shape functions with respect to the local reference frame. To this end,

$$\mathbf{B}^m_{p,i} = \begin{bmatrix} N_{i,x} & 0 \\ 0 & N_{i,y} \\ N_{i,y} & N_{i,x} \end{bmatrix} \quad (i = 1,2,3,4) \tag{A.9}$$

hence,

$$\mathbf{B}^m_p = \begin{bmatrix} \mathbf{B}^m_{p,1} & \mathbf{B}^m_{p,2} & \mathbf{B}^m_{p,3} & \mathbf{B}^m_{p,4} \end{bmatrix} \tag{A.10}$$

For the inverse-shell element, the shape functions L_i, and M_i are similarly, defined in the isoparametric reference frame. Using the Eqs. (A.1-A.8), the L_i and M_i are defined as links between the translation degrees of freedom and hierarchical artificial rotation degree of freedom:

$$L_1 = y_{14}N_8 - y_{21}N_5 \tag{A.11}$$

$$L_2 = y_{21}N_5 - y_{32}N_6 \tag{A.12}$$

$$L_3 = y_{32}N_6 - y_{43}N_7 \tag{A.13}$$

$$L_4 = y_{43}N_7 - y_{14}N_8 \tag{A.14}$$

$$M_1 = x_{41}N_8 - x_{12}N_5 \tag{A.15}$$

$$M_2 = x_{12}N_5 - x_{23}N_6 \tag{A.16}$$

$$M_3 = x_{23}N_6 - x_{34}N_7 \tag{A.17}$$

$$M_4 = x_{34}N_7 - x_{41}N_8 \tag{A.18}$$

where,

$$\left.\begin{aligned} x_{ij} &= x_i - x_j \\ y_{ij} &= y_i - y_j \end{aligned}\right\} \quad (i = 1,2,3,4)(j = 1,2,3,4) \tag{A.19}$$

are the edge lengths of the inverse-shell element. The strain-displacement matrices for membrane, $\mathbf{B}_s^m$, for bending, $\mathbf{B}^b$, and for transverse shear, $\mathbf{B}^s$, are derived as the following:

$$\mathbf{B}_{s,i}^m = \begin{bmatrix} N_{i,x} & 0 & 0 & 0 & 0 & L_{i,x} \\ 0 & N_{i,y} & 0 & 0 & 0 & M_{i,y} \\ N_{i,y} & N_{i,x} & 0 & 0 & 0 & L_{i,y} + M_{i,x} \end{bmatrix} \quad (i = 1,2,3,4) \tag{A.20}$$

$$\mathbf{B}_i^b = \begin{bmatrix} 0 & 0 & 0 & 0 & N_{i,x} & 0 \\ 0 & 0 & 0 & -N_{i,y} & 0 & 0 \\ 0 & 0 & 0 & -N_{i,x} & N_{i,y} & 0 \end{bmatrix} \quad (i = 1,2,3,4) \tag{A.21}$$

$$\mathbf{B}_i^s = \begin{bmatrix} 0 & 0 & N_{i,x} & -L_{i,x} & -M_{i,x}+N_i & 0 \\ 0 & 0 & N_{i,y} & -L_{i,y}-N_i & -M_{i,y} & 0 \end{bmatrix} \quad (i=1,2,3,4) \tag{A.22}$$

subsequently,

$$\mathbf{B}_s^m = \begin{bmatrix} \mathbf{B}_{s,1}^m & \mathbf{B}_{s,2}^m & \mathbf{B}_{s,3}^m & \mathbf{B}_{s,4}^m \end{bmatrix} \tag{A.23}$$

$$\mathbf{B}^b = \begin{bmatrix} \mathbf{B}_1^b & \mathbf{B}_2^b & \mathbf{B}_3^b & \mathbf{B}_4^b \end{bmatrix} \tag{A.24}$$

$$\mathbf{B}^s = \begin{bmatrix} \mathbf{B}_1^s & \mathbf{B}_2^s & \mathbf{B}_3^s & \mathbf{B}_4^s \end{bmatrix} \tag{A.25}$$

However, it was noted that for the iRZT4 element, there were complementary strain-displacement relations. The strain-displacement matrices for this inverse-element type are presented below. It must be noted that matrices corresponding to the membrane, bending, and transverse-shear strain modes are already calculated when deriving the relations for the inverse-shell element. Hence, it can be written that,

$$\mathbf{B}^e = \mathbf{B}_s^m \tag{A.26}$$

$$\mathbf{B}^\kappa = \mathbf{B}^b \tag{A.27}$$

$$\mathbf{B}^\gamma = \mathbf{B}^s \tag{A.28}$$

Furthermore for the strain-displacement matrix emerging as a result of zigzag rotations,

$$\mathbf{B}_i^\mu = \begin{bmatrix} 0 & 0 & 0 & 0 & 0 & 0 & 0 & N_{i,x} & 0 \\ 0 & 0 & 0 & 0 & 0 & 0 & -N_{i,y} & 0 & 0 \\ 0 & 0 & 0 & 0 & 0 & 0 & 0 & N_{i,y} & 0 \\ 0 & 0 & 0 & 0 & 0 & 0 & -N_{i,x} & 0 & 0 \end{bmatrix} \tag{A.29a}$$

hence,

$$\mathbf{B}^\mu = \begin{bmatrix} \mathbf{B}_1^\mu & \mathbf{B}_2^\mu & \mathbf{B}_3^\mu & \mathbf{B}_4^\mu \end{bmatrix} \tag{A.29b}$$

And for the transverse-shear strain term associated with $\chi = \eta$ in Eq. (2.27),

$$\mathbf{B}_i^{\eta} = \begin{bmatrix} 0 & 0 & N_{i,x} & -L_{i,x} & -M_{i,x}+N_i & 0 & L_{i,x} & M_{i,x}-N_i & 0 \\ 0 & 0 & N_{i,y} & -L_{i,y}-N_i & -M_{i,y} & 0 & L_{i,y}+N_i & M_{i,y} & 0 \end{bmatrix} \tag{A.30a}$$

yielding

$$\mathbf{B}^{\eta} = \begin{bmatrix} \mathbf{B}_1^{\eta} & \mathbf{B}_2^{\eta} & \mathbf{B}_3^{\eta} & \mathbf{B}_4^{\eta} \end{bmatrix} \tag{A.30b}$$